

博士後期学位論文

**Corrosion resistance and tribological properties  
on surface of DLC films-coated metal substrate  
prepared by IBED**

IBED 法を用いた DLC/金属の成膜表面における  
耐食耐摩耗特性に関する研究

韓 貝貝

埼玉工業大学大学院



## ABSTRACT

Diamond-like carbon (DLC) films exhibit high hardness, low friction, excellent wear resistance, high anticorrosion resistance, good biocompatibility, high surface tension with water, and optical transparency in various fields such as the automotive, aerospace, communication and biomedical industries. In this study, diamond-like carbon (DLC) films were deposited successfully on magnesium alloy AZ31 substrate as hard protective film by ion-beam-enhanced deposition with various  $\text{CH}_4/\text{H}_2$  ratio, gas flow rates and accelerating voltages. The composition and mechanical properties of the DLC coatings were characterized using scanning electron microscopy (SEM), Raman spectroscopy, Rockwell test, and micro-indentation. The tribological properties of the coating were also investigated using a frictional surface microscope with an in situ observation system and friction force measurements. The DLC films were characterized by a lower intensity ratio of the D-peak to G-peak (ID/IG), higher hardness, and improved tribological properties when deposited at a lower accelerating voltage (6 kV). At the  $\text{CH}_4/\text{H}_2$  ratio of 1:99 and 6 sccm/6 kV, minimum ID/IG values of 0.62, relatively low friction force value of 0.12 N, and a maximum hardness of 4056 HV were attained respectively. In addition, the DLC film exhibited improved wear resistance and a shallower wear track at this condition.

The characterizations and corrosion behaviors of the DLC-coated stainless steel and titanium which used in bipolar plates deposited with different gas ratios  $\text{CH}_4/\text{H}_2$  and deposition times were investigated and evaluated. The chemical bonding structure and composition of the DLC coatings were confirmed by Raman spectroscopy, X-ray photoelectron spectroscopy (XPS) and Transmission Electron Microscope (TEM). The micromorphology and surface roughness of the films were observed and analyzed by

SEM and AFM. The element compositions of cross-section were determined by Electron probe microanalysis (EPMA). The DLC-coated stainless steel and titanium were corroded by potentiostatic polarizations in a 0.5mol/L sulfuric acid solution at 90 °C for 168 h and the corrosion behaviors were investigated in the solution using electrochemical techniques. In addition, the metal ions in sulfuric acid corrosion solution were detected by inductively coupled plasma (ICP) atomic emission spectroscopy. The results indicate that a higher CH<sub>4</sub>/H<sub>2</sub> ratio for titanium and a lower CH<sub>4</sub>/H<sub>2</sub> ratio for stainless steel can result in a decreasing ID/IG ratio, low root mean square (RMS) of the surface morphology and low concentration of metal ions in corrosion solution. The ID/IG ratio of corroded DLC coating on titanium with a minimum of 0.827 is lower than that of corroded DLC coating on stainless steel with a minimum of 1.03. The significant improvement in the corrosion resistance of DLC film was mainly attributed to the increased sp<sup>3</sup> bond element and formation of passive film. The minimum resistivity of 12.9 mΩ·cm<sup>2</sup> for DLC film-coated SUS316L is obtained, which is higher than that of 7 mΩ·cm<sup>2</sup> for DLC film-coated titanium. The metal ions concentration of a DLC coating on titanium with a minimum of 0.34 ppm is obviously lower than that of a DLC coating on stainless steel with a minimum of 16.60 ppm. The corrosion mechanism of stainless steel is proposed. As a result, the localized corrosion of a point or small area has been significantly improved after depositing the DLC films, the DLC films-coated titanium substrate is more promising in the applications with the superior anti-corrosion properties.

Keywords: DLC film; corrosion resistance; tribological properties; IBED; metal substrate

# Contents

<b>Chapter 1 Introduction</b> .....	1
1.1 Research background and significance .....	1
1.2 Performance characteristics and mechanical application of magnesium alloy substrate .....	3
1.2.1 Mechanical application of magnesium alloy .....	3
1.2.2 Tribological properties of magnesium alloy .....	5
1.3 Application of titanium and stainless steel materials for fuel cells and surface modification methods .....	9
1.3.1 Application of titanium and stainless steel for fuel cells .....	9
1.3.2 Surface modification methods for titanium and stainless steel .....	11
1.4 Performance characteristics of Diamond-Like Carbon films .....	14
1.4.1 DLC films .....	14
1.4.2 Problems of DLC films-coated metal substrate .....	18
1.5 Thesis objective and structure .....	19
References .....	22
<b>Chapter 2 Experimental methods and principle</b> .....	29
2.1 Preparation of DLC films .....	29
2.1.1 Experimental materials and substrate processing .....	29
2.1.2 Deposition of DLC films on different substrates .....	30
2.2 Experimental analysis methods .....	33
2.2.1 Raman analysis .....	33
2.2.2 Micromorphology analysis .....	34
2.2.3 XPS analysis .....	37
2.2.4 TEM analysis .....	40
2.3 Analysis of hardness and tribological behavior .....	41
2.4 Corrosion performance analysis .....	43
2.4.1 Corrosion test .....	43
2.4.2 Corrosion behavior DLC films .....	45
References .....	48
<b>Chapter 3 Surface characteristics and tribological properties of DLC films on magnesium alloy</b> .....	51
3.1 Chemical bonding structure of DLC films .....	51
3.2 Hardness analysis of DLC films .....	54

3.3 Cross-section morphology and thickness analysis of DLC films.....	56
3.4 Tribological properties of DLC films .....	59
3.5 Summary.....	65
References .....	67
<b>Chapter 4 Microstructure analysis and corrosion resistance of DLC films-coated titanium .....</b>	<b>69</b>
4.1 Surface and cross-section morphology of DLC films deposited on titanium.....	69
4.1.1 Surface morphology and roughness .....	69
4.1.2 Cross-sectional morphology and thickness .....	72
4.2 Chemical composition and microstructure analysis of DLC films deposited on titanium.....	76
4.2.1 Raman spectroscopy of DLC films on titanium.....	76
4.2.2 TEM analysis of DLC films on titanium.....	78
4.2.3 XPS analysis of DLC films on titanium.....	80
4.3 Interfacial Contact Resistance of DLC films deposited on titanium.....	82
4.4 Corrosion resistance of DLC films-coated titanium.....	83
4.4.1 Surface characteristics of DLC films-coated titanium after corrosion.....	83
4.4.2 Effect of DLC films on metal ions dissolution.....	85
4.4.3 Electrochemical behaviors of DLC films deposited on titanium .....	86
4.5 Summary.....	88
References .....	91
<b>Chapter 5 Chemical composition and corrosion behavior of DLC films-coated stainless steel .....</b>	<b>95</b>
5.1 Surface and cross-section morphology of DLC films deposited on SUS316L....	95
5.1.1 Surface morphology and roughness .....	95
5.1.2 Cross-sectional morphology and thickness .....	99
5.2 Chemical composition and microstructure analysis of DLC films deposited on SUS316L .....	103
5.2.1 Raman spectroscopy of DLC films on SUS316L.....	103
5.2.2 TEM analysis of DLC films on SUS316L .....	106
5.2.3 XPS analysis of DLC films on SUS316L .....	107
5.3 Interfacial Contact Resistance of DLC films deposited on SUS316L .....	109
5.4 Corrosion behavior of DLC films-coated SUS316L.....	110
5.4.1 Surface characteristics of DLC films-coated SUS316L after corrosion.....	110
5.4.2 Effect of DLC films on metal ions dissolution.....	114
5.4.3 Electrochemical behaviors of DLC films deposited on SUS316L.....	115

5.5 Summary.....	117
References .....	119
<b>Chapter 6 Conclusion</b> .....	123
6.1 Discussion and summary .....	123
6.2 Future work .....	125
<b>Related Publications</b> .....	127
<b>Acknowledgements</b> .....	129



# Chapter 1 Introduction

## 1.1 Research background and significance

The movement of mechanical parts is always accompanied by friction and wear [1, 2]. A large number of industrial parts fail because the surface properties are inability to meet the severe friction and wear service conditions such as heavy load and high speed conditions [3]. Magnesium alloys have recently been widely applied as structural materials because of their light weight, high dimensional stability, excellent electromagnetic shielding and damping performance, excellent machinability, and easy of recycling [4, 5]. They are practically used in various fields such as the automotive, aerospace, communication and biomedical industries. However, the poor hardness, abrasion resistance, and corrosion resistance of magnesium alloys limit their application [6]. Modification of the material surface is an effective means to improve these properties to enable the use of magnesium for more machine parts [7].

Currently there are much attention about the development of more efficient and cleaner technologies. Fuel cells are environmentally friendly energy generation devices, which convert chemical energy directly into electrical energy [8]. Polymer electrolyte membrane fuel cell (PEMFC) is an ideal candidate as one of the most potential power sources for residential and transportation applications with high efficiency and virtual zero-emissions among all kinds of the fuel cells [9-11]. The PEM fuel cell is consisted of membrane electrode assemblies (MEAs), gas diffusion layers (GDLs) and bipolar plates. As a major component of the PEMFC stack, the bipolar plates have the most total weight and the most expensive cost. These bipolar plates play multiple roles in the following functions

such as distributing the air to a gas diffusion layer-electrodes assembly uniformly, removing heat and water flow from the active areas, providing the electrical contact and carrying current from adjacent cells [12]. So it is necessary to reduce the cost and the large mass of these components for the commercial application of PEFC fuel cells [13]. For the development of PEMFCs, bipolar plates should have the characteristics such as high anticorrosion resistance, high electrical conductivity, lightweight, high mechanical manufacturability, high surface tension with water and low cost [14].

The traditional bipolar plate material is non-porous graphite due to its high electronic conductivity and good chemical stability in PEMFC environments. However, it is fragile to impact. Meanwhile the manufacture costs of gas flow channels are increased and the overall volume of the PEMFCs becomes bigger [15]. The graphite is not an ideal candidate for commercialization application directly. Hence the metallic bipolar plates such as stainless steel is commercially available [16]. Compared with graphite, the stainless steels have the advantages of high volumetric electrical conductivity, high mechanical strength, low gas permeability, and economic to manufacture particularly suitable for portable PEMFCs. However the stainless steel is highly vulnerable to corrosive attack in the strong acidic fuel cell environment of the electrolyte membrane with the pH value of about 2-3 [17]. The interfacial contact resistance of stainless steel material should also be considered. The other metals such as titanium alloys show the better performances in the corrosion resistance and have a higher mechanical strength than the stainless steel but the higher cost. The corrosion behavior of the metallic bipolar plate can degrade the fuel cell performance because the proton conductivity of the polymeric electrolyte membrane is decreased due to the poison of Fe, Cr and Ni ions [11].

To overcome these drawbacks, depositing a protective coating on the metallic bipolar

plate is necessary by various surface modification techniques. Therefore, in this paper DLC films were deposited on the surface of magnesium alloy substrate by IBED to improve the tribological properties, and on the surface of titanium and stainless steel substrate to protect the bare metallic bipolar plate from the highly acidic environment. The hardness and wear resistance on surface of DLC films-coated AZ31 magnesium alloy were analyzed. The optimal conditions were found to improve wear resistance and a shallower wear track. The characterizations and corrosion behaviors of the DLC films-coated titanium and stainless steel were investigated and evaluated. The chemical bonding structure and composition of the DLC coatings were analyzed to obtain the mechanism of anti-corrosion.

## 1.2 Performance characteristics and mechanical application of magnesium alloy substrate

### 1.2.1 Mechanical application of magnesium alloy

In the past, magnesium was used extensively in World War I and again in World War II but apart from use in niche applications in the nuclear industry, metal and military aircraft, interest subsequently waned. The most significant application was its use in the VW beetle but even this petered out when higher performance was required. The requirement to reduce the weight of car components as a result in part of the introduction of legislation limiting emission has triggered renewed interest in magnesium. In 1944 the consumption had reached 228 000 t but slumped after the war to 10 000 t per annum. In 1998 with renewed interest it has climbed to 360 000 t per annum at a price of US\$3.6 per kg. The growth rate over the next 10 years has been forecast to be 7% per annum [18].

The advantages of magnesium and magnesium alloys are listed as follows,

- lowest density of all metallic constructional materials;
- high specific strength; good castability, suitable for high pressure die-casting;
- can be turned/milled at high speed;
- good weldability under controlled atmosphere;
- much improved corrosion resistance using high purity magnesium;
- readily available;
- compared with polymeric materials:
  - better mechanical properties;
  - resistant to ageing;
  - better electrical and thermal conductivity;
  - recyclable.

One of the reasons for the limited use of magnesium has been some poor properties exacerbated by a lack of development work. The disadvantages of magnesium are presented based on the following:

- low elastic modulus;
- limited cold workability and toughness;
- limited high strength and creep resistance at elevated temperatures;
- high degree of shrinkage on solidification;
- high chemical reactivity;
- in some applications limited corrosion resistance.

It is not possible to use conventional alloying techniques to improve some of the properties, e.g. elastic constants. The use of magnesium alloys in the European automobile industry encompasses parts such as steering wheels, steering column parts,

instrument panels, seats, gear boxes, air intake systems, stretcher, gearbox housings, tank covers etc. Magnesium based alloys have been used for numerous applications in hobby equipment e.g. bicycle frames. In communication engineering, light weight is required as well as screening against electro–magnetic radiation which plastic materials cannot offer.

Magnesium alloy, the lightest metallic construction material with high strength/weight ratio, high thermal conductivity, good machinability and recyclability, is considered as the most promising green engineering material in the 21st century [19, 20]. Therefore, magnesium and its alloys are attracting great interest as they have enormous promising potential applications in the automotive, aircraft, aerospace, electronic industries, biological materials and so on [21]. For some lightweight soft matrix materials such as aluminum alloys, although they have the characteristics of light weight and high specific strength, their surface wear resistance is poor, which seriously affects the safety and reliability of these parts.

### 1.2.2 Tribological properties of magnesium alloy

Tribology is the science and engineering of interacting surfaces in relative motion. It includes the study and application of the principles of friction, lubrication and wear. Tribology is highly interdisciplinary. The wear is the progressive involuntary removal of material from a surface in relative motion with another or with a fluid. We can distinguish two different types of wear: moderate wear and severe wear [22, 23]. The first case concerns low loads and smooth surfaces, while the second concerns significantly higher loads and compatible and rough surfaces, in which the wear processes are much more violent. Wear plays a fundamental role in tribological studies, since it causes changes in the shape of the components used in the construction of machinery (for example). These

worn parts must be replaced and this entails both a problem of an economic nature, due to the cost of replacement, and a functional problem, since if these components are not replaced in time, more serious damage could occur to the machine in its complex. This phenomenon, however, has not only negative sides, indeed, it is often used to reduce the roughness of some materials, eliminating the asperities. Erroneously we tend to imagine wear in a direct correlation with friction, in reality these two phenomena cannot be easily connected. There may be conditions such that low friction can result in significant wear and vice versa. In order for this phenomenon to occur, certain implementation times "are required, which may change depending on some variables, such as load, speed, lubrication and environmental conditions, and there are different wear mechanisms, which may occur simultaneously or even combined with each other:

1. Adhesive Wear;
2. Abrasive Wear;
3. Fatigue Wear;
4. Corrosive Wear;
5. Rubbing Wear or Fretting;
6. Erosion Wear;
7. Other minor wear phenomena (Wear by Impact, Cavitation, Wear-Fusion, Wear-Spreading).

As known, the contact between two surfaces occurs through the interaction between asperities [24]. If a shearing force is applied in the contact area, it may be possible to detach a small part of the weaker material, due to its adhesion to the harder surface. What is described is precisely the mechanism of the adhesive wear represented in the figure. This type of wear is very problematic, since it involves high wear speeds, but at the same

time it is possible to reduce adhesion by increasing surface roughness and hardness of the surfaces involved, or by inserting layers of contaminants such as oxygen, oxides, water or oils. In conclusion, the behavior of the adhesive wear volume can be described by means of three main laws.

The abrasive wear consists of the cutting effort of hard surfaces that act on softer surfaces and can be caused either by the roughness that as tips cut off the material against which they rub (two-body abrasive wear), or from particles of hard material that interpose between two surfaces in relative motion (three-body abrasive wear) [25, 26]. At application levels, the two-body wear is easily eliminated by means of an adequate surface finish, while the three-body wear can bring serious problems and must therefore be removed as much as possible by means of suitable filters, even before of a weighted machine design.

The fatigue wear is a type of wear that is caused by alternative loads, which cause local contact forces repeated over time, which in turn lead to deterioration of the materials involved [27]. The most immediate example of this type of wear is that of a comb. If you slide a finger over the teeth of the comb over and over again, it is observed that at some point one or more teeth of the comb come off. This phenomenon can lead to the breaking of the surfaces due to mechanical or thermal causes. The first case is that described above in which a repeated repeated load causes high contact stresses. The second case, however, is caused by the thermal expansion of the materials involved in the process. To reduce this type of wear, therefore, it is good to try to decrease both the contact forces and the thermal cycling, that is the frequency with which different temperatures intervene. For optimal results it is also good to eliminate, as much as possible, impurities between surfaces, local defects and inclusions of foreign materials in the bodies involved.

The rubbing wear occurs in systems subject to more or less intense vibrations, which cause relative movements between the surfaces in contact with the order of the nanometer [28]. These microscopic relative movements cause both adhesive wear, caused by the displacement itself, and abrasive wear, caused by the particles produced in the adhesive phase, which remain trapped between the surfaces. This type of wear can be accelerated by the presence of corrosive substances and the increase in temperature [29].

The erosion wear occurs when free particles, which can be either solid or liquid, hit a surface, causing abrasion [30]. The mechanisms involved are of various kinds and depend on certain parameters, such as the impact angle, the particle size, the impact velocity and the material of which the particles are made up.

Among the factors we find hardness, mutual solubility and crystalline structure affecting wear [31]. It has been verified that the harder a material is, the more it decreases. In the same way, the less two materials are mutually soluble, the more the wear tends to decrease. Finally, as regards the crystalline structure, it is possible to state that some structures are more suitable to resist the wear of others, such as a hexagonal structure with a compact distribution, which can only deform by slipping along the base planes.

The high friction coefficient of magnesium alloy limits the application of magnesium alloy materials as mechanical parts, and the research on the tribology of related magnesium alloys is also insufficient. In order to meet the needs of high performance materials in various industries, it is necessary to conduct more in-depth research on tribology of magnesium alloys. In particular, the tribological studies on the currently expensive alloy materials have found that the friction mechanism of these alloys is a very meaningful work.

## 1.3 Application of titanium and stainless steel materials for fuel cells and surface modification methods

### 1.3.1 Application of titanium and stainless steel for fuel cells

With the civilization of mankind, present world energy scenario reveals that within the next few decades conventional fuel resources will face severe shortage and taking into concern environmental pollution by using fossil fuel, fuel cell will be one of the most promising power sources [32] for future. Fuel cell generates electricity and heat by converting the chemical energy stored in a fuel. Depending upon the fuel used and operating conditions, fuel cells are subdivided into various types. Among all the fuel cells, proton exchange membrane (PEM) fuel cell is the most promising power sources for residential and mobile applications [33]. A recent technical cost analysis indicates that the cost of the platinum electrode accounts for about 50% of the PEM fuel cell cost, whereas the bipolar plates rank second in cost depending upon the material used and process development and leads up to 80% of the total weight [34].

The biggest challenge for the development of PEM fuel cell for automotive application is the reduction of cost and weight of the bipolar plate. Thus, widespread applications of PEM fuel cell rely heavily on both cost and weight reduction of bipolar plate. The main purposes [35] of the bipolar plates in PEM fuel cells are:

- 1) distribution of reactant gases uniformly over the active areas
- 2) collection of electrons,
- 3) connection of two adjacent cells,
- 4) heat removal from adjacent cells,
- 5) preventing leakage of reactant gases and coolant.

To achieve this goal the bipolar plate should have the following properties:

- 1) should have less porosity with high mechanical strength,
- 2) high electronic conductivity and low contact resistance,
- 3) high thermal conductivity,
- 4) integrated uniform cooling channel,
- 5) high corrosion resistance.

Due to these properties the overall efficiency of the fuel cell depends extensively on the performance of the bipolar end plates in the fuel cell stack. Today several types of materials are used [36] for the development of bipolar plates. For the development of PEMFCs, bipolar plates should have the characteristics such as high anticorrosion resistance, high electrical conductivity, lightweight, high mechanical manufacturability, high surface tension with water and low cost [37]. The traditional bipolar plate material is non-porous graphite due to its high electronic conductivity and good chemical stability in PEMFC environments. However, it is fragile to impact. Meanwhile the manufacture costs of gas flow channels are increased and the overall volume of the PEMFCs becomes bigger [15]. The graphite is not an ideal candidate for commercialization application directly. Hence the metallic bipolar plates such as stainless steel is commercially available [16]. Compared with graphite, the stainless steels have the advantages of high volumetric electrical conductivity, high mechanical strength, low gas permeability, and economic to manufacture particularly suitable for portable PEMFCs. However the stainless steel is highly vulnerable to corrosive attack in the strong acidic fuel cell environment of the electrolyte membrane with the pH value of about 2-3. The interfacial contact resistance of stainless steel material should also be considered. The other metals such as titanium and aluminum alloys show the better performances in the corrosion resistance and have

a higher mechanical strength than the stainless steel but the higher cost. The corrosion behavior of the metallic bipolar plate can degrade the fuel cell performance because the proton conductivity of the polymeric electrolyte membrane is decreased due to the poison of Fe, Cr and Ni ions.

### 1.3.2 Surface modification methods for titanium and stainless steel

Tribological coatings such as titanium nitride are usually deposited by glow- discharge, physical vapor deposition (PVD) processes such as activated reactive evaporation, cathodic arc sputtering, or magnetron sputtering [38]. In these processes coating reactants are transported to, and combined together in a glow-discharge carrier gas plasma. The reactions that occur when the reactants are combined in the glow-discharge carrier gas are driven primarily by the energetics of the glow-discharge. Therefore the metallurgical, morphological, and mechanical properties of the coatings deposited are determined by the thermodynamic environment in the glow-discharge. Once submerged in the glow-discharge the reactants cannot be controlled individually, and optimizing one coating feature such as grain size may have to be done at the expense of another feature such as density or adhesion.

The IBED process differs from the PVD process in that the reactants are not first reacted in a glow- discharge but are delivered individually directly to the surface to be coated as seen in Fig. 1-1. In addition, the energy of reaction is supplied by kinetic energy provided to one of the reactants. This provides more control over the reaction process and therefore more flexibility in the final morphology of the coating. Sacrificing one coating feature in order to optimize another is not necessary, which allows deposition of tribological coatings that perform better than the equivalent PVD-deposited coating. The

major differences between the IBED and PVD processes are summarized in Table 1. Compared with the other coating techniques, the Ion beam enhanced deposition (IBED) method has many advantages such as lower compressive stress due to the production of a graded interfacial, higher film-substrate adhesion, better surface properties of high-precision parts and be selective surface modification, which enables a series of beneficial surface property modifications without detrimentally affecting the bulk properties.

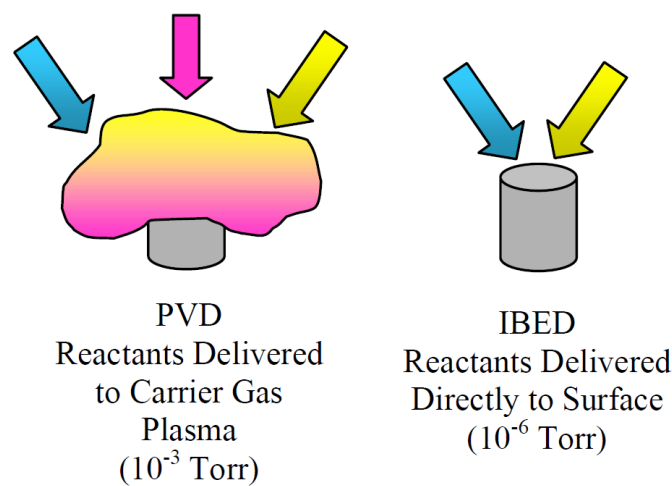


**Fig. 1- 1** Reactant delivery differences: PVD versus IBED.

The IBED process is a line-of-sight deposition process that requires three-dimensional components be manipulated to maintain proper angles relative to the reactant flux flows. The continuous part motion relative to the reactant fluxes results in deposition of coatings having very uniform thickness over the entire treated surface because all surfaces are exposed to the reactant fluxes from all angular orientations. The industrial scale IBED system currently in operation was designed and specified primarily to deposit tribological hardcoatings on precision machined parts and manufacturing tooling. System designs and specifications were developed based on a detailed analysis of the needs for tribological coatings on tools and components found in a variety of market sectors including the

automotive, truck, aircraft, aerospace, medical, and general machinery.

**Table 1- 1** IBED and PVD process comparison

<b>PVD</b>	<b>IBED</b>
<b>Reactant delivery</b>	
Into plasma atmosphere surrounding parts	Simultaneous, directly to surface of parts
<b>Reaction chemistry</b>	
Thermally driven by plasma temperature	Kinetically driven by kinetic energy of ions
<b>Reaction atmosphere (pressure)</b>	
10-3 Torr with high partial pressures of (H <sub>2</sub> , H <sub>2</sub> O, O <sub>2</sub> , CO <sub>2</sub> )	10-6 Torr with low partial pressures of (H <sub>2</sub> , H <sub>2</sub> O, O <sub>2</sub> , CO <sub>2</sub> )
<b>Reaction vessel temperature</b>	
> 400 °C	< 93 °C
<b>Coating morphology</b>	
Crystalline, grains 1-50 micron dimensions	Semi-amorphous, grains sub-micron dimensions
<b>Coating adhesion</b>	
Thermal diffusion driven, interlayer needed	Ballistic-alloyed, no interlayer needed

Some research have been investigated to protect the bare metallic bipolar plate from the highly acidic environment. Yu Fu et al. [39] prepared the carbon-based films on SUS316L substrates using pulsed bias arc ion plating (PBAIP). They found the excellent performance such as low interfacial contact resistance, high corrosion resistance and high contact angle of the coating with water compared with the bare contact angle of the sample with water substrate. The ZrCN film was deposited on titanium alloy using a

double glow discharge plasma technique by Jiang Xu et al. [40]. The film has the better electrochemical behavior, electrical conductivity, corrosion resistance and surface wettability than the uncoated titanium alloy. In addition, the preparation method of C film was introduced in the patent by Jiang Xu et al in order to achieve the thicker film and the lower electrical conductivity. Compared with the CVD techniques [41] the Ion beam enhanced deposition (IBED) method provided coatings with lower compressive stress. Depositing DLC films is one of the methods to control corrosion. To overcome these drawbacks, depositing a protective coating on the metallic bipolar plate is necessary by various surface modification techniques.

## 1.4 Performance characteristics of Diamond-Like Carbon films

### 1.4.1 DLC films

Diamond-like carbon (DLC) films are mainly amorphous carbon consisting of a network of diamond ( $sp^3$ )- and graphite ( $sp^2$ )- bonded carbon atoms as shown in Fig. 1-2. DLC films exhibit high hardness, low friction, excellent wear resistance, good biocompatibility, and optical transparency in the infrared (IR) region [42]. Liu et al. deposited a DLC film on metallic substrates using a methane ion-beam method and observed that the ultra-low wear rate was due to transfer layer formation of graphite-like carbon [43]. Wear-resistant ( $Cr_xN$ ,  $WC/a-C:H$ ,  $TiC/a-C$ ) and solid lubricant ( $Ti-MoS_2$ ) coatings were deposited on machine parts by Mutyala et al., and their tribological performance was evaluated; the authors reported that the coatings improved the life in both lubricated and unlubricated conditions [44]. Dai et al. reported that magnesium alloy coated with Cr-incorporated DLC hard films had a low internal stress and excellent

friction performance [45]. An increase in the hardness and reduction of the friction force were observed in another study in which DLC coatings were deposited on magnesium alloys, which led to improvement of the wear resistance [46]. The protection mechanism and corrosion behavior of DLC films deposited on AZ31 magnesium alloys were investigated by Choi et al. [47]. The drawbacks of poor hardness and wear resistance of the magnesium alloys were improved by depositing DLC films on the alloys. Because magnesium alloy is very soft relative to the hard DLC film, both precipitation hardening of the magnesium alloy and reinforcement of the magnesium alloy with particles have been suggested to improve the supporting effect and coating durability [48, 49]. In addition, the production of a graded interfacial layer using ion-beam-enhanced deposition (IBED) can also reduce the internal stress. The DLC film can be deposited as a protective coating on magnesium alloys using physical vapor deposition, chemical vapor deposition, and other techniques [50, 51]. The IBED method is a physical thin-film technique that achieves a high degree of precision and uniformity via the simultaneous bombardment of energetic atomic particles. Relative to chemical and thermal processes, the IBED method has many advantages when used to enhance the friction, adhesion, and other surface properties of high-precision parts, as it does not require post-coating refinish. Because the IBED augmenting ion beam is controlled independently, film properties such as the interfacial adhesion, density, grain size, and morphology as well as internal stresses can be optimized [52]. The difference between IBED and physical vapor deposition method is that the reactants are delivered individually to the surface directly in the IBED process. The energy of reaction is supplied by the kinetic energy of ions instead of the plasma temperature, which provides more control over the reaction process and more flexibility in the film properties. High-energy ions, such as Ar<sup>+</sup> or N<sup>+</sup>, cause the initial few atomic

layers of the film material to mix into the surface. Then, an alloyed bond layer is formed to promote adhesion of the film. Film–substrate adhesion is achieved without the external application of heat, and processing temperatures can be held below 93°C (200°F); therefore, no physical dimensions are produced [38]. Accordingly, the primary advantage of IBED is selective surface modification, which enables a series of beneficial surface property modifications without detrimentally affecting the bulk properties [53].

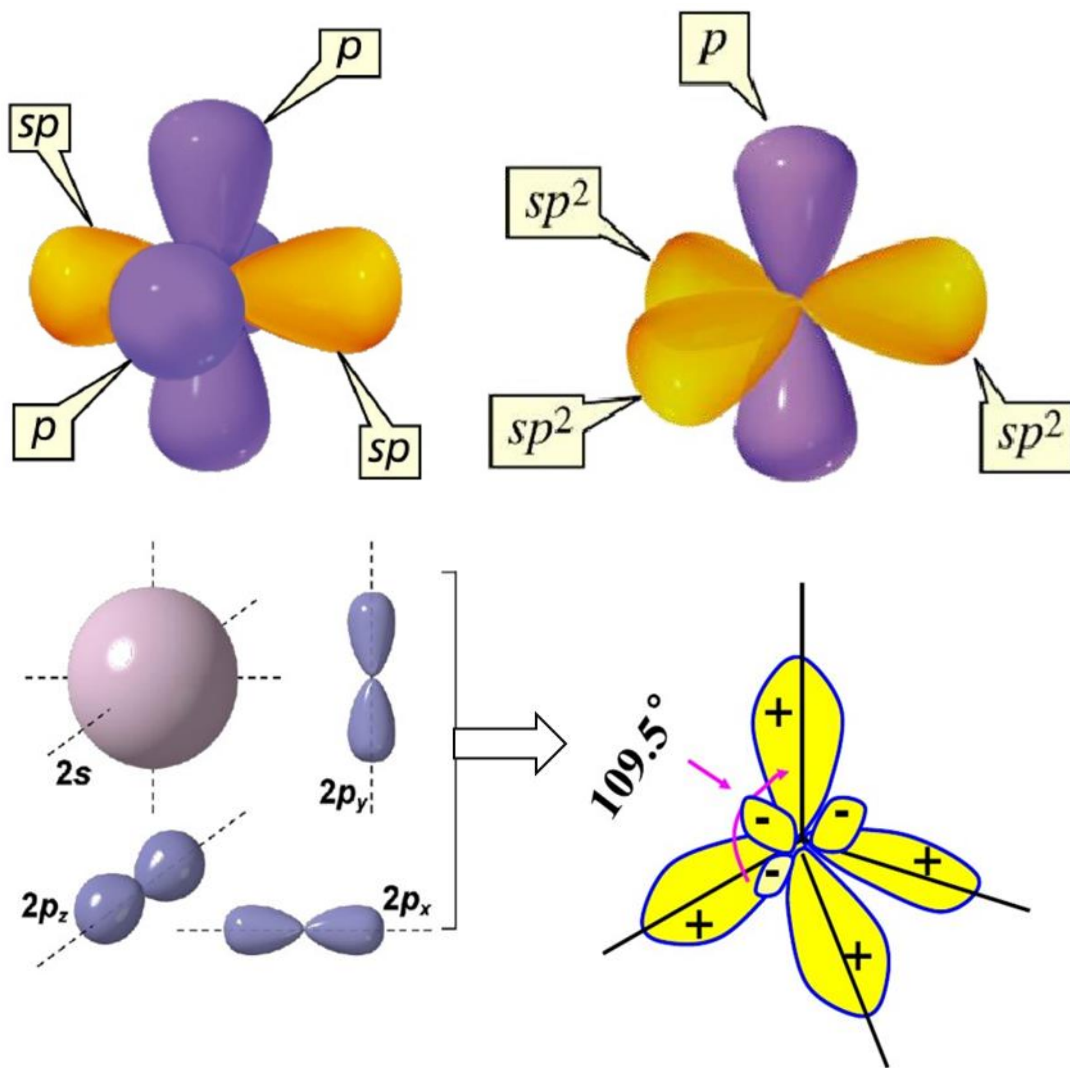


**Fig. 1- 2** Structure of (a) $sp$  hybrid carbon atom; (b)  $sp^2$  hybrid carbon atom; (c)  $sp^3$  hybrid carbon atom;

In the last 10 years DLC film have gained special attention due to their properties such as low friction coefficient, high chemical stability, high hardness, optical transparency, high electrical resistivity and low electron affinity [54, 55]. Thereby they can be used in optoelectronic devices, protective films for tribological or chemical applications, automotive parts and tools, coatings for dies or molds and biological parts. In this paper, the friction property and corrosion property were analyzed.

An important factor affecting the hardness of the film is the content of the hybrid bond  $sp^3$  [56]. In general, the higher the content of the hybrid bond  $sp^3$ , the closer the hardness of the film is to diamond [57]. Since the structure and composition of the film obtained by different preparation methods are different, the hardness of the film can be adjusted within a wide range, and the highest hardness can reach 90 GPa. However, the problem of internal stress is also considered. The high hardness of the film is always accompanied by a high internal stress, and the excessive internal stress causes the wear resistance of the film to be seriously reduced, thereby seriously affecting the mechanical properties of the film. At present, researchers use doping N, Si, Cr and other elements in the film to perform low-temperature short-time heat treatment or to prepare a gradient film to reduce the internal stress of the film.

Due to its high hardness, low coefficient of friction and good thermal conductivity, the DLC film can be used as a wear-resistant coating in the field of tribology [58]. After evaluating the various solid materials used in space in 1990, the European Space Center Friction Laboratory pointed out that the most important thing in the future is the development of thin films as coatings for future spatially lubricated friction surfaces [59]. Due to its anti-wear and chemical stability properties, the film is used as a coating for future space-lubricated friction surfaces [60] and is suitable for wear-resistant layers of

consumable parts such as bearings and gears [61, 62]. The film has good chemical stability, prevents acid and alkali and organic solution erosion, and is suitable for chemical mechanical parts and coatings of various decorative parts without changing the size of mechanical parts.

Harbin Institute of Technology used plasma immersion ion implantation and deposition technology to deposit the film on the aerospace space flywheel bearings [63-65]. The results show that the film's stable friction coefficient is only 1/3 of the substrate, and the surface friction and wear performance is greatly improved, which is beneficial to extend the life expectancy of the space flywheel bearing. In order to solve the problem of high wear of cutting tools in the wet environment of wood processing, the oxygen-free and anaerobic films were deposited on low-alloy working steel using the PVD method by Wolfgang et al [66]. It was found that the oxygen-free film in the humid environment showed excellent wear resistance. The IBM Company has developed a micro-drilled film-coated micro-drill for drilling fine holes in the circuit board [67, 68]. It has been found that the drilling speed of the micro-drill increases the service life by a factor of two, and the processing cost of the drill is reduced. Some scholars have succeeded in depositing films on wearable mechanical components such as automobile engine parts, plates, nails, etc. [69, 70], and the friction coefficient is 0.14.

#### 1.4.2 Problems of DLC films-coated metal substrate

Magnesium alloys have a problem of poor hardness, abrasion resistance and corrosion resistance, which restrict their more extensive application. Therefore, depositing a DLC film to modify material surfaces is an effective means to improve these properties to use magnesium for more machine parts [71-73].

For the development of PEMFCs [74-77], bipolar plates should have the characteristics such as high anticorrosion resistance, high electrical conductivity, lightweight, high mechanical manufacturability, high surface tension with water and low cost [78]. The traditional bipolar plate material is non-porous graphite [79]. However, it is fragile to impact. Meanwhile the manufacture costs of gas flow channels are increased and the overall volume of the PEMFCs becomes bigger. The graphite is not an ideal candidate for commercialization application directly. Hence the metallic bipolar plates such as stainless steel and titanium is commercially available. Compared with graphite, the stainless steels have the advantages of high volumetric electrical conductivity, high mechanical strength, low gas permeability, and economic to manufacture particularly suitable for portable PEMFCs [14, 74]. However the stainless steel is highly vulnerable to corrosive attack in the strong acidic fuel cell environment of the electrolyte membrane with the pH value of about 2-3 [80]. The interfacial contact resistance of stainless steel material should also be considered. The other metals such as titanium and aluminum alloys show the better performances in the corrosion resistance and have a higher mechanical strength than the stainless steel but the higher cost. The corrosion behavior of the metallic bipolar plate can degrade the fuel cell performance because the proton conductivity of the polymeric electrolyte membrane is decreased due to the poison of Fe, Cr and Ni ions [81-83].

## 1.5 Thesis objective and structure

The figure 1-3 shows the overview of the thesis. In this study, different DLC films were deposited using IBED by changing the CH<sub>4</sub>/H<sub>2</sub> gas flow rate and accelerating voltage for surface modification, and the composition and mechanical properties of the DLC coatings were analyzed. The purpose of this study was to improve the surface performance of

magnesium alloy AZ31 by enhancing the hardness and wear-resistance capacity of the DLC coating.

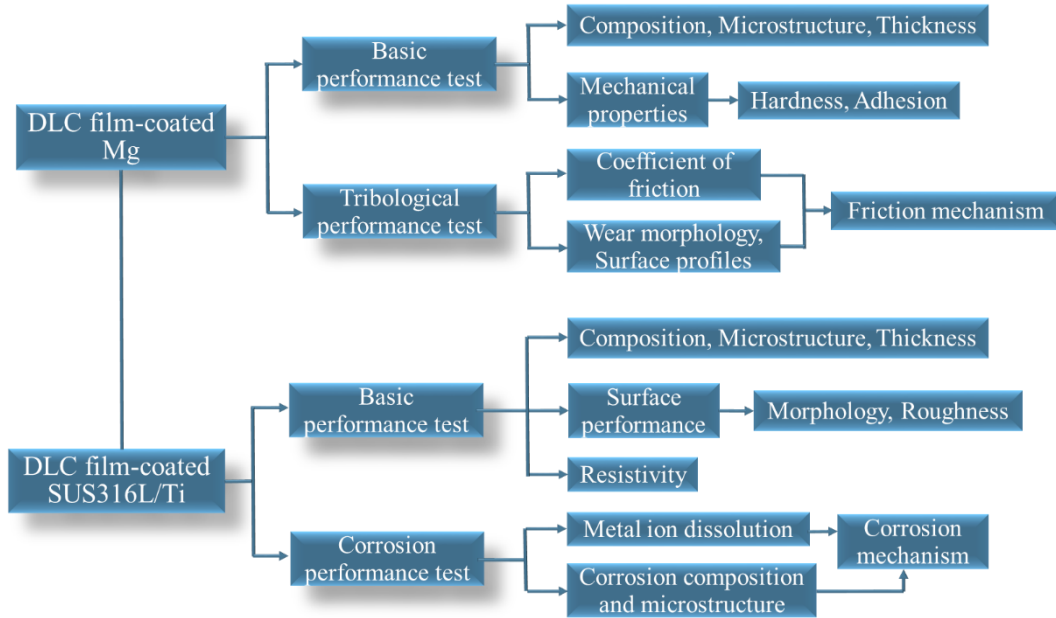


**Fig. 1- 3** Overview of the thesis

316L stainless steel and titanium substrates were coated with amorphous hydrogenated carbon (a-C:H) films [84] by Ion beam enhanced deposition (IBED) technique. The characterizations and corrosion behaviors of the DLC coated stainless steel deposited with different gas ratios CH<sub>4</sub>/H<sub>2</sub> and deposition times were investigated and evaluated. The chemical bonding structure and composition of the DLC coatings were analyzed. The purpose of this study is to evaluate the anti-corrosion properties of the stainless steel and titanium substrates.

The first step is to understand the application of metal substrates, the background and significance of Diamond-Like Carbon films.

Chapter 2 describes the experimental methods and principle.

Chapter 3 focuses on surface characteristics and tribological properties of DLC films on magnesium alloy.

Chapter 4 consists of microstructure analysis and corrosion resistance of DLC films-coated titanium.

Chapter 5 explains chemical composition and corrosion behavior of DLC films-coated stainless steel.

Lastly, Chapter 6 concludes the thesis and summarizes the work.

## References

- [1] I. Hutchings and P. Shipway, *Tribology: friction and wear of engineering materials*. Butterworth-Heinemann, 2017.
- [2] R. G. Bayer, "Mechanical wear prediction and prevention," *Marcel! Dekker, Inc, P. O. Box 5005, Monticello, NY 12701-5185, USA, 1994. 657*, 1994.
- [3] M. Godet, "The third-body approach: a mechanical view of wear," *Wear*, vol. 100, no. 1-3, pp. 437-452, 1984.
- [4] Y. Song, Y. Liu, S. Yu, X. Zhu, and Q. Wang, "Plasma electrolytic oxidation coating on AZ91 magnesium alloy modified by neodymium and its corrosion resistance," *Applied Surface Science*, vol. 254, no. 10, pp. 3014-3020, 2008.
- [5] A. Ghasemi, V. Raja, C. Blawert, W. Dietzel, and K. Kainer, "Study of the structure and corrosion behavior of PEO coatings on AM50 magnesium alloy by electrochemical impedance spectroscopy," *Surface and Coatings Technology*, vol. 202, no. 15, pp. 3513-3518, 2008.
- [6] J. D. Majumdar, R. Galun, B. Mordike, and I. Manna, "Effect of laser surface melting on corrosion and wear resistance of a commercial magnesium alloy," *Materials Science and Engineering: A*, vol. 361, no. 1-2, pp. 119-129, 2003.
- [7] H. Hintermann, "Adhesion, friction and wear of thin hard coatings," *Wear*, vol. 100, no. 1-3, pp. 381-397, 1984.
- [8] B. Kakati and V. Mohan, "Development of Low-Cost Advanced Composite Bipolar Plate for Proton Exchange Membrane Fuel Cell," *Fuel Cells*, vol. 8, no. 1, pp. 45-51, 2008.
- [9] J. Hwang, W. Chang, F. Weng, A. Su, and C. o.-K. Chen, "Development of a small vehicular PEM fuel cell system," *International Journal of Hydrogen Energy*, vol. 33, no. 14, pp. 3801-3807, 2008.
- [10] O. Savadago and B. Xing, "Hydrogen/oxygen polymer electrolyte membrane fuel cell (PEMFC) based on acid doped poly benzimidazole (PBI)," *J New Mater Electrochem Syst*, vol. 3, p. 345, 2000.
- [11] Y. Wang, K. S. Chen, J. Mishler, S. C. Cho, and X. C. Adroher, "A review of polymer electrolyte membrane fuel cells: technology, applications, and needs on fundamental research," *Applied energy*, vol. 88, no. 4, pp. 981-1007, 2011.
- [12] X.-Z. Yuan, C. Song, H. Wang, and J. Zhang, "PEM fuel cells and their related electrochemical fundamentals," *Electrochemical Impedance Spectroscopy in PEM Fuel Cells: Fundamentals and Applications*, pp. 1-37, 2010.
- [13] H. Wang and J. Turner, "Reviewing metallic PEMFC bipolar plates," *Fuel Cells*,

- vol. 10, no. 4, pp. 510-519, 2010.
- [14] H. Wang, M. A. Sweikart, and J. A. Turner, "Stainless steel as bipolar plate material for polymer electrolyte membrane fuel cells," *Journal of Power Sources*, vol. 115, no. 2, pp. 243-251, 2003.
- [15] R. A. Antunes, M. C. L. Oliveira, G. Ett, and V. Ett, "Corrosion of metal bipolar plates for PEM fuel cells: a review," *International journal of hydrogen energy*, vol. 35, no. 8, pp. 3632-3647, 2010.
- [16] E. Cho, U.-S. Jeon, S.-A. Hong, I.-H. Oh, and S.-G. Kang, "Performance of a 1 kW-class PEMFC stack using TiN-coated 316 stainless steel bipolar plates," *Journal of Power Sources*, vol. 142, no. 1-2, pp. 177-183, 2005.
- [17] J. R. Mawdsley *et al.*, "Composite-coated aluminum bipolar plates for PEM fuel cells," *Journal of Power Sources*, vol. 231, pp. 106-112, 2013.
- [18] M. M. Avedesian and H. Baker, "ASM speciality handbook: magnesium and magnesium alloys," *ASM international*, vol. 59, p. 60, 1999.
- [19] B. Mordike and T. Ebert, "Magnesium: Properties—applications—potential," *Materials Science and Engineering: A*, vol. 302, no. 1, pp. 37-45, 2001.
- [20] Z. Zhang *et al.*, "Studies on influence of zinc immersion and fluoride on nickel electroplating on magnesium alloy AZ91D," *Applied Surface Science*, vol. 255, no. 17, pp. 7773-7779, 2009.
- [21] S. Agnew, M. Yoo, and C. Tome, "Application of texture simulation to understanding mechanical behavior of Mg and solid solution alloys containing Li or Y," *Acta Materialia*, vol. 49, no. 20, pp. 4277-4289, 2001.
- [22] F. Stapleton *et al.*, "Risk factors for moderate and severe microbial keratitis in daily wear contact lens users," *Ophthalmology*, vol. 119, no. 8, pp. 1516-1521, 2012.
- [23] N. Welsh, "The dry wear of steels I. The general pattern of behaviour," *Philosophical Transactions for the Royal Society of London. Series A, Mathematical and Physical Sciences*, pp. 31-50, 1965.
- [24] A. W. Batchelor and G. W. Stachowiak, "Tribology in materials processing," *Journal of materials processing technology*, vol. 48, no. 1-4, pp. 503-515, 1995.
- [25] M. Khruschov, "Principles of abrasive wear," *wear*, vol. 28, no. 1, pp. 69-88, 1974.
- [26] A. Kumar, J. Bijwe, and S. Sharma, "Hard metal nitrides: Role in enhancing the abrasive wear resistance of UHMWPE," *Wear*, vol. 378, pp. 35-42, 2017.
- [27] J. Challen, P. Oxley, and B. Hockenhull, "Prediction of Archard's wear coefficient for metallic sliding friction assuming a low cycle fatigue wear mechanism," *Wear*, vol. 111, no. 3, pp. 275-288, 1986.

- [28] Y. Berthier, L. Vincent, and M. Godet, "Fretting fatigue and fretting wear," *Tribology international*, vol. 22, no. 4, pp. 235-242, 1989.
- [29] C. T. d. Santos, C. Barbosa, M. d. J. Monteiro, I. d. C. Abud, I. M. V. Caminha, and C. R. d. M. Roesler, "Fretting corrosion tests on orthopedic plates and screws made of ASTM F138 stainless steel," *Research on Biomedical Engineering*, vol. 31, no. 2, pp. 169-175, 2015.
- [30] M. Gee, A. Gant, and B. Roebuck, "Wear mechanisms in abrasion and erosion of WC/Co and related hardmetals," *Wear*, vol. 263, no. 1-6, pp. 137-148, 2007.
- [31] E. Trent, "Some factors affecting wear on cemented carbide tools," *Proceedings of The Institution of Mechanical Engineers*, vol. 166, no. 1, pp. 64-74, 1952.
- [32] J. Fuller, R. T. Carlin, and R. A. Osteryoung, "The room temperature ionic liquid 1-ethyl-3-methylimidazolium tetrafluoroborate: electrochemical couples and physical properties," *Journal of the Electrochemical Society*, vol. 144, no. 11, pp. 3881-3886, 1997.
- [33] Z. Jie, Z. Yan-wen, and H. Jun, "Influence of graphite particle size and its shape on performance of carbon composite bipolar plate," *Journal of Zhejiang University-SCIENCE A*, vol. 6, no. 10, pp. 1080-1083, 2005.
- [34] I. Bar-On, R. Kirchain, and R. Roth, "Technical cost analysis for PEM fuel cells," *Journal of Power Sources*, vol. 109, no. 1, pp. 71-75, 2002.
- [35] V. Mehta and J. S. Cooper, "Review and analysis of PEM fuel cell design and manufacturing," *Journal of Power Sources*, vol. 114, no. 1, pp. 32-53, 2003.
- [36] E. Middelmann, W. Kout, B. Vogelaar, J. Lenssen, and E. De Waal, "Bipolar plates for PEM fuel cells," *Journal of Power Sources*, vol. 118, no. 1-2, pp. 44-46, 2003.
- [37] K. Feng, X. Cai, H. Sun, Z. Li, and P. K. Chu, "Carbon coated stainless steel bipolar plates in polymer electrolyte membrane fuel cells," *Diamond and Related Materials*, vol. 19, no. 11, pp. 1354-1361, 2010.
- [38] A. H. Deutchman and R. J. Partyka, "Industrial Scale Ion Beam Enhanced Deposition (IBED) Processing System," in *Proceedings: ASM International Surface Engineering Congress*, 2002, pp. 1-9.
- [39] K. Feng, D. T. Kwok, D. Liu, Z. Li, X. Cai, and P. K. Chu, "Nitrogen plasma-implanted titanium as bipolar plates in polymer electrolyte membrane fuel cells," *Journal of Power Sources*, vol. 195, no. 19, pp. 6798-6804, 2010.
- [40] Y. Fu, G. Lin, M. Hou, B. Wu, Z. Shao, and B. Yi, "Carbon-based films coated 316L stainless steel as bipolar plate for proton exchange membrane fuel cells," *International Journal of hydrogen energy*, vol. 34, no. 1, pp. 405-409, 2009.
- [41] K. E. Spear and J. P. Dismukes, *Synthetic diamond: emerging CVD science and*

- technology*. John Wiley & Sons, 1994.
- [42] G. Ma, S. Gong, G. Lin, L. Zhang, and G. Sun, "A study of structure and properties of Ti-doped DLC film by reactive magnetron sputtering with ion implantation," *Applied Surface Science*, vol. 258, no. 7, pp. 3045-3050, 2012.
- [43] Y. Liu, A. Erdemir, and E. Meletis, "A study of the wear mechanism of diamond-like carbon films," *Surface and Coatings Technology*, vol. 82, no. 1-2, pp. 48-56, 1996.
- [44] K. C. Mutyala, H. Singh, R. Evans, and G. Doll, "Deposition, characterization, and performance of tribological coatings on spherical rolling elements," *Surface and Coatings Technology*, vol. 284, pp. 302-309, 2015.
- [45] W. Dai, G. Wu, and A. Wang, "Preparation, characterization and properties of Cr-incorporated DLC films on magnesium alloy," *Diamond and Related Materials*, vol. 19, no. 10, pp. 1307-1315, 2010.
- [46] G. Wu, W. Dai, H. Zheng, and A. Wang, "Improving wear resistance and corrosion resistance of AZ31 magnesium alloy by DLC/AlN/Al coating," *Surface and Coatings Technology*, vol. 205, no. 7, pp. 2067-2073, 2010.
- [47] J. Choi, J. Kim, S. Nakao, M. Ikeyama, and T. Kato, "Friction properties of protective DLC films on magnesium alloy in aqueous NaCl solution," *Nuclear Instruments and Methods in Physics Research Section B: Beam Interactions with Materials and Atoms*, vol. 257, no. 1-2, pp. 718-721, 2007.
- [48] Y. Harada and S. Kumai, "Effect of ceramics coating using sol-gel processing on corrosion resistance and age hardening of AZ80 magnesium alloy substrate," *Surface and Coatings Technology*, vol. 228, pp. 59-67, 2013.
- [49] Z. Szaraz, Z. Trojanova, M. Cabbibo, and E. Evangelista, "Strengthening in a WE54 magnesium alloy containing SiC particles," *Materials Science and Engineering: A*, vol. 462, no. 1-2, pp. 225-229, 2007.
- [50] J. Liang, P. Wang, L. Hu, and J. Hao, "Tribological properties of duplex MAO/DLC coatings on magnesium alloy using combined microarc oxidation and filtered cathodic arc deposition," *Materials Science and Engineering: A*, vol. 454, pp. 164-169, 2007.
- [51] H. Sun, Y.-N. Shi, and M.-X. Zhang, "Wear behaviour of AZ91D magnesium alloy with a nanocrystalline surface layer," *Surface and Coatings Technology*, vol. 202, no. 13, pp. 2859-2864, 2008.
- [52] A. H. Deutchman and R. J. Partyka, "Ion Beam Enhanced Deposited (IBED) Tribological Coatings for Non-Ferrous Alloys," in *Proceedings from the 1st International Surface Engineering Congress and the 13th IFHTSE Congress*,

- 2002, pp. 7-10.
- [53] P. Sioshansi and E. J. Tobin, "Surface treatment of biomaterials by ion beam processes," *Surface and coatings Technology*, vol. 83, no. 1-3, pp. 175-182, 1996.
  - [54] H.-J. Scheibe and B. Schultrich, "DLC film deposition by laser-arc and study of properties," *Thin Solid Films*, vol. 246, no. 1-2, pp. 92-102, 1994.
  - [55] M. Morshed, B. McNamara, D. Cameron, and M. Hashmi, "Effect of surface treatment on the adhesion of DLC film on 316L stainless steel," *Surface and Coatings Technology*, vol. 163, pp. 541-545, 2003.
  - [56] S. Praver *et al.*, "Systematic variation of the Raman spectra of DLC films as a function of sp<sup>2</sup>: sp<sup>3</sup> composition," *Diamond and related materials*, vol. 5, no. 3-5, pp. 433-438, 1996.
  - [57] T. FC and T. SL, "Correlation between ID/IG ratio from visible Raman spectra and sp<sup>2</sup>/sp<sup>3</sup> ratio from XPS spectra of annealed hydrogenated DLC film," *Materials transactions*, vol. 47, no. 7, pp. 1847-1852, 2006.
  - [58] R. Chattopadhyay, *Surface wear: analysis, treatment, and prevention*. ASM international, 2001.
  - [59] S. B. Johnson, *The secret of Apollo: systems management in American and European space programs*. JHU Press, 2002.
  - [60] Y. D. W. L. O. Jinlin, "Recent Progress of the Space Mechanism Lubrication [J]," *摩擦学学报*, vol. 1, 1996.
  - [61] A. Bloyce, "Surface engineering of titanium alloys for wear protection," *Proceedings of the Institution of Mechanical Engineers, Part J: Journal of Engineering Tribology*, vol. 212, no. 6, pp. 467-476, 1998.
  - [62] C. Y. Qiao and T. Trudeau, "Corrosion and wear resistant alloy," ed: Google Patents, 2004.
  - [63] J. Z. Z. H. S. Ruipeng and H. Lixia, "Study on Surface Modification Technology with Ion Implantation for the Materials Used for Space Gear Transmission Pairs," *Lubrication Engineering*, vol. 12, p. 011, 2011.
  - [64] L. Zhaoguang, Z. Renji, Y. Yu, and W. Langping, "Surface Modification of Aerospace Flywheel-Bearings by Nitrogen Plasma Immersion Ion Implantation," *Chinese Journal of Vacuum Science and Technology*, vol. 3, p. 016, 2011.
  - [65] Z. LI, R. ZHANG, L. WANG, J. PENG, and G. ZHOU, "Research on Improvement of Surface Treatment Process of Aerospace Flywheel Bearing by Diamond-like Carbon," *New Technology & New Process*, vol. 8, p. 036, 2010.
  - [66] M. Peters, C. Leyens, U. Schulz, and W. A. Kaysser, "EB-PVD thermal barrier coatings for aeroengines and gas turbines," *Advanced Engineering Materials*, vol.

- 3, no. 4, pp. 193-204, 2001.
- [67] M. Hasan, J. Zhao, and Z. Jiang, "A review of modern advancements in micro drilling techniques," *Journal of Manufacturing Processes*, vol. 29, pp. 343-375, 2017.
- [68] L. Zheng, C. Wang, X. Zhang, Y. Song, L. Zhang, and K. Wang, "The entry drilling process of flexible printed circuit board and its influence on hole quality," *Circuit World*, vol. 41, no. 4, pp. 147-153, 2015.
- [69] J. Pretlove, C. Skourup, P. Öberg, T. Pettersen, and C. Apneseth, "Method to generate a human machine interface," ed: Google Patents, 2010.
- [70] J. L. Kaschmitter and I. W. Kaye, "Disposable component on a fuel cartridge and for use with a portable fuel cell system," ed: Google Patents, 2010.
- [71] N. Yamauchi, K. Demizu, N. Ueda, N. Cuong, T. Sone, and Y. Hirose, "Friction and wear of DLC films on magnesium alloy," *Surface and Coatings Technology*, vol. 193, no. 1-3, pp. 277-282, 2005.
- [72] I. Shigematsu, M. Nakamura, N. Saitou, and K. Shimojima, "Surface treatment of AZ91D magnesium alloy by aluminum diffusion coating," *Journal of Materials Science Letters*, vol. 19, no. 6, pp. 473-475, 2000.
- [73] B. Hu, K. Tong, X. P. Niu, and I. Pinwill, "Design and optimisation of runner and gating systems for the die casting of thin-walled magnesium telecommunication parts through numerical simulation," *Journal of Materials Processing Technology*, vol. 105, no. 1-2, pp. 128-133, 2000.
- [74] H. Tawfik, Y. Hung, and D. Mahajan, "Metal bipolar plates for PEM fuel cell—a review," *Journal of power sources*, vol. 163, no. 2, pp. 755-767, 2007.
- [75] S. Joseph, J. McClure, R. Chianelli, P. Pich, and P. Sebastian, "Conducting polymer-coated stainless steel bipolar plates for proton exchange membrane fuel cells (PEMFC)," *International Journal of Hydrogen Energy*, vol. 30, no. 12, pp. 1339-1344, 2005.
- [76] X. Li and I. Sabir, "Review of bipolar plates in PEM fuel cells: Flow-field designs," *International Journal of Hydrogen Energy*, vol. 30, no. 4, pp. 359-371, 2005.
- [77] J. S. Cooper, "Design analysis of PEMFC bipolar plates considering stack manufacturing and environment impact," *Journal of Power Sources*, vol. 129, no. 2, pp. 152-169, 2004.
- [78] E. Cho, U.-S. Jeon, H. Ha, S.-A. Hong, and I.-H. Oh, "Characteristics of composite bipolar plates for polymer electrolyte membrane fuel cells," *Journal of Power Sources*, vol. 125, no. 2, pp. 178-182, 2004.

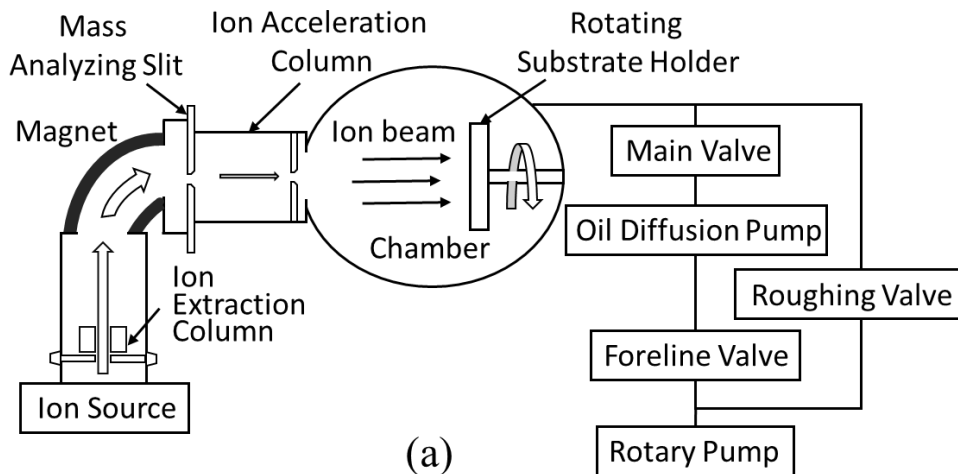
- [79] J. Scholta, B. Rohland, V. Trapp, and U. Focken, "Investigations on novel low-cost graphite composite bipolar plates," *Journal of Power Sources*, vol. 84, no. 2, pp. 231-234, 1999.
- [80] M. Kumagai, S.-T. Myung, S. Kuwata, R. Asaishi, and H. Yashiro, "Corrosion behavior of austenitic stainless steels as a function of pH for use as bipolar plates in polymer electrolyte membrane fuel cells," *Electrochimica Acta*, vol. 53, no. 12, pp. 4205-4212, 2008.
- [81] M. P. Brady *et al.*, "Preferential thermal nitridation to form pin-hole free Cr-nitrides to protect proton exchange membrane fuel cell metallic bipolar plates," *Scripta Materialia*, vol. 50, no. 7, pp. 1017-1022, 2004.
- [82] M. P. Brady *et al.*, "Growth of Cr-Nitrides on commercial Ni–Cr and Fe–Cr base alloys to protect PEMFC bipolar plates," *International Journal of Hydrogen Energy*, vol. 32, no. 16, pp. 3778-3788, 2007.
- [83] Y. Wang and D. O. Northwood, "Effects of O<sub>2</sub> and H<sub>2</sub> on the corrosion of SS316L metallic bipolar plate materials in simulated anode and cathode environments of PEM fuel cells," *Electrochimica Acta*, vol. 52, no. 24, pp. 6793-6798, 2007.
- [84] J. Schwan, W. Dworschak, K. Jung, and H. Ehrhardt, "Microstructures and mechanical properties of amorphous hydrogenated carbon-nitrogen films," *Diamond and Related Materials*, vol. 3, no. 7, pp. 1034-1039, 1994.

# Chapter 2 Experimental methods and principle

## 2.1 Preparation of DLC films

### 2.1.1 Experimental materials and substrate processing

The substrate material used in this experiment was AZ31 (Mg–3.3%Al–0.6%Zn–0.28%Mn) magnesium alloy, stainless steel SUS316L (Cr 18 wt.%, Ni 12 wt.%, Mo 1.3 wt.%, C 0.01 wt.%, balanced Fe) and titanium. The size of the magnesium alloy substrate was 15 mm (L) × 15 mm (W) × 3 mm (H). The size of the stainless steel and titanium substrate were 100 mm (L) × 100 mm (W) × 0.1 mm (H). All the magnesium alloy samples were ground with abrasive paper (400# → 600# → 800# → 1200#). After semi-finishing, fine polishing was performed using a polishing cloth and diamond paste. The grinding sequence was 9 μm (1800#) → 6 μm (3000#) → 3 μm (8000#). Then, the magnesium alloy, stainless steel and titanium samples were ultrasonically cleaned in ethanol for 10 min to remove any contamination from grease before being dried with air. Finally, the samples were fixed onto the substrate holder in the ion implantation system chamber, as shown in Figure 2-1(a).



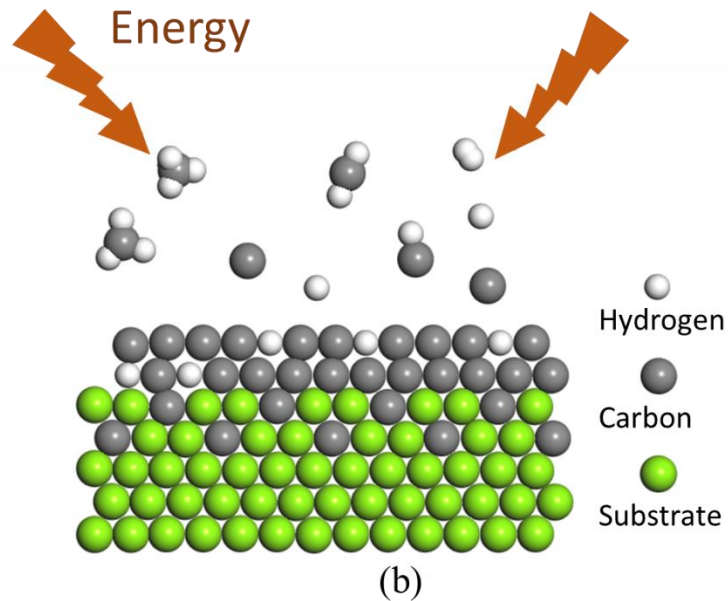


**Fig. 2-1** Schematic diagram of ion implantation system (a) and IBED process (b)

### 2.1.2 Deposition of DLC films on different substrates

The IBED method is a physical thin-film technique that achieves a high degree of precision and uniformity via the simultaneous bombardment of energetic atomic particles. Relative to chemical and thermal processes, the IBED method has many advantages when used to enhance the friction, adhesion, and other surface properties of high-precision parts, as it does not require post-coating refinish. Because the IBED augmenting ion beam is controlled independently, film properties such as the interfacial adhesion, density, grain size, and morphology as well as internal stresses can be optimized [1]. The difference between IBED and physical vapor deposition method is that the reactants are delivered individually to the surface directly in the IBED process. The energy of reaction is supplied by the kinetic energy of ions instead of the plasma temperature, which provides more control over the reaction process and more flexibility in the film properties. High-energy ions, such as  $\text{Ar}^+$  or  $\text{N}^+$ , cause the initial few atomic layers of the film material to

mix into the surface. Then, an alloyed bond layer is formed to promote adhesion of the film. Film–substrate adhesion is achieved without the external application of heat, and processing temperatures can be held below 93°C (200°F); therefore, no physical dimensions are produced [2]. Accordingly, the primary advantage of IBED is selective surface modification, which enables a series of beneficial surface property modifications without detrimentally affecting the bulk properties [3].

Schematic diagrams of the ion implantation system and IBED process are presented in Figure 2-1(a) and (b), respectively. In the first stage, the hydrocarbon gas is ionized and extracted through a grid by an accelerating voltage. Then the ionized hydrocarbon ions are accelerated to form ion beam. The film atoms penetrate the surface of the substrate to form the case layer. Upon implantation of the ions, they convey substantial energy to the film for substrate heating. The process of substrate heating provides a denser and more uniform coating. In addition, the energetic atomic particles interact with film atoms, drive them into the substrate, and produce a graded interface to improve the adhesion. In the second stage, the film atoms grow out from the graded interface to form the growing DLC film by ion-beam bombardment, as illustrated in Figure 1(b). Several reactions, electron-neutral, ion-neutral and neutral-neutral reactions, are taken place in plasma. These different species of positive ions, radicals and other hydrocarbon are generated in these reactions. There are several surface processes such as adsorption, desorption, direct incorporation of ions, reemission of H, ion-induced incorporation of neutral radicals, adsorbed layer reactions, surface etching reactions and sputtering in the species deposition of DLC film. The neutral species promote DLC film growth due to the ions mass deposition rate [4]. The most species in plasma and these species that contribute more to DLC growth are  $\text{CH}_5^+$  and  $\text{CH}_3^+$  ions. The film comprises a fully dense coating

and a ballistically bonded zone, ie a permeation layer. In the IBED process, high-energy ions mix the initial atom layers of the film material into the surface being coated. It forms an alloyed bond layer which improves coating adhesion and allows coatings to be applied to virtually any substrate without an intermediate layer. The coating grows from alloyed layer and the high-energy ion flux controls the coating's grain structure, density and residual stresses [1, 2].

The deposition of the DLC films was performed using IBED with CH<sub>4</sub> and H<sub>2</sub> sources. Before the deposition, the chamber was evacuated to a base pressure of 4×10<sup>-4</sup> Pa to produce plasma discharge. Then, the CH<sub>4</sub> and H<sub>2</sub> mixture was injected into the chamber. The ratio of CH<sub>4</sub>/H<sub>2</sub> was 99:1, 1:99 and 1:1. The chamber pressure changed as the gas was injected; therefore, the chamber pressure was fixed at 0.8×10<sup>-3</sup> Pa using the pressure valve. During the deposition process, the ion beam interacted with the substrate via the accelerator, which was generated from the CH<sub>4</sub> and H<sub>2</sub> mixture. For all the magnesium alloy samples, the current and deposition time were fixed at 40 mA and 4 h, respectively. Accelerating voltages of 6 and 9 kV and total gas flows of 3, 6, and 9 sccm were applied. For the stainless steel and titanium samples, the anode, accelerating voltage, current and gas flow was fixed at 40 mA, 10 kV, 2.5 mA and 0.4~0.5 sccm, respectively. Deposition time of 6 and 12 hrs were applied. Finally, the DLC coating with high adhesion was deposited. All the samples were cooled down inside the chamber after processing. The detailed experimental conditions are listed in Table 2-1.

**Table 2- 1** Parameters for different processing conditions

(a)	Mg	
Gas ratio (CH <sub>4</sub> /H <sub>2</sub> )	CH <sub>4</sub> /H <sub>2</sub> = 99:1	CH <sub>4</sub> /H <sub>2</sub> = 1:99

Gas flow (sccm)	3	6	9	3	6	9	3	6	9
Accelerating Voltage (kV)	6	6	6	9	9	9	6	6	6

(b)	SUS316L			Ti				
Gas ratio (CH <sub>4</sub> /H <sub>2</sub> )	1:1	1:1	1:0	1:0	1:1	1:1	1:0	1:0
Time (hrs)	6	12	6	12	6	12	6	12

## 2.2 Experimental analysis methods

### 2.2.1 Raman analysis

Schematic presentation of Raman spectroscopy instrument is shown in figure 2-2. When excitation light irradiates (green line), Rayleigh scattering (blue line) and Raman scattering (red dotted line) are released. Rayleigh scattering is filtered, and pure Raman scattering is detected [5].

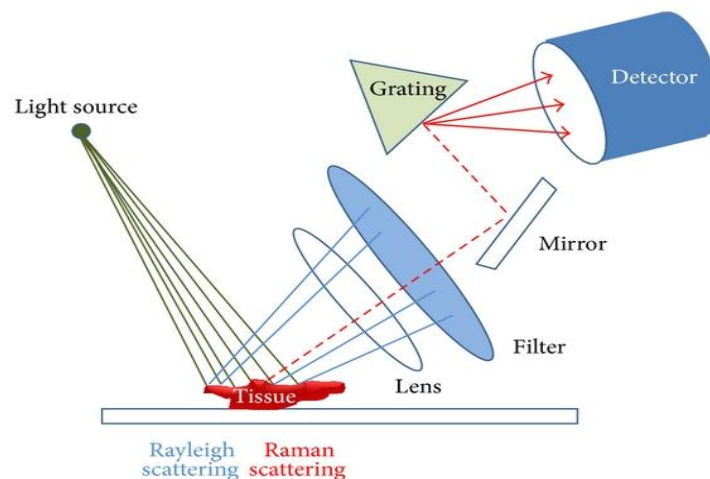


**Fig. 2- 2** Schematic diagram of Raman analysis

Raman spectroscopy is mainly used to identify molecular structures and materials. Because of its high resolution to various carbon isomers, Raman spectroscopy is widely used to identify the structure of diamond, graphite, diamond-like and carbon nanotubes [6, 7]. It is a traditional, non-destructive means of analyzing carbon structures. The principle of Raman spectroscopy is that photons collide with the extranuclear electrons of matter, and use the information obtained by elastic scattering to analyze the structure of matter. When a high-frequency  $\nu_0$  monochromatic laser beam hits a substance molecule, the frequency of the partially scattered light is different from the frequency of the incident light. The energy of the scattered light is  $h(\nu_0-\nu_1)$  or  $h(\nu_0+\nu_1)$ , The lost energy or obtained energy  $h\nu_1$  is equivalent to the vibration energy. This effect is called the Raman effect and the resulting spectrum is called Raman spectroscopy.  $h\nu_1$  is called Raman shift. The Raman spectrum gives the structure of the near surface of the carbon material. In this paper the detailed bonding structure of the DLC film was analyzed using Raman spectroscopy (NRS-4100) with a laser wavelength of 532.0 nm, spot size of  $\Phi 34 \mu\text{m}$ , and laser power of 0.03 mW.

### 2.2.2 Micromorphology analysis

The Atomic Force Microscope (AFM) is comprised of a cantilever-tip assembly that raster scans across the sample surface using a piezoelectric tube controlled by a computer. The cantilever tip tapers to a very sharp point, typically less than 10nm radius of curvature [8]. The deflection of the cantilever is monitored using an optical detection system in the form of a laser that reflects off the back of the cantilever and onto a four quadrant photodiode. A feedback loop maintains a constant tip-sample force. This can be done by operating in contact mode, where a constant cantilever deflection is maintained, or in

intermittent contact mode where the cantilever is oscillated near resonance and constant amplitude is maintained. The AFM is also capable of force spectroscopy measurements.

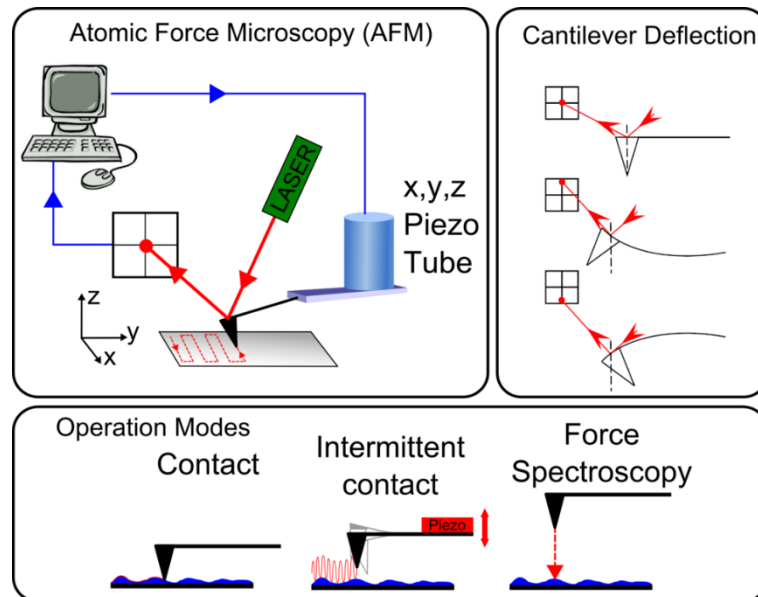


**Fig. 2- 3** Schematic diagram of AFM analysis

The surface roughness of the films were observed and analyzed by a SPM-9500J3 atomic force microscopy (AFM), as shown in Figure 2-3. The Atomic Force Microscope uses a force-sensitive probe to detect the interaction between the tip and the sample to achieve surface imaging. The tapping mode was used during the test [9, 10]. The micro-rotor was forced to vibrate near its resonant frequency, and the oscillating tip gently tapped the surface, intermittently contacting the sample. Since the interaction between the tip and the sample is small, the resolution caused by the shear force and the damage to the sample almost disappear. The micromorphology and cross-section of the films were observed and analyzed by scanning electron microscope (SEM; HITACHI, TM3000). The scanning electron microscope can directly observe the surface quality of the film, such as uniformity and flatness. The cross-section used for SEM was milled by focused

ion beam (FIB) with a JIB-4500 Multi Beam system.

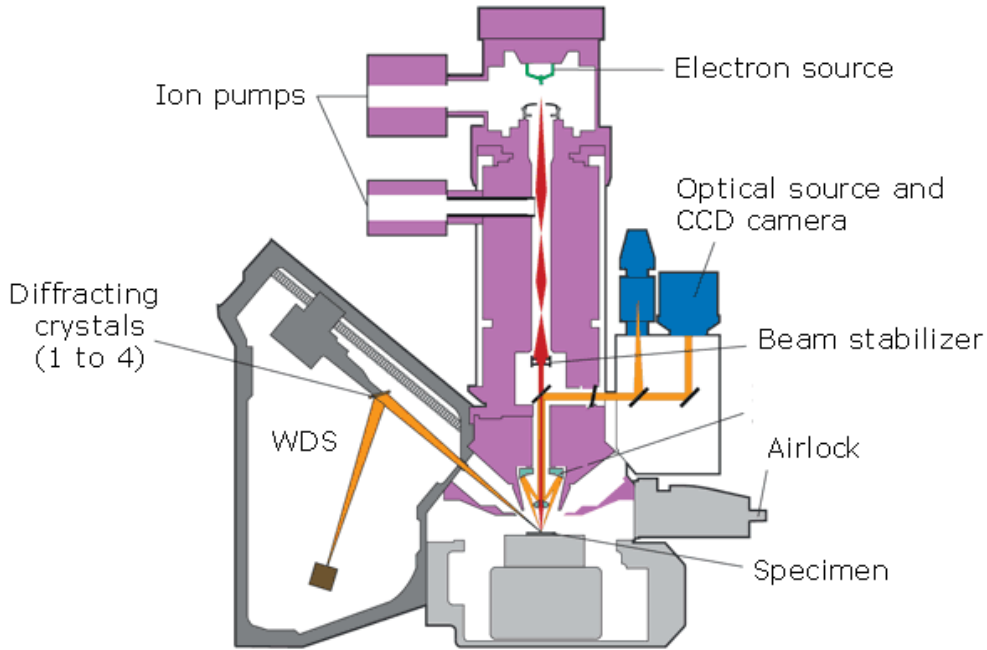


**Fig. 2- 4** Schematic diagram of EPMA

The element compositions of cross-section polished with diamond paste ( $0.05\ \mu\text{m}$ ) were determined by an Electron probe microanalysis (EPMA) JXA-8900R. EPMA works by bombarding a micro-volume of a sample with a focused electron beam (typical energy = 5-30 keV) and collecting the X-ray photons thereby emitted by the various elemental species.

- EPMA is a fully qualitative and quantitative method of non-destructive elemental analysis of micron-sized volumes at the surface of materials, with sensitivity at the level of ppm. Routine quantification to 1% reproducibility is obtained over several days. It is the most precise and accurate micro-analysis technique available and all elements from B to U and above can be analyzed.
- EPMA is fully compatible with routine analysis sessions, with easy and direct interpretation of the results.

- Determination of thickness and elemental composition from nm to mm thick layers in stratified materials is possible.

EPMA provides much better results than standard SEM/EDS systems. Because of the internal properties of WDS, the general sensitivity, analysis of light elements and risks of erroneous interpretation of qualitative spectra are all superior with EPMA. Spectral resolution and detector dead time are much better than EDS (Energy Dispersive Spectroscopy). The excitation beam regulation system and sophisticated sample stage capabilities guarantee that this technique provides outstanding stability and measurement repeatability.

The carbon element concentration distribution of DLC film-coated SUS316L were determined by EPMA. The sample to be analyzed was bombarded by an electron beam which would emit x-rays with wavelengths characteristic to specific elements. Then the concentration distribution and diffusivities of elements could be obtained accurately by EPMA mapping [11, 12].

### 2.2.3 XPS analysis

X-ray Photoelectron Spectroscopy (XPS) also known as Electron Spectroscopy for Chemical Analysis (ESCA) is the most widely used surface analysis technique because it can be applied to a broad range of materials and provides valuable quantitative and chemical state information from the surface of the material being studied[13-15]. The average depth of analysis for an XPS measurement is approximately 5 nm. PHI XPS instruments provide the ability to obtain spectra with a lateral spatial resolution as small as 7.5  $\mu\text{m}$ . Spatial distribution information can be obtained by scanning the micro focused x-ray beam across the sample surface. Depth distribution information can be obtained by

combining XPS measurements with ion milling (sputtering) to characterize thin film structures. The information XPS provides about surface layers or thin film structures is important for many industrial and research applications where surface or thin film composition plays a critical role in performance including: nanomaterials, photovoltaics, catalysis, corrosion, adhesion, electronic devices and packaging, magnetic media, display technology, surface treatments, and thin film coatings used for numerous applications.

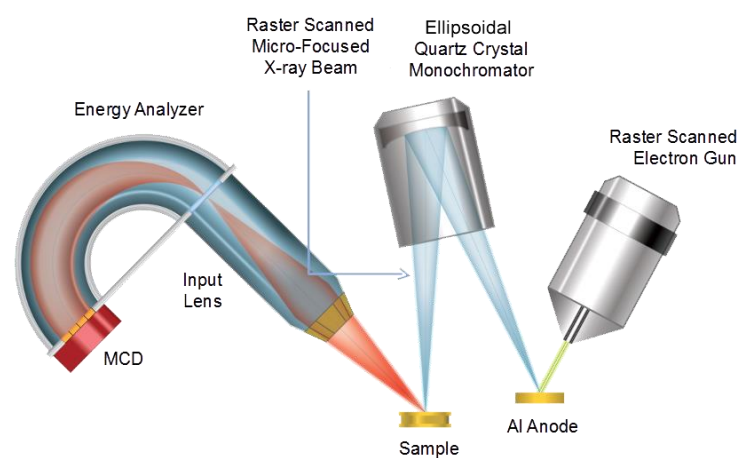


**Fig. 2- 5** Schematic diagram of XPS analysis

XPS is typically accomplished by exciting a samples surface with mono-energetic Al  $\alpha$  x-rays causing photoelectrons to be emitted from the sample surface. An electron energy analyzer is used to measure the energy of the emitted photoelectrons. From the binding energy and intensity of a photoelectron peak, the elemental identity, chemical state, and quantity of a detected element can be determined. Schematic presentation of XPS spectroscopy instrument is shown in figure 2-4.

Physical Electronics XPS instruments function in a manner analogous to SEM/EDS instruments that use a finely focused electron beam to create SEM images for sample viewing and point spectra or images for compositional analysis. With the PHI XPS

instruments, a finely focused x-ray beam is scanned to create secondary electron images for sample viewing and point spectra or images for compositional analysis. The size of the x-ray beam can be increased to support the efficient analysis of larger samples with homogeneous composition. In contrast to SEM/EDS which has a typical analysis depth of 1-3  $\mu\text{m}$ , XPS is a surface analysis technique with a typical analysis depth of less than 5 nm and is therefore better suited for the compositional analysis of ultra-thin layers and thin microscale sample features.

X-ray photoelectron spectroscopy (XPS) is a surface analysis technique for studying the composition of surface elements and the state of ions. The basic principle is to irradiate the material with X-ray, so that the inner electrons or valence electrons of the material atoms and molecules can be excited to absorb light energy and get away from the surface of the object. The composition of the object to be tested can be understood by analyzing the photoelectron energy. The main application of XPS is to achieve a defined and quantitative analysis of surface elements by measuring the binding energy of electrons. XPS analysis can also infer the structure of a compound or the binding state of an element (ion) to other surrounding ions theoretically. The advantage of the XPS method is that it can reflect the content of various bonds. The disadvantage is that the disorder in the film interferes with the measurement accuracy, so the full spectrum needs to be analyzed to separate the true spectrum. In this work, the equipment Physical Electronics (PHI) Quantum 2000 was used to characterize the composition and chemical bonds of the solid surface. The Quantum 2000 is a high performance Scanning ESCA Microprobe with a minimum x-ray beam size of less than 10 $\mu\text{m}$  and uses an Al  $K\alpha$  X-ray source with an energy of 1486.68 eV. The accelerating voltage and emission current of the X-ray source were kept at 13 kV and 12 mA, respectively.

#### 2.2.4 TEM analysis

Transmission electron microscopy (TEM) is an imaging technique where a beam of electrons is transmitted through a specimen, thereby casting an image is formed, magnified and directed to appear either on a fluorescent screen or layer of photographic film or to be detected by a sensor such as a CCD camera. The first practical transmission electron microscope was built by Albert Prebus and James Hillier at the university of Toronto in 1938 using concepts developed earlier by Max Knoll and Ernst Ruska. The most common use of transmission electron microscopy in nanomaterials is to measure the distribution of particle size as well as the morphology of supported or unsupported active materials. It is also used to detect the defect structures in case of some electronic materials. The specimens for TEM should be very thin so that the electron beam may penetrate through the sample and should be able to withstand the high vacuum present inside the instrument. Fig. 2-6 shows the schematic of the working of a transmission electron microscope [16]. The FIB equipment we used for preparing TEM samples. As an initial work of specimen preparation, the sample was cut into a size of 10mm×10mm. After thinning the slice thickness to about 30μm, a 1.5mm×1.5mm foil was cut off and glued on a Mo grid. Then the sample was further cut by FIB. The sample was milled into stair-step shape initially and finally it was milled down to a thickness of about 0.1 μm.

In the TEM results, Diffraction contrast is formed by elastically scattered electrons (Incident electrons) that are scattered (deflected from their original path) by atoms in the specimen in an elastic fashion (no loss of energy). Samples can exhibit diffraction contrast, whereby the electron beam undergoes Bragg's scattering which in the case of a crystalline sample, disperses electrons into discrete locations in the back focal plane. Electrons passing through at a similar angle are scattered, these electrons can then be collated using

magnetic lenses to form a pattern of spots; each spot corresponds to a specific atomic spacing (a plane). This pattern can then yield information about the orientation, atomic arrangements and phases present in the area being examined [17, 18]. From the selected area diffraction pattern, d-spaces corresponding to the rings could be calculated by the following equation:

$$Rd=L\lambda \quad (2-1)$$

where R is the distance of any reflections from the center of pattern, d is the interplanar spacing, L is the effective camera length,  $\lambda$  is the wave length of the incident beam.

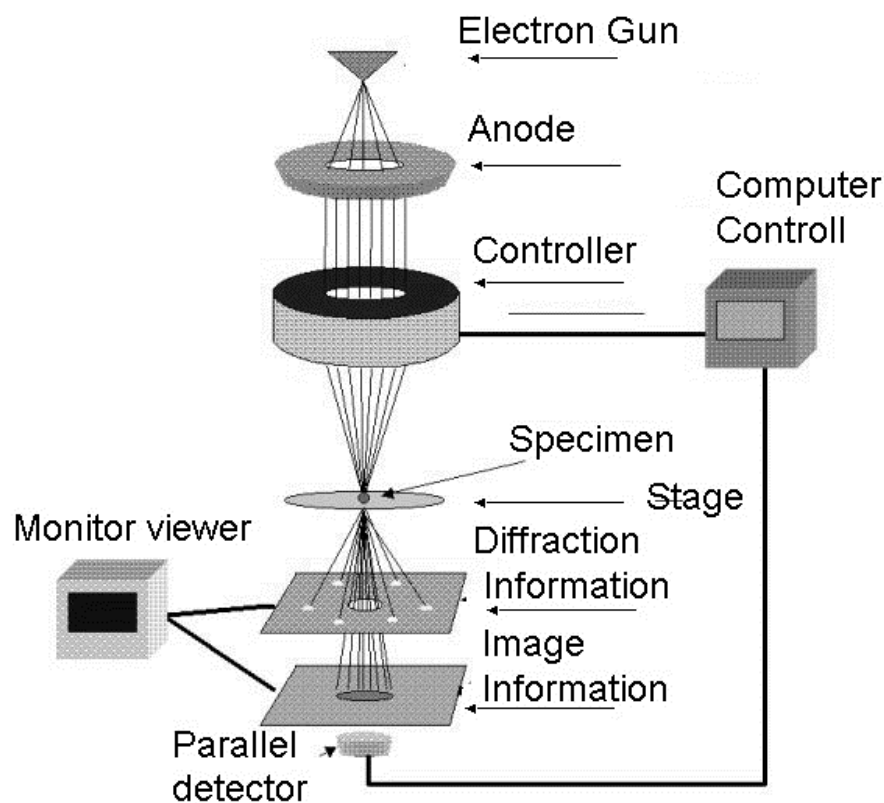


**Fig. 2- 5** Schematic diagram of TEM analysis

### 2.3 Analysis of hardness and tribological behavior

In the nanoindentation test [19, 20], the indenter is pushed into the surface of the sample producing both elastic and plastic deformation of the material (Fig. 2-7). The first difference with macro- or micro-indentation tests is that, in the nanoindentation machines, the displacement  $h$  and the load  $L$  are continuously monitored with high precision, as schematically shown in Fig. 2-8. During the nanoindentation process, the indenter will penetrate the sample until a predetermined maximum load  $L_{\max}$  is reached, where the corresponding penetration depth is  $h_{\max}$ . When the indenter is withdrawn from the sample, the unloading displacement is also continuously monitored until the zero load is reached and a final or residual penetration depth  $h_f$  is measured. The slope of the upper portion of the unloading curve, denoted as  $S = dL/dh$ , is called the elastic contact stiffness [21, 22]. In nanoindentation, the hardness of the material is defined as  $H = L/A_{pml}$ , where  $A_{pml}$  is the projected area of contact at the maximum load. In this method, the maximum load ranges between few  $1 \mu\text{N}$  and about  $200 \text{ mN}$ , while penetrations will vary from few  $\text{nm}$  to about few  $\mu\text{m}$  [22, 23].

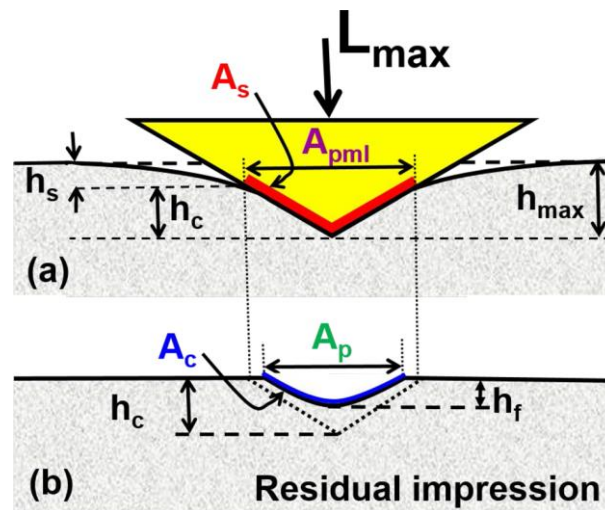


**Fig. 2- 6** A Elasto-plastic deformation at the maximum applied load  $L_{\max}$ ; b plastic deformation after releasing the load

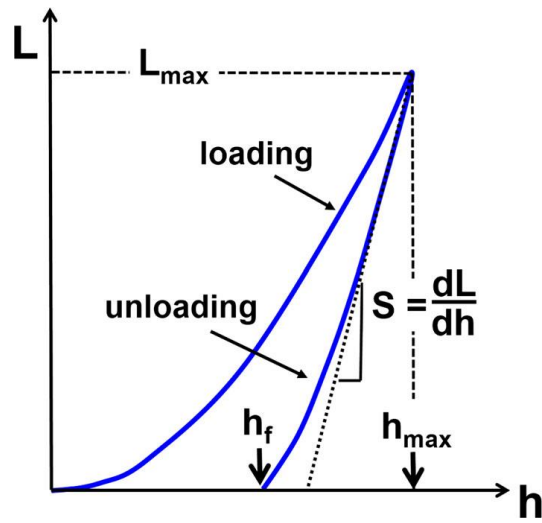
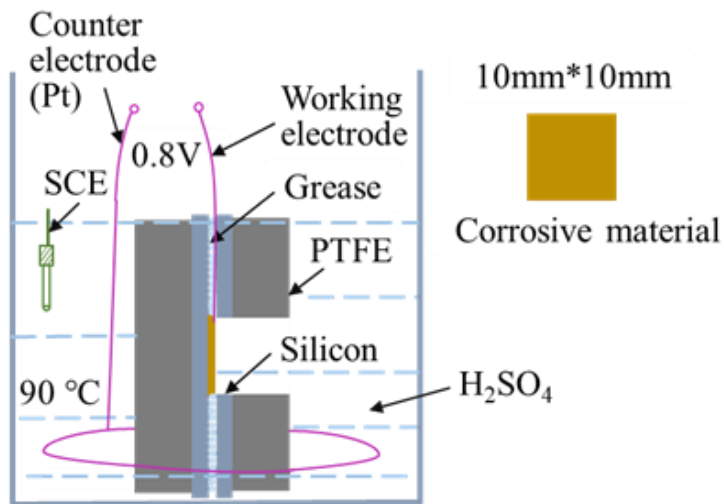


Fig. 2- 7 Load–unload during nanoindentation

## 2.4 Corrosion performance analysis

### 2.4.1 Corrosion test

The DLC films-coated stainless steel and titanium substrates were corroded by potentiostatic polarizations in a 0.5mol/L sulfuric acid solution at 90 °C, 0.8V for 168 hrs. The schematic diagram of corrosion test was showed in Fig. 2-9. The sample was cut to a size of 20 × 20 mm<sup>2</sup> by a circular saw after the deposition and then sealed with epoxy resin and exposed one end with an area of 10 × 10 mm<sup>2</sup>. The metal ions in sulfuric acid corrosion solution were detected by inductively coupled plasma (ICP) atomic emission spectroscopy after corrosion experiment. The Schematic diagram of ICP was shown in Fig. 2-10.



**Fig. 2- 8** Schematic diagram of corrosion test

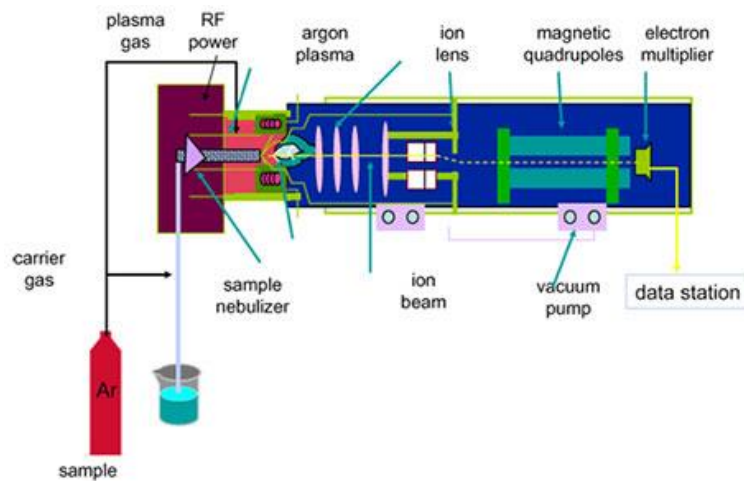


**Fig. 2- 9** Schematic diagram of ICP analysis

Inductively coupled plasma atomic emission spectroscopy (ICP-AES), also referred to as inductively coupled plasma optical emission spectrometry (ICP-OES), is an analytical technique used for the detection of chemical elements [24]. It is a type of emission spectroscopy that uses the inductively coupled plasma to produce excited atoms and ions that emit electromagnetic radiation at wavelengths characteristic of a particular element.

It is a flame technique with a flame temperature in a range from 6000 to 10000 K. The intensity of this emission is indicative of the concentration of the element within the sample. The ICP-AES is composed of two parts: the ICP and the optical spectrometer. The ICP torch consists of 3 concentric quartz glass tubes. The output or "work" coil of the radio frequency (RF) generator surrounds part of this quartz torch. Argon gas is typically used to create the plasma. Examples of the application of ICP-AES include the determination of metals in wine, arsenic in food, and trace elements bound to proteins.

#### 2.4.2 Corrosion behavior DLC films

Pitting Corrosion is the localized corrosion of a metal surface confined to a point or small area, which takes the form of cavities. Pitting corrosion is one of the most damaging forms of corrosion. Pitting factor is the ratio of the depth of the deepest pit resulting from corrosion divided by the average penetration as calculated from weight loss. The driving power for pitting corrosion is the depassivation of a small area, which becomes anodic while an unknown but potentially vast area becomes cathodic, leading to very localised galvanic corrosion. The corrosion penetrates the mass of the metal, with a limited diffusion of ions. The more conventional explanation for pitting corrosion is that it is an autocatalytic process. Metal oxidation results in localised acidity that is maintained by the spatial separation of the cathodic and anodic half-reactions, which creates a potential gradient and electromigration of aggressive anions into the pit. Fig. 2-11 shows a mechanism of localised corrosion developing on metal in a solution containing oxygen.

In the process,  $\text{Fe} + 2\text{H}^+ \rightarrow \text{Fe}^{2+} + 2\text{e}^-$ .

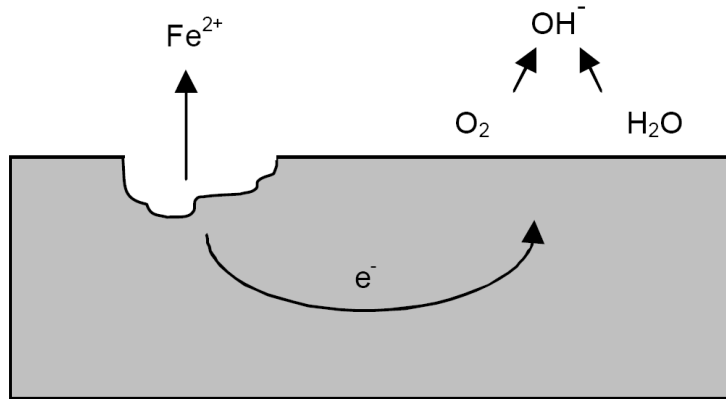


**Fig. 2- 11** Mechanism of localized corrosion developing on metal in a solution containing oxygen

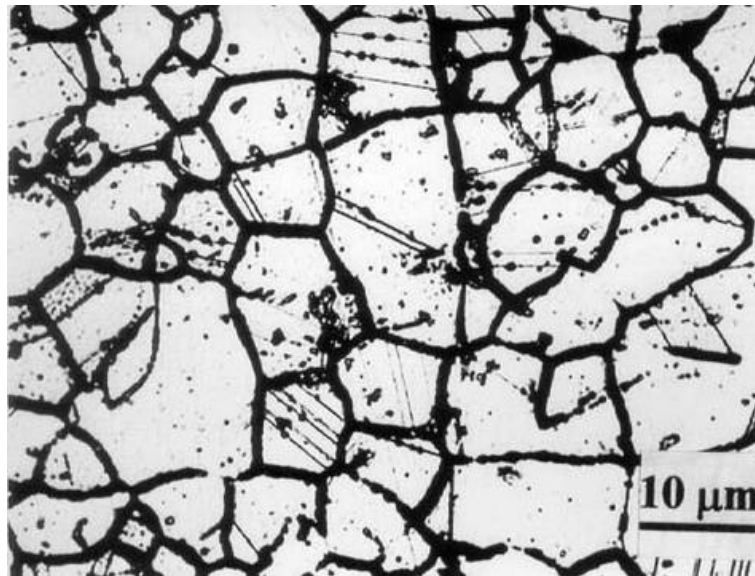


**Fig. 2- 12** Heavily sensitized microstructure

Intergranular corrosion (IGC), also known as intergranular attack (IGA), is a form of corrosion where the boundaries of crystallites of the material are more susceptible to corrosion than their insides [25, 26]. Sensitization refers to the precipitation of carbides at grain boundaries in a stainless steel or alloy, causing the steel or alloy to be susceptible to intergranular corrosion or intergranular stress corrosion cracking. Certain alloys when exposed to a temperature characterized as a sensitizing temperature become particularly susceptible to intergranular corrosion. In a corrosive atmosphere, the grain interfaces of

these sensitized alloys become very reactive and intergranular corrosion results. This is characterized by a localized attack at and adjacent to grain boundaries with relatively little corrosion of the grains themselves. The alloy disintegrates (grains fall out) and/or loses its strength. The Fig. 2-12 shows the typical microstructure of a heavily sensitized steel. The samples have been polished and etched before taking the photos, and the sensitized areas show as wide, dark lines where the etching fluid has caused corrosion. The dark lines consist of carbides and corrosion products.

## References

- [1] A. H. Deutchman and R. J. Partyka, "Ion beam enhanced deposition," *Advanced materials & processes*, vol. 161, no. 7, pp. 33-35, 2003.
- [2] A. H. Deutchman and R. J. Partyka, "Industrial Scale Ion Beam Enhanced Deposition (IBED) Processing System," in *Proceedings: ASM International Surface Engineering Congress*, 2002, pp. 1-9.
- [3] P. Sioshansi and E. J. Tobin, "Surface treatment of biomaterials by ion beam processes," *Surface and coatings Technology*, vol. 83, no. 1-3, pp. 175-182, 1996.
- [4] J. Robertson, "Diamond-like amorphous carbon," *Materials science and engineering: R: Reports*, vol. 37, no. 4-6, pp. 129-281, 2002.
- [5] D. A. Long and D. Long, *Raman spectroscopy*. McGraw-Hill New York, 1977.
- [6] A. C. Ferrari, "Raman spectroscopy of graphene and graphite: disorder, electron-phonon coupling, doping and nonadiabatic effects," *Solid state communications*, vol. 143, no. 1-2, pp. 47-57, 2007.
- [7] D. S. Knight and W. B. White, "Characterization of diamond films by Raman spectroscopy," *Journal of Materials Research*, vol. 4, no. 2, pp. 385-393, 1989.
- [8] H.-J. Butt, B. Cappella, and M. Kappl, "Force measurements with the atomic force microscope: Technique, interpretation and applications," *Surface science reports*, vol. 59, no. 1-6, pp. 1-152, 2005.
- [9] M. Tortorese, R. Barrett, and C. Quate, "Atomic resolution with an atomic force microscope using piezoresistive detection," *Applied physics letters*, vol. 62, no. 8, pp. 834-836, 1993.
- [10] S. Alexander *et al.*, "An atomic-resolution atomic-force microscope implemented using an optical lever," *Journal of Applied Physics*, vol. 65, no. 1, pp. 164-167, 1989.
- [11] J. H. Kim, J. T. Yeom, J. K. Hong, S. Y. Shim, S. G. Lim, and N. K. Park, "Effect of scandium on the hot extrudability of 7075 aluminum alloy," *Metals and Materials International*, vol. 16, no. 4, pp. 669-677, 2010.
- [12] W. Lengauer and M. Bohn, "Thermochemical basis of the preparation of well-defined transition metal carbide, nitride and carbonitride reference materials for electron-probe microanalysis (epma)," in *Solid State Phenomena*, 2018, vol. 274, pp. 20-42: Trans Tech Publ.
- [13] F. A. Delesma, M. Van den Bossche, H. Grönbeck, P. Calaminici, A. M. Köster, and L. G. Pettersson, "A Chemical View on X-ray Photoelectron Spectroscopy:

- the ESCA Molecule and Surface-to-Bulk XPS Shifts," *ChemPhysChem*, vol. 19, no. 2, pp. 169-174, 2018.
- [14] J. Moulder, "The impact of the scanning XPS microprobe on industrial applications of X-ray photoelectron spectroscopy," *Journal of Electron Spectroscopy and Related Phenomena*, 2018.
- [15] M. Schmal and C. A. C. Perez, "X-Ray Photoelectron Spectroscopy (ESCA: XPS/ISS)," in *Heterogeneous Catalysis and its Industrial Applications*: Springer, 2016, pp. 251-266.
- [16] B. Baruwati, "Studies on the Synthesis, Characterization, Surface Modification and Application of Nanocrystalline Nickel Ferrite," INDIAN INSTITUTE OF CHEMICAL TECHNOLOGY HYDERABAD, 2007.
- [17] P. Stadelmann, "Image analysis and simulation software in transmission electron microscopy," *Microscopy and microanalysis*, vol. 9, no. S03, pp. 60-61, 2003.
- [18] N. Tanaka, *Scanning transmission electron microscopy of nanomaterials*. World Scientific, 2015.
- [19] E. Broitman, "Indentation hardness measurements at macro-, micro-, and nanoscale: a critical overview," *Tribology Letters*, vol. 65, no. 1, p. 23, 2017.
- [20] K. Liu, M. Ostadhassan, and B. Bubach, "Applications of nano-indentation methods to estimate nanoscale mechanical properties of shale reservoir rocks," *Journal of Natural Gas Science and Engineering*, vol. 35, pp. 1310-1319, 2016.
- [21] E. Berkovich, "Three faceted diamond pyramid for micro-hardness testing," *Industrial Diamond Review*, vol. 11, no. 127, p. 129, 1951.
- [22] W. C. Oliver and G. M. Pharr, "An improved technique for determining hardness and elastic modulus using load and displacement sensing indentation experiments," *Journal of materials research*, vol. 7, no. 6, pp. 1564-1583, 1992.
- [23] W. C. Oliver and G. M. Pharr, "Measurement of hardness and elastic modulus by instrumented indentation: Advances in understanding and refinements to methodology," *Journal of materials research*, vol. 19, no. 1, pp. 3-20, 2004.
- [24] S. Greenfield, "Inductively coupled plasma-atomic emission spectroscopy (ICP-AES) with flow injection analysis (FIA)," *Spectrochimica Acta Part B: Atomic Spectroscopy*, vol. 38, no. 1-2, pp. 93-105, 1983.
- [25] H. Kokawa, M. Shimada, M. Michiuchi, Z. Wang, and Y. Sato, "Arrest of weld-decay in 304 austenitic stainless steel by twin-induced grain boundary engineering," *Acta Materialia*, vol. 55, no. 16, pp. 5401-5407, 2007.
- [26] C. Hu *et al.*, "Improving the intergranular corrosion resistance of 304 stainless steel by grain boundary network control," *Corrosion science*, vol. 53, no. 5, pp.

1880-1886, 2011.

# Chapter 3 Surface characteristics and tribological properties of DLC films on magnesium alloy

## 3.1 Chemical bonding structure of DLC films

Raman spectroscopy is generally used to analyze the detailed bonding structure of DLC coatings. Raman spectroscopy has the advantages of being non-destructive and allowing easy examination of the low-wavenumber region.

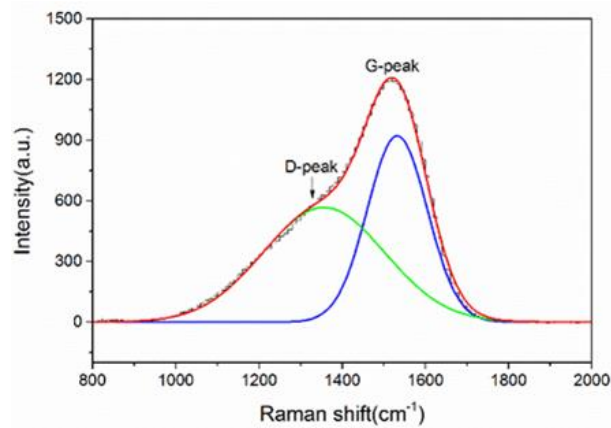


**Fig. 3- 1** The typical Raman spectrum fitted by the Gaussian at 6 sccm and 6 kV.

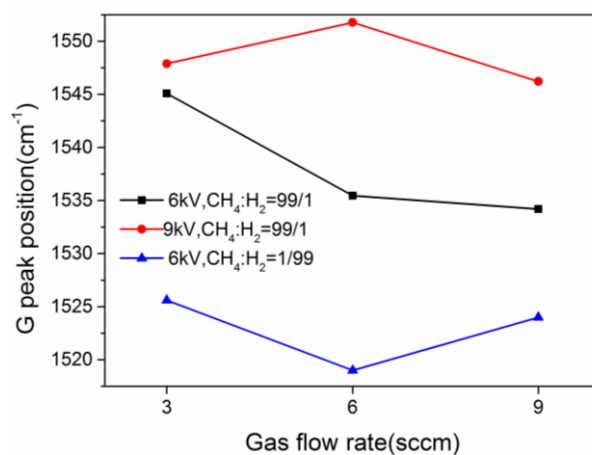


**Fig. 3- 2** The G-peak position of DLC coatings deposited at different gas ratio, flow rate and accelerating voltage.

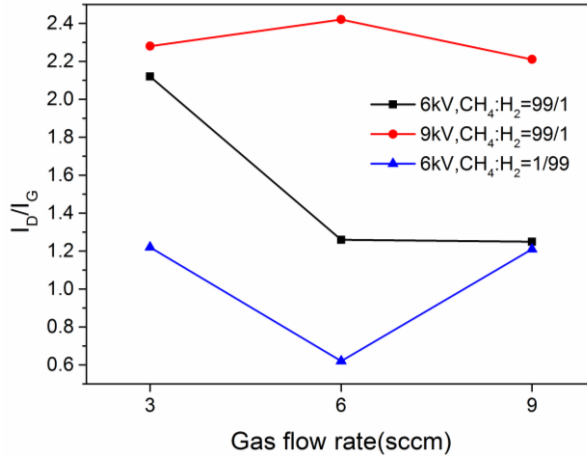


**Fig. 3-3** The  $I_D/I_G$  of DLC films deposited at different gas ratio, flow rate and accelerating voltage.

In general, the Raman spectra of the DLC films could be fitted by two Gaussian peaks: the G-peak (located at approximately  $1580\text{ cm}^{-1}$ ) and D-peak (located at approximately  $1350\text{ cm}^{-1}$ ). The G-peak (graphite) originates from bond stretching of  $sp^2$  atoms in both aromatic rings and chains, and the D-peak (disorder) originates from the breathing modes of  $sp^2$  atoms in aromatic rings [1, 2]. The  $sp^2$  site consists of two  $\pi$  orbitals and two  $\sigma$  orbitals, whereas the  $sp^3$  site consists of four  $\sigma$  orbitals. The  $\pi$  state is more polarizable than the  $\sigma$  state because of the lower energy of the  $\pi$  state. Therefore, the Raman spectra are dominated by the  $sp^2$  site, which has a 50–230 times larger Raman cross-section than the  $sp^3$  site [3]. Fig. 3-1 displays a typical Raman spectrum for the DLC coating deposited at 6 sccm/ 6 kV. The spectrum consists of a widely asymmetric Raman scattering band in the range of  $1000\text{--}2000\text{ cm}^{-1}$ , which is a typical characteristics of DLC coatings [4].

The intensity ratio of the D-peak to G-peak ( $I_D/I_G$ ) and the position of the G-peak were used to characterize the DLC films [5, 6]. A shift of the G-peak position to higher wavenumbers and an increase of the intensity ratio  $I_D/I_G$  are consistent with an increase in the  $sp^2/sp^3$  ratio [7]. Fig. 3-2 displays the G-peak position of DLC coatings deposited

at different gas ratio, flow rate and accelerating voltages. Using of the Gaussian fitting method, the  $I_D/I_G$  ratios of the DLC films with different processing conditions were presented in Fig. 3-3. The  $I_D/I_G$  ratios increased and the G-peak position shifted toward higher wavenumber with increasing accelerating voltage at  $CH_4/H_2$  ratio of 99:1, and  $I_D/I_G$  decreased and the G-peak position shifted toward lower wavenumber with increasing gas flow rate at 6 kV.  $I_D/I_G$  decreased and the G-peak position shifted toward lower wavenumber when the gas flow rate increased from 3 sccm to 6 sccm at  $CH_4/H_2$  ratio of 1:99. The  $I_D/I_G$  and G-peak position were lower for the deposition at  $CH_4/H_2=99:1$  than at  $CH_4/H_2=1:99$ . For instance, at  $CH_4/H_2$  ratio of 99:1, a gas flow rate of 9 sccm and accelerating voltages of 6 and 9 kV, the G-peak position was 1534.2 and 1546.2  $cm^{-1}$  as shown in Figure 3. The corresponding  $I_D/I_G$  ratios were 1.25 and 2.21 respectively shown on Figure 4. For the accelerating voltage of 6 kV and gas flow rates of 3 and 9 sccm, the  $I_D/I_G$  ratios were 2.12 and 1.25, respectively. Thus, the  $I_D/I_G$  ratio of the DLC film deposited at 6 kV was lower than that deposited at 9 kV. The  $I_D/I_G$  ratio decreased with decreasing  $CH_4/H_2$  ratio from 99:1 to 1:99, The  $I_D/I_G$  ratio decreased to a minimum value of 0.62 at 6 sccm/6 kV.

Usually, an increase in the G-peak position correspond to an increase in the  $sp^3$  content. The  $I_D/I_G$  values are related to  $sp^2$  clustering and increase as the  $sp^2$  fraction increases [5]. The G-peak position and  $I_D/I_G$  ratio increase with increasing  $sp^2/sp^3$  ratio in hydrogenated amorphous DLC films [8]. If the  $sp^2$  type is predominant, the film will be softer and the DLC film structure will be more disordered. The nanostructure is transformed from a typical three-dimensional diamond-like crosslinking structure to a two-dimensional graphite-like structure. As the fraction of  $sp^3$ -hybridized C–C bonding increases, the films become harder.

In this study, a lower acceleration voltage led to higher hardness, which suggests more  $sp^3$ -hybridized C-C bonding. When a DLC coating is deposited at too high of an accelerating voltage, the ions may have too much energy. The ions with higher energy cause the  $sp^3$  bonds to break down into stable  $sp^2$  bonds with low-energy states. In addition, thermal effects at very high accelerating voltage and ion energies cause annealing effects. The generation of thermal energy leads to relaxation and the formation of more stable graphite-like  $sp^2$  bonds. As the accelerating voltage decreases, the thermal annealing is reduced and the  $sp^3$ -hybridized C-C bonding becomes permanent. The high gas flow rate leads to more collisions of ions and species. As a result, the final energy of the film-forming ions is lower, which apparently results in a higher amount of  $sp^3$  C-C bonding. In addition, the surface becomes smoother because of the increased surface mobility of the species. The high gas flow rate leads to a high amount of  $sp^3$  C-C bonding and low  $I_D/I_G$  in the DLC films. There are possible of other effects, such as the  $CH_x$  group ions reacting with dangling C-bonds, orbital hybridization between carbon atoms, and the formation of  $sp^3$  C-C bonds at the surface of the magnesium alloy. Therefore, the DLC films deposited at 6 kV exhibited higher hardness than those deposited at 9 kV. The  $I_D/I_G$  ratio is lower for the deposition at  $CH_4/H_2=1:99$  than at  $CH_4/H_2=99:1$  because of the increase in hydrogen atoms promoting the formation of  $sp^3$  C-C bonding. The gas flow rate and acceleration voltage play key roles in determining the chemical bond structure. It is known that a low gas flow rate enhances dissociation of  $CH_4$  because of the resident time at the plasma and leads to graphitization of the film structure because of H ion/atom/molecule enrichment [9].

### 3.2 Hardness analysis of DLC films

The surface hardness of the DLC films was evaluated using nano-indenter (JSPM-4210). The nano-indenter is especially suitable for measuring the hardness of micro-volume materials such as thin films, clad layer and materials in MEMS [10]. Table 3-1 and 3-2 display the hardness of the DLC coatings deposited at different gas ratio, flow rates and accelerating voltages. The surface hardness clearly increased with increasing gas flow rate at 6 kV. The hardness of the DLC coating was higher for the deposition at 6 kV than at 9 kV. For an accelerating voltage of 6 kV at CH<sub>4</sub>/H<sub>2</sub>=1:99, the hardness changed abruptly as the gas flow rate increased from 3 to 9 sccm. The hardness increased to a maximum of 4056HV at 6 sccm/6 kV. Generally, the internal stress and surface hardness of the DLC coating is related to the  $sp^2/sp^3$  ratio and amount of H<sub>2</sub>. The hydrogen content is considered to play an important role in determining the bonding structure of C atoms by helping to stabilize the  $sp^3$ -C structure [11]. A low  $sp^2/sp^3$  ratio implies low internal stress and high hardness. Therefore, the hardness results are consistent with the I<sub>D</sub>/I<sub>G</sub> results presented in Fig. 3-3. The decreasing I<sub>D</sub>/I<sub>G</sub> of the DLC coatings deposited at low accelerating voltage correlates with an increase in the hardness. At the CH<sub>4</sub>/H<sub>2</sub> ratio of 1:99, the DLC coatings exhibited higher hardness than that of 99:1. Because of the presence of hydrogen atoms, the local structure of the film is made porous, suppressing the  $sp^2$ -C structure with shorter C-C bond length (~1.42Å), and increasing the  $sp^3$ -C structure with longer C-C bond length (~1.54Å). As the gas flow rate increases, the  $sp^3/sp^2$  ratio and film density increase and reach a saturation value [12]. The DLC coatings deposited at 6 sccm/6 kV appeared to contain a more diamond-like nanostructure. The Vickers hardness of AZ31 magnesium alloy is only 78HV. The hardness of all the AZ31-coated DLC coatings were much higher than that of the uncoated substrate, indicating that the hardness characteristics of magnesium alloy AZ31 were greatly improved by the

DLC coatings.

**Table 3- 1** Hardness of DLC coatings deposited at 6 kV

	CH <sub>4</sub> /H <sub>2</sub> = 99:1			CH <sub>4</sub> /H <sub>2</sub> = 1:99		
Accelerating Voltage (kV)	6			6		
Gas flow rate (sccm)	3	6	9	3	6	9
Hardness (HV)	1011	1036	1044	1320	4056	1334

**Table 3- 2** Hardness of DLC coatings deposited at 9 kV

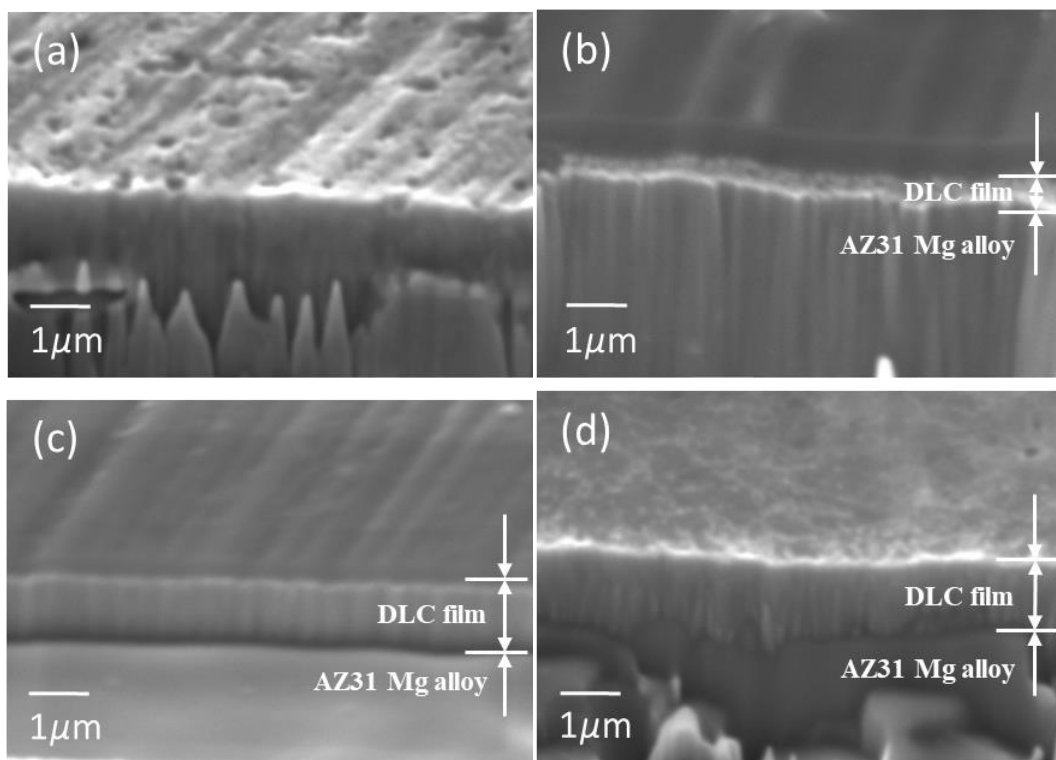
	CH <sub>4</sub> /H <sub>2</sub> = 99:1		
Accelerating Voltage (kV)	9		
Gas flow rate (sccm)	3	6	9
Hardness (HV)	1006	806	1018

### 3.3 Cross-section morphology and thickness analysis of DLC films

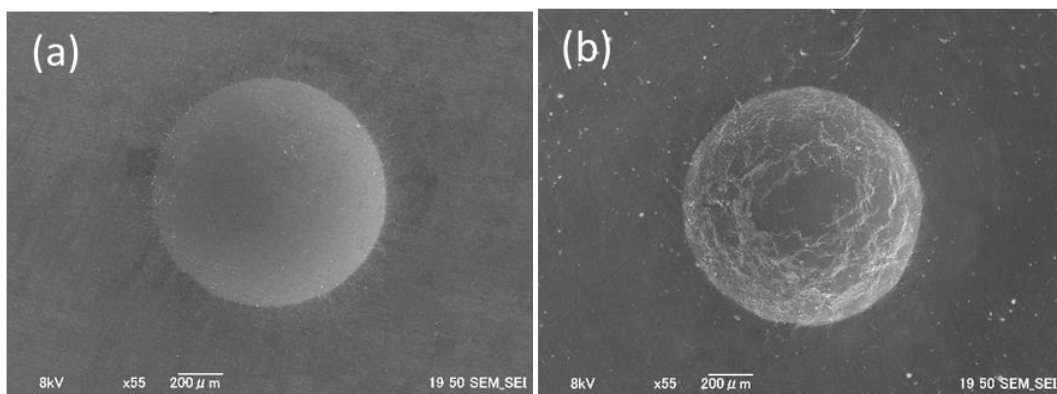
SEM images showing the cross-sectional morphology of the (a) AZ31 magnesium alloy and DLC films deposited at the CH<sub>4</sub>/H<sub>2</sub> ratio of 1:99 and at (b) 3 sccm/6 kV, (c) 6 sccm/6 kV, and (d) 9 sccm/6 kV are presented in Figure 3-4. Compared with the surface of the uncoated AZ31 magnesium alloy, no obvious cracks or delamination were observed for any of the DLC coating surfaces, indicating that the DLC films were successfully deposited on the substrates as protective coatings. The DLC film surfaces were uniform over a large area. The surface of the magnesium alloy substrate consisted of an oxide film

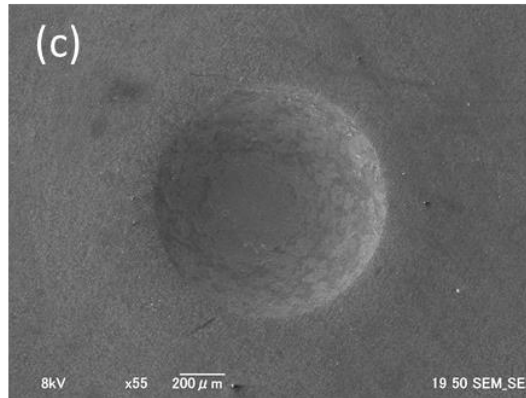
because of the exposure to air, as observed in Figure 3-4(a). The oxidized layer was removed before deposition of the DLC film. The average thickness of the DLC film was approximately 0.284 and 1.145  $\mu\text{m}$ , respectively, at 3sccm/6 kV and 9sccm/6 kV shown on Figure 3-4(a) and (d). The thickness of the DLC layer was approximately 1.034  $\mu\text{m}$  at 6 sccm/6 kV shown on Figure 3-4(c). No delamination was observed between the DLC coatings and magnesium alloy, indicating good adhesion. The DLC coating deposited at 6 sccm/6 kV was denser than that of others.

The adhesion of thin films can be evaluated using Rockwell hardness tests using a quantifiable method. Adhesion criteria was developed by the Union of German Engineers (Verein Deutscher Ingenieure, VDI). A load of 150kg was applied to cause film damage at the perimeter of the indentation in this paper. Figure 3-5 shows Rockwell indentation craters for DLC coatings deposited (a) at 3 sccm/6 kV; (b) at 9 sccm/6 kV; (c) at 3 sccm/9 kV. The SEM image illustrated that there were little radial cracks and little flaking areas near the boundary of indentation craters shown on Figure 3-5(b). Compared to typical classification map of adhesion strength quality (HF1-HF6) [13, 14], DLC films deposited at 9 sccm/6 kV represent HF2 type which indicating the acceptable adhesion between DLC film and magnesium alloy. This may indicate that the harder DLC film is easier to crack and scale when mechanical strain was applied because of tensile residual stresses. The little cracks were found on DLC film deposited at 3 sccm/6 kV near the boundary of indentation craters. It may be due to the low film thickness. The adhesion strength is related to HF1-HF2 which indicating the good interfacial adhesion. The DLC film had the least cracks deposited at 3 sccm/9 kV indicating the best adhesion strength quality shown on Figure 3-5(c).



**Fig. 3- 4** Cross-section SEM images at a tilted angle of 38° from the vertical position of the electron beam to the sample cross-section. (a) AZ31 magnesium alloy substrate, DLC films deposited at the CH<sub>4</sub>/H<sub>2</sub> ratio of 1:99 and at (b) 3 sccm/6 kV; (c) 6 sccm/6 kV; (d) 9 sccm/6 kV.

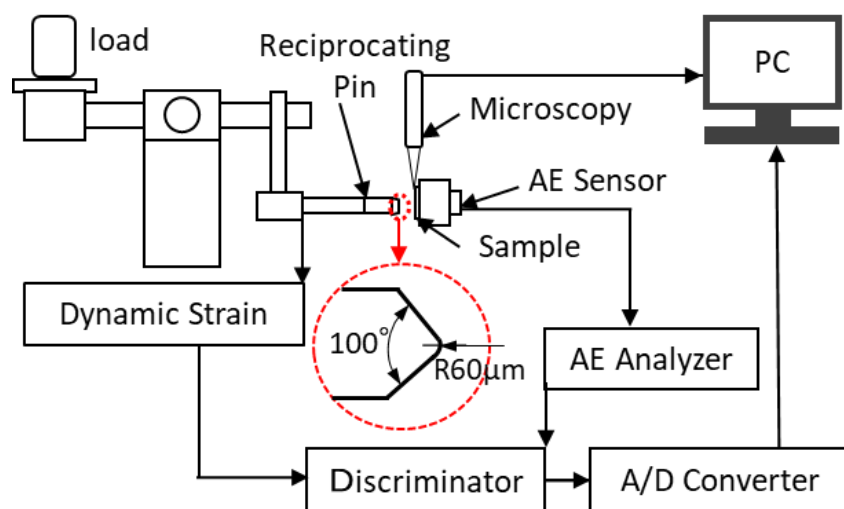




**Fig. 3- 5** Rockwell indentation craters for DLC coatings deposited at the  $\text{CH}_4/\text{H}_2$  ratio of 1:99 and at (a) 3 sccm/6 kV; (b) 9 sccm/6 kV; (c) 3 sccm/9 kV.

### 3.4 Tribological properties of DLC films

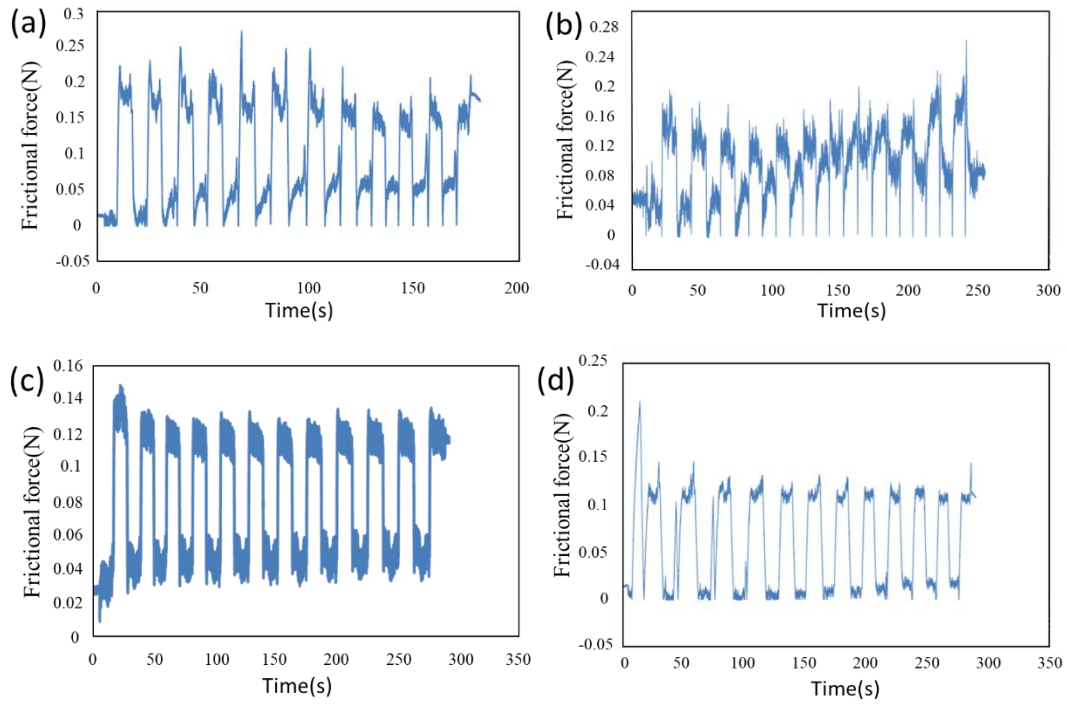
DLC films are characterized by low friction property and high abrasion resistance. The friction behaviors of the uncoated and DLC-coated AZ31 magnesium alloys were examined using a reciprocating probe and wear tester. Generally, both line contact and surface contact probes are available for friction and wear experiments. Line contact between the probe and sample is mainly suitable for observing the deformation of the friction surface in a friction experiment, whereas surface contact is suitable for observing the generation of wear tracks in a wear experiment [15]. In this study, SUS304 was selected as the probe material because of its high hardness and good oxidation resistance. The outer diameter of the reciprocating probe was 4 mm, and the nose part of the probe had an angle of approximately  $100^\circ$  because it is least susceptible to deformation at this angle.



**Fig. 3-6** Schematic diagram of friction test.

A schematic diagram of the friction test is presented in Figure 3-6. The probe reciprocated at a constant sliding distance on the surface of the specimen under the loading force. The friction process and friction surface were monitored using an in situ microscopy system. In addition, the AE signals were converted into friction forces using computer software. The load, sliding speed, sliding distance, and repeated time were 1 N, 20 mm/s, 2 mm, and 300 s, respectively. The evaluation of the friction force is a key factor to illustrate the mechanism of friction and wear. Figure 3-7 shows that the friction force varied with time for the uncoated magnesium alloy substrate and DLC coatings deposited at different flow rates and accelerating voltages after the friction test. The friction force was highest in the first cycle because of the run-in process. The curve of the frictional force fluctuated because of the appearance of wear particles during the friction process. The friction force of the uncoated magnesium alloy substrate was significantly higher than that of the magnesium alloy substrates with DLC films. During the friction process, the friction force on the uncoated magnesium alloy clearly changed and increased to a maximum of 0.28 N, as observed in Figure 3-7(a). The average friction coefficient of the

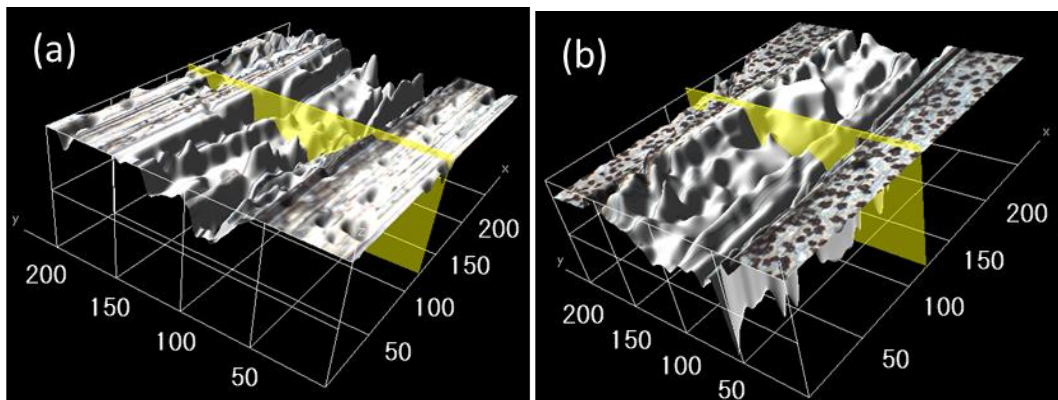
uncoated magnesium alloy AZ31 was approximately 0.23 in the stable stage. The fluctuation of the frictional force curve of the uncoated magnesium alloy AZ31 is due to the high roughness of the surface and larger wear tracks, which may be caused by softening of the magnesium substrate. The friction force of the DLC coating deposited on the magnesium alloy was stable under the same testing conditions. Compared with the uncoated AZ31 magnesium alloy, the DLC films had lowest average friction forces of approximately 0.11 N at 9 sccm/6 kV because of higher  $sp^2/sp^3$  ratio indicating the graphitization of the DLC film. The higher friction force could be related to the reduction in  $sp^2/sp^3$  ratio in the DLC films deposited at 3 sccm/6 kV and 6 sccm/6 kV. The increase of the friction force in the first cycle was mainly caused by the RMS roughness, elastic deformation from both the tip and surface morphology, and intrinsic error of the apparatus [16]. They contributed in different ways to the coefficient of friction. The sudden increase in friction force may be due to a lower film density and a thinner film as observed in Figure 3-7(b). The fluctuations were caused by cracking of the DLC coatings under applied loading. The cracks moved and were detected on the surface especially on uncoated AZ31 magnesium alloy surface. During friction testing, some substances were observed to be transferred from the DLC coating to the probe. The transfer layer served as lubrication consisting of a graphite-like structure [17, 18]. Aboua et al. [19] concluded that the steel counterpart that can be diffused by carbon and bonded with the molecular transformations leads to the low friction force of DLC coating.



**Fig. 3-7** Friction force varies with time of (a) naked magnesium alloy substrate; DLC films deposited at the  $\text{CH}_4/\text{H}_2$  ratio of 1:99 and at (b) 3 sccm/6 kV; (c) 6 sccm/6 kV; (d) 9 sccm/6 kV.

In Figure 3-8, images of the wear morphology and wear traces of the uncoated magnesium alloy substrate (a) and (e), and DLC films deposited on magnesium alloy at 3 sccm/6 kV (b) and (f), 9 sccm/6 kV (c) and (g), and 3 sccm/9 kV (d) and (h) with  $\text{CH}_4/\text{H}_2$  ratio of 1:99 are presented. The numbers of cracks and grooves parallel to the sliding direction could be determined from the wear morphology images of the uncoated AZ31 magnesium alloy surface. The wear traces are deep and broad in Figure 3-8 (a) and (e), indicating the low hardness. The volume of the wear trace was  $2038 \mu\text{m}^3$ . The grinding tracks on the DLC coatings were much narrower and shallower than those on the uncoated AZ31 magnesium alloy. Surface profiles of the wear tracks of the uncoated magnesium alloy substrate and DLC films deposited on the magnesium alloy under different conditions are presented in Figure 3-9. It is necessary to calculate wear volume to evaluate

the wear extent. The wear volume of the wear track was  $819 \mu\text{m}^3$  at 9 sccm/6 kV. For the gas flow rates of 3 and 6 sccm, the wear track volumes were 698 and  $631 \mu\text{m}^3$ , respectively. The wear volumes are consistent with the hardness, which can protect the surface from wear. Once cracks appeared on the DLC films, spallation more easily spread along the surface. Less abrasive debris or spike particles were observed in the wear morphology images of the DLC coatings than in that of the uncoated magnesium alloy. The wear morphology images correspond well to the hardness of the DLC films deposited at different gas flow rates and accelerating voltages. The hardness is consistent with the  $I_D/I_G$  values in Figure 3-3. The lowest  $I_D/I_G$  and highest hardness values of the DLC film deposited at 6 sccm/6 kV corresponded with the least debris at both sides and ends of the grinding cracks in Figure 3-8(c) and (g). The good wear resistance may originate from the combined protection of the smooth surface morphology and high hardness of the DLC films. The DLC coating also exhibited excellent adhesion to the uncoated AZ31 magnesium alloy, with no gaps observed during or after the friction testing. These findings indicate that the DLC coatings improve the friction characteristics of AZ31 magnesium alloy.



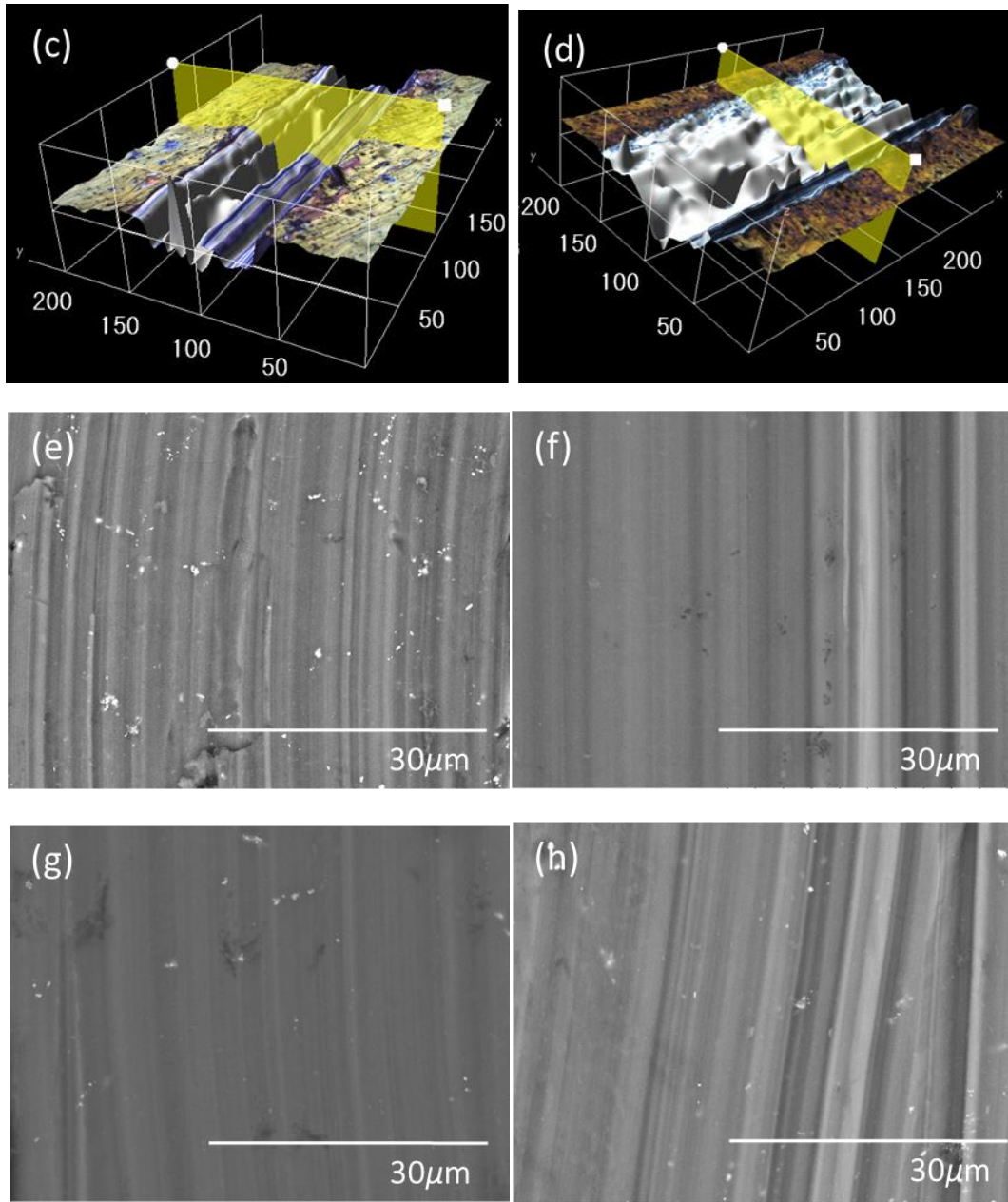


**Fig. 3- 8** Images of wear morphology and wear traces of uncoated magnesium alloy substrate (a) and (e), and DLC films deposited on magnesium alloy at 3 sccm/6 kV (b) and (f); 6 sccm/6 kV (c) and (g); 9 sccm/6 kV (d) and (h) with the  $\text{CH}_4/\text{H}_2$  ratio of 1:99.

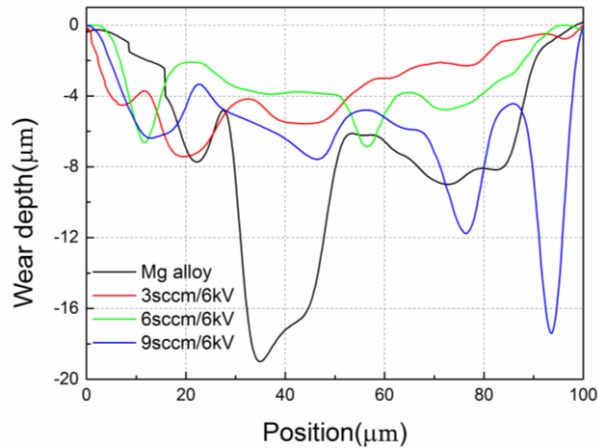


**Fig. 3- 9** Surface profiles of wear tracks of uncoated magnesium alloy substrate and DLC films deposited on the magnesium alloy at different conditions for  $\text{CH}_4/\text{H}_2$  ratio of 1:99.

### 3.5 Summary

The different DLC coatings were successfully deposited on AZ31 magnesium alloy as hard protective coatings using the IBED method by changing the gas flow rate and accelerating voltage. The composition and friction characteristics of the DLC coatings were analyzed to improve the surface performance of magnesium alloy AZ31, and the following observations were made:

(1) The DLC coatings had a lower  $I_D/I_G$ , higher hardness as the accelerating voltage decreased from 9 to 6 kV at the  $\text{CH}_4/\text{H}_2$  ratio of 99:1, and at 6 kV the hardness increased with increasing the gas flow rate from 3 to 9 sccm. The  $I_D/I_G$  ratio decreased and the hardness increased with decreasing  $\text{CH}_4/\text{H}_2$  ratio from 99:1 to 1:99.

(2) No voids or pinholes were observed and the adhesion strength quality were acceptable in the SEM analysis of the DLC films for the  $\text{CH}_4/\text{H}_2$  ratio of 1:99. The  $I_D/I_G$  value decreased, the wear track area decreased, and the hardness increased upon increasing the gas flow rate from 3 to 6 sccm at 6 kV; in addition, less debris was observed

in the wear morphology images of the DLC coatings. The  $I_D/I_G$  decreased to a minimum of 0.62, the hardness increased to a maximum of 4056 HV and the track wear volume decreased to  $631 \mu\text{m}^3$ . The friction force decreased to 0.12 N for the DLC coating deposited at 6 sccm/6 kV. The surface performance of AZ31 magnesium alloy was significantly improved with the deposition of the DLC films at different flow rates and accelerating voltages by enhancing the hardness and friction properties. Future work will involve improving the precipitation hardening of magnesium alloy to improve the supporting effect of the substrate and coating durability.

(3) The  $I_D/I_G$  ratio,  $sp^3$  bond fraction, and hardness increased with increasing gas flow rate from 3 to 6 sccm at a low accelerating voltage. Orbital hybridization between carbon atoms and  $sp^3$  C–C bonds was formed on the surface of the magnesium alloy. The ions with higher energy caused the  $sp^3$  bond to break down into the stable  $sp^2$  bond as the accelerating voltage decreased, resulting in a low  $I_D/I_G$ , high fraction of  $sp^3$  carbon, and high hardness in the DLC films.

(4) An increase of the gas flow rate led to reduction of friction force because the increasing number of  $\text{CH}_x$  group ions generated with  $\text{CH}_4$ , which formed  $sp^3$  and  $sp^2$  hybridizations, reduced the number of C-dangling bonds on the surface. A low gas flow rate enhances dissociation of  $\text{CH}_4$  due to the resident time at the plasma and leads to graphitization of the film structure because of H ion/atom/molecule enrichment.

## References

- [1] J. Cui, L. Qiang, B. Zhang, X. Ling, T. Yang, and J. Zhang, "Mechanical and tribological properties of Ti-DLC films with different Ti content by magnetron sputtering technique," *Applied Surface Science*, vol. 258, no. 12, pp. 5025-5030, 2012.
- [2] K. Furlan, A. Klein, and D. Hotza, "Diamond-like carbon films deposited by hydrocarbon plasma sources," *Rev. Adv. Mater. Sci*, vol. 34, pp. 165-172, 2013.
- [3] W. Dai, X. Gao, J. Liu, S.-H. Kwon, and Q. Wang, "Compositionally modulated multilayer diamond-like carbon coatings with AlTiSi multi-doping by reactive high power impulse magnetron sputtering," *Applied Surface Science*, vol. 425, pp. 855-861, 2017.
- [4] J. Robertson, "Diamond-like amorphous carbon," *Materials science and engineering: R: Reports*, vol. 37, no. 4-6, pp. 129-281, 2002.
- [5] C. Casiraghi, A. Ferrari, and J. Robertson, "Raman spectroscopy of hydrogenated amorphous carbons," *Physical Review B*, vol. 72, no. 8, p. 085401, 2005.
- [6] S. Sattel, J. Robertson, and H. Ehrhardt, "Effects of deposition temperature on the properties of hydrogenated tetrahedral amorphous carbon," *Journal of applied physics*, vol. 82, no. 9, pp. 4566-4576, 1997.
- [7] N. Dwivedi *et al.*, "Probing the role of an atomically thin SiN<sub>x</sub> interlayer on the structure of ultrathin carbon films," *Scientific reports*, vol. 4, p. 5021, 2014.
- [8] Y. Zou *et al.*, "The microstructure, mechanical and friction properties of protective diamond like carbon films on magnesium alloy," *Applied Surface Science*, vol. 258, no. 4, pp. 1624-1629, 2011.
- [9] W. Ding, Y. Guo, D. Ju, S. Sato, and T. Tsunoda, "The effect of CH<sub>4</sub>/H<sub>2</sub> ratio on the surface properties of HDPE treated by CH<sub>x</sub> ion beam bombardment," *Modern Physics Letters B*, vol. 30, no. 17, p. 1650214, 2016.
- [10] J. Liang, M. Chen, W. Tsai, S. Lee, and C. Ai, "Characteristics of diamond-like carbon film synthesized on AISI 304 austenite stainless steel using plasma immersion ion implantation and deposition," *Nuclear Instruments and Methods in Physics Research Section B: Beam Interactions with Materials and Atoms*, vol. 257, no. 1-2, pp. 696-701, 2007.
- [11] X. Li and B. Bhushan, "Micro/nanomechanical and tribological characterization of ultrathin amorphous carbon coatings," *Journal of materials research*, vol. 14, no. 6, pp. 2328-2337, 1999.
- [12] L. Margules, J. Demaison, and J. E. Boggs, "The equilibrium CC bond length,"

- Structural chemistry*, vol. 11, no. 2-3, pp. 145-154, 2000.
- [13] Y. Kayali and S. Taktak, "Characterization and Rockwell-C adhesion properties of chromium-based borided steels," *Journal of Adhesion Science and Technology*, vol. 29, no. 19, pp. 2065-2075, 2015.
- [14] T. Ozdemir and S. Hiziroglu, "Evaluation of surface quality and adhesion strength of treated solid wood," *Journal of Materials Processing Technology*, vol. 186, no. 1-3, pp. 311-314, 2007.
- [15] A. Hase, H. Mishina, and M. Wada, "Fundamental study on early detection of seizure in journal bearing by using acoustic emission technique," *Wear*, vol. 346, pp. 132-139, 2016.
- [16] N. Dwivedi *et al.*, "Ultrathin carbon with interspersed graphene/fullerene-like nanostructures: A durable protective overcoat for high density magnetic storage," *Scientific reports*, vol. 5, p. 11607, 2015.
- [17] A. Voevodin, A. Phelps, J. Zabinski, and M. Donley, "Friction induced phase transformation of pulsed laser deposited diamond-like carbon," *Diamond and Related Materials*, vol. 5, no. 11, pp. 1264-1269, 1996.
- [18] A. Erdemir, C. Bindal, G. Fenske, C. Zuiker, and P. Wilbur, "Characterization of transfer layers forming on surfaces sliding against diamond-like carbon," *Surface and Coatings Technology*, vol. 86, pp. 692-697, 1996.
- [19] K. A. M. Aboua *et al.*, "Effect of carbon diffusion on friction and wear properties of diamond-like carbon in boundary base oil lubrication," *Tribology International*, vol. 113, pp. 389-398, 2017.

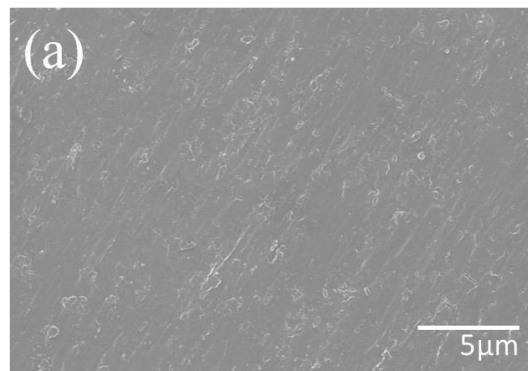
# Chapter 4 Microstructure analysis and corrosion resistance of DLC films-coated titanium

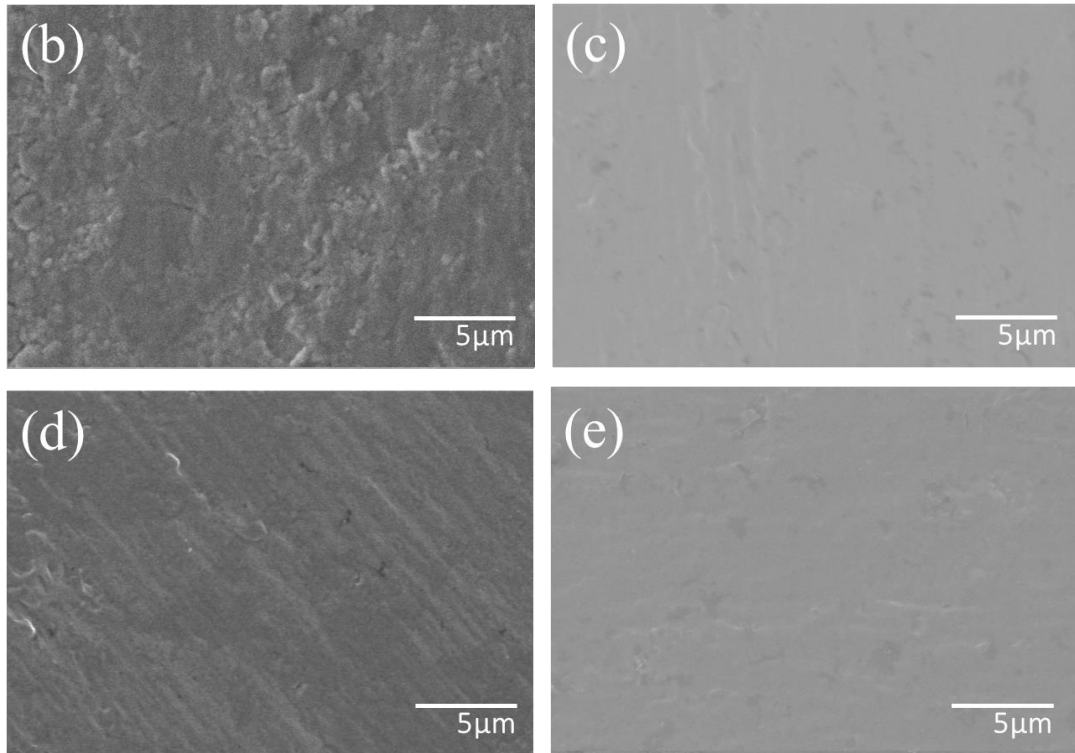
## 4.1 Surface and cross-section morphology of DLC films

### deposited on titanium

#### 4.1.1 Surface morphology and roughness

The surface morphology of the DLC films were observed using a scanning electron microscope (SEM). The surface morphology images of titanium (a); and the DLC films deposited at (b) gas ratios  $\text{CH}_4/\text{H}_2 = 1:1$ , 6hrs; (c) gas ratios  $\text{CH}_4/\text{H}_2 = 1:1$ , 12hrs; (d) gas ratios  $\text{CH}_4/\text{H}_2 = 1:0$ , 6hrs; (e) gas ratios  $\text{CH}_4/\text{H}_2 = 1:0$ , 12hrs are presented in Fig. 4-1. The DLC films are observed to be dense and composed of spherical particles with diameters of  $0.2\sim 1.6\ \mu\text{m}$  on the entire titanium surface. The surface morphologies of DLC films deposited at  $\text{CH}_4/\text{H}_2=1:0$  show a smoother surface and a smaller granules than that of DLC films at  $\text{CH}_4/\text{H}_2=1:1$ . Thus the high  $\text{CH}_4$  ratio is beneficial for the smooth surface morphology with almost no pinholes. Therefore the DLC films can be used to protect titanium substrate from the acidic corrosion solution. The high  $\text{CH}_4$  ratio and long processing time are more beneficial for the denser deposition of DLC films.

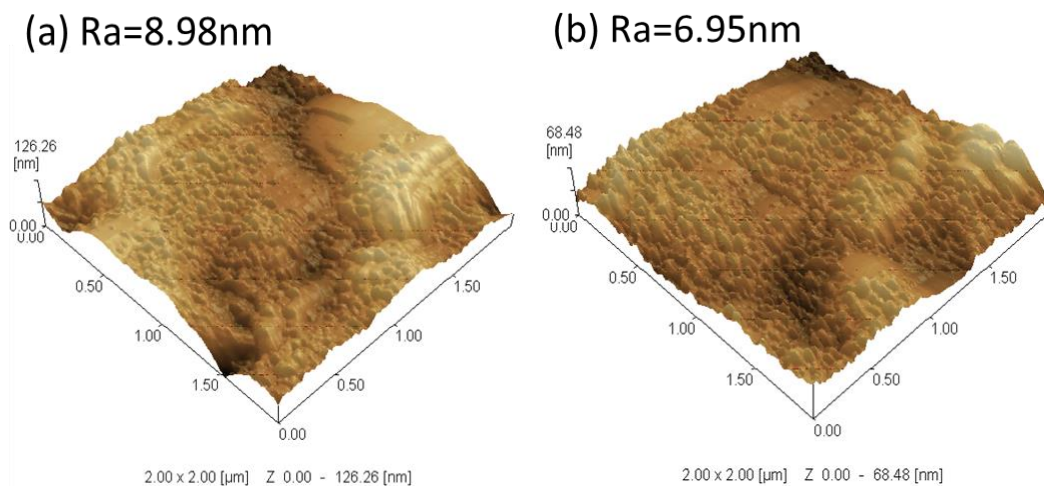




**Fig.4- 1** SEM image of titanium substrate (a); and the DLC film deposited at gas ratios  $\text{CH}_4/\text{H}_2 = 1:1$ , 6hrs (b); gas ratios  $\text{CH}_4/\text{H}_2 = 1:1$ , 12hrs (c); gas ratios  $\text{CH}_4/\text{H}_2 = 1:0$ , 6hrs (d); gas ratios  $\text{CH}_4/\text{H}_2 = 1:0$ , 12hrs (e).

Fig. 4-2 presents the AFM images and average roughness values of random ( $2\mu\text{m}\times 2\mu\text{m}$ ) areas of DLC films-coated titanium. From the figures, it can be seen that the undulating hills with a height of about 126.26 nm, 68.48 nm, 91.75 nm and 66.03 nm appear on the surface of bare and DLC films respectively. The average roughness values  $R_a$  of DLC films at  $\text{CH}_4/\text{H}_2=1:0$  are 7.38nm and 5.76nm, which are lower than that of DLC films at  $\text{CH}_4/\text{H}_2=1:1$ , 8.98nm and 6.95nm. The undulating hills became more flattened with increasing  $\text{CH}_4$  ratio which has the higher  $sp^3$  content. An increase in the  $\text{H}_2$  ratio led to an increase in the surface roughness. These changes may be caused by the etching effect [1]. Liang et al. [2] suggested that hydrogen etching was a variable affecting the surface

roughness. During the deposition process, the titanium surface was destroyed. In addition, the incident  $\text{CH}_x$  group ions can chemically react on the titanium surface, forming  $sp^3$  and  $sp^2$  hybridizations. An abundance of  $sp^3$  and  $sp^2$  carbon leads to the growth of  $\text{CH}_x$  groups on the titanium surface. However, for growth of the  $\text{CH}_x$  group on the surface, the H ions/atoms/molecules promoted  $sp^3$  hybridization. As a result, the competition between  $\text{CH}_x$  group ions and H groups as well as the etching and growth effects on the titanium surface must be considered. Many dangling C-bonds were observed on the surface because of the small amounts of H ions/atoms/molecules in the ion beam. The dangling C-bonds on the surface could not be completely saturated, leading to the growth of incident  $\text{CH}_x$  groups on the titanium surface. Therefore, the growth effect dominates the deposition process as the  $\text{CH}_4$  ratio increases, which leads to a smoother surface. The results are consistent with the surface SEM images.



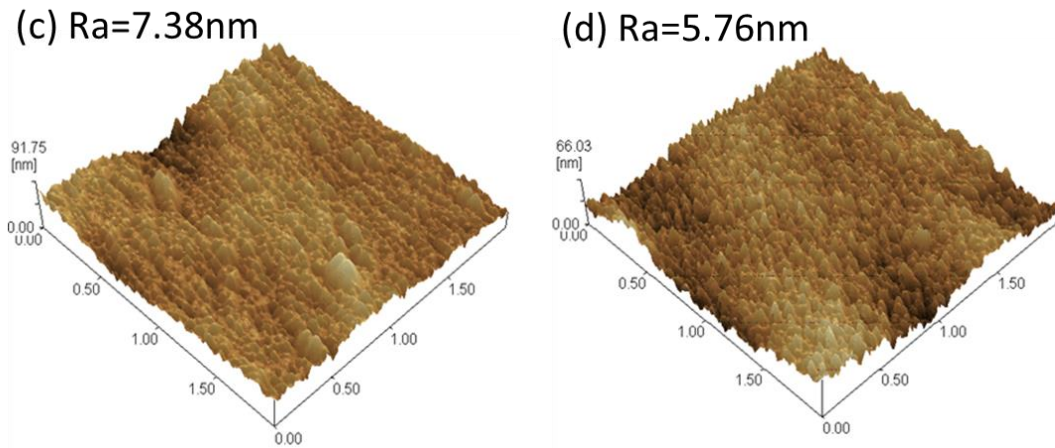


**Fig.4- 2** AFM images of DLC films deposited on titanium at (a) gas ratios  $\text{CH}_4/\text{H}_2 = 1:1$ , 6hrs; (b) gas ratios  $\text{CH}_4/\text{H}_2 = 1:1$ , 12hrs; (c) gas ratios  $\text{CH}_4/\text{H}_2 = 1:0$ , 6hrs; (d) gas ratios  $\text{CH}_4/\text{H}_2 = 1:0$ , 12hrs.

#### 4.1.2 Cross-sectional morphology and thickness

The cross-section morphology of the DLC films were observed using a scanning electron microscope. The cross-section morphology images of titanium (a) and the DLC films deposited at (b)  $\text{CH}_4/\text{H}_2 = 1:1$ , 6hrs; (c)  $\text{CH}_4/\text{H}_2 = 1:1$ , 12hrs; (d)  $\text{CH}_4/\text{H}_2 = 1:0$ , 6hrs; (e)  $\text{CH}_4/\text{H}_2 = 1:0$ , 12hrs are presented in Fig. 4-3. The DLC films are compact and dense covering the entire titanium surface. The thickness of the fully dense coating cannot be clearly defined because of the permeation layer. The DLC layer has a maximum thickness of about 1281nm from the Fig. 4-3(d). The average thickness of the DLC film-coated stainless steel is about 533.7nm, 581.7nm and 693.9nm respectively from the Fig. 4-3(a), (b) and (c). The thickness of the fully dense DLC films increases significantly with the deposition time. The DLC film with larger density is considered to better prevent the titanium substrate from direct corrosion. With the increase of time, the high-energy ion beams continuously bombard the growing film. So the coating atoms are penetrated into the substrate with more energy, which increases the thickness of the fully dense coating

and the permeation layer [3-4]. All the DLC films on the surface are very dense, and no gaps were found between the DLC coating and substrates, indicating the good adhesion.

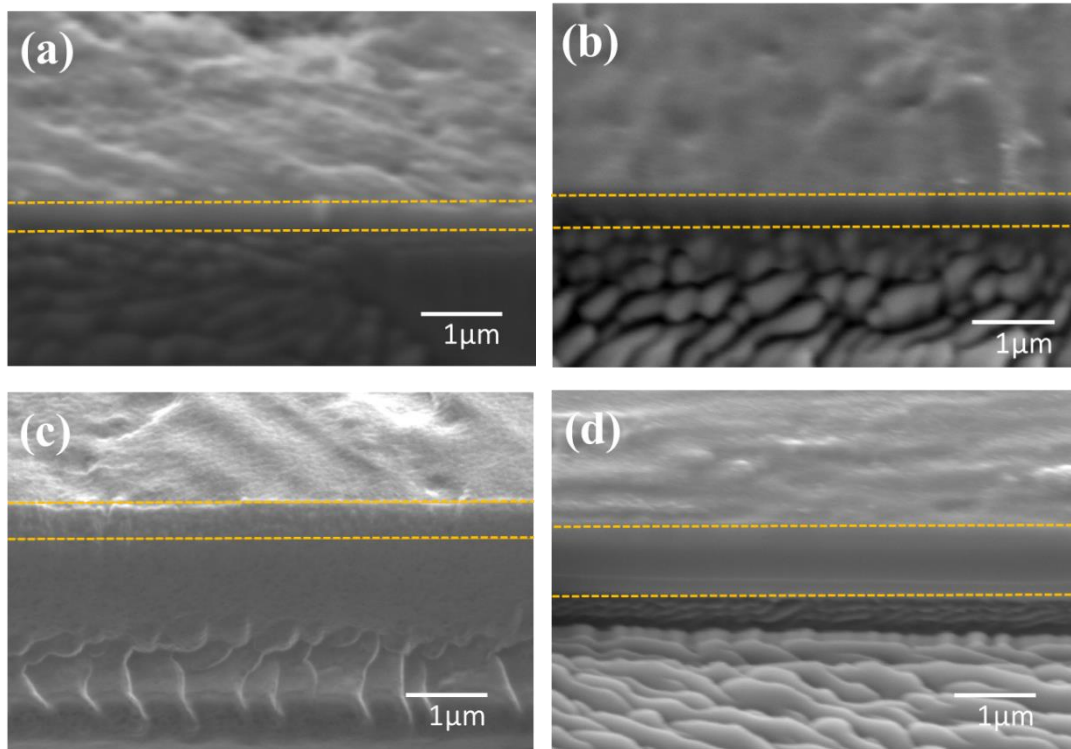


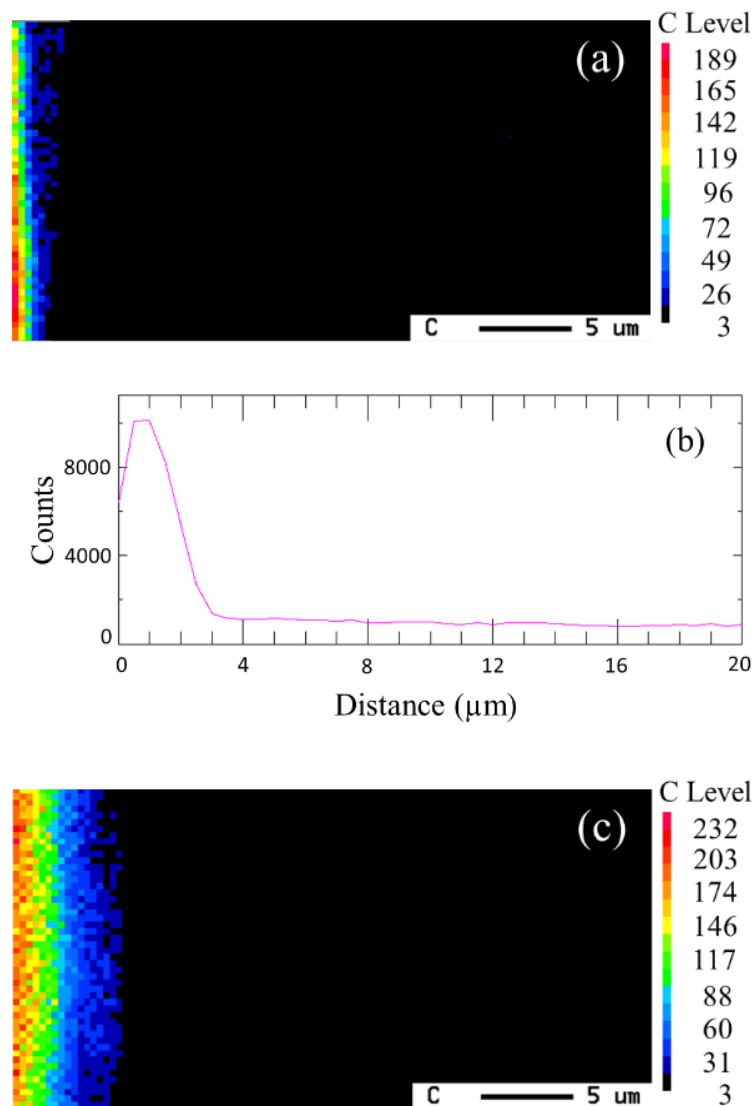
**Fig.4- 3** Cross-section SEM image of the DLC films deposited at (a)  $CH_4/H_2 = 1:1$ , 6hrs; (b)  $CH_4/H_2 = 1:1$ , 12hrs; (c)  $CH_4/H_2 = 1:0$ , 6hrs; (d)  $CH_4/H_2 = 1:0$ , 12hrs.

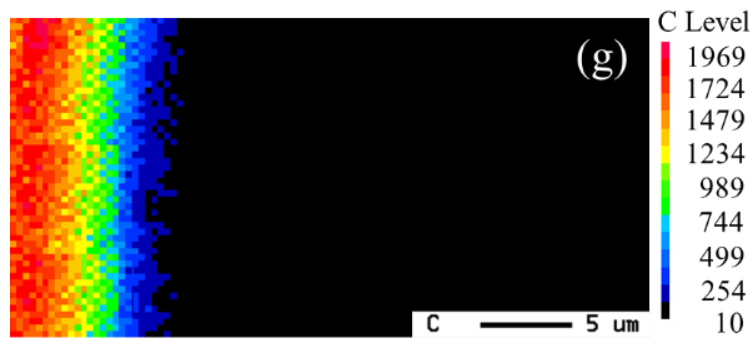
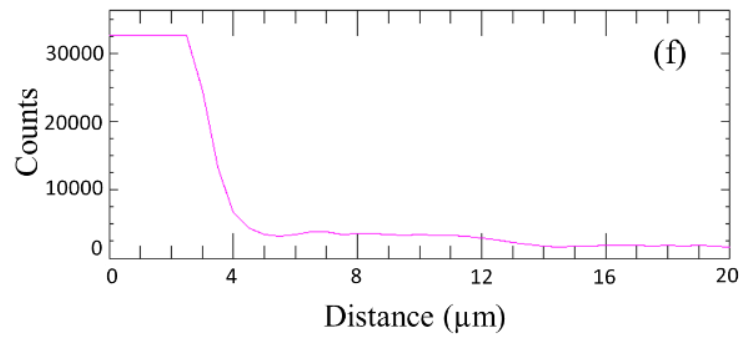
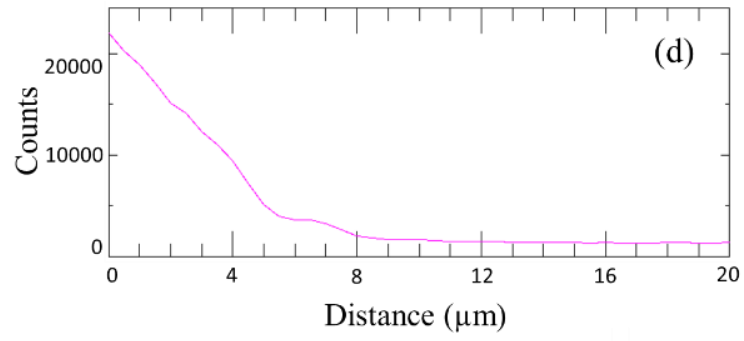
**Table 4- 1** Thickness of DLC films-coated titanium deposited at different conditions

	$CH_4/H_2 = 1:1$	$CH_4/H_2 = 1:1$	$CH_4/H_2 = 1:0$	$CH_4/H_2 = 1:0$
	6h	12h	6h	12h
<b>Thickness(<math>\mu m</math>)</b>	0.5337	0.5871	0.6939	1.2810

The carbon element concentration distribution and cross-section morphology of DLC films-coated titanium are determined by EPMA. The sample to be analyzed is bombarded

by an electron beam which would emit x-rays with wavelengths characteristic to specific elements. Then the concentration distribution and diffusivities of elements can be obtained accurately by EPMA mapping [5-7]. The average thickness of the carbon permeation layer is about 3  $\mu\text{m}$ , 4 $\mu\text{m}$ , 4 $\mu\text{m}$  and 12  $\mu\text{m}$  respectively from the Figure 4-4 b, d, f, h. The carbon concentration of DLC film deposited at  $\text{CH}_4/\text{H}_2=1:0$  is higher than that of  $\text{CH}_4/\text{H}_2=1:1$ . As the increase of deposition time, the penetration depth becomes thicker because of the increase in high-energy ion beam at the deposition time of 12 h.





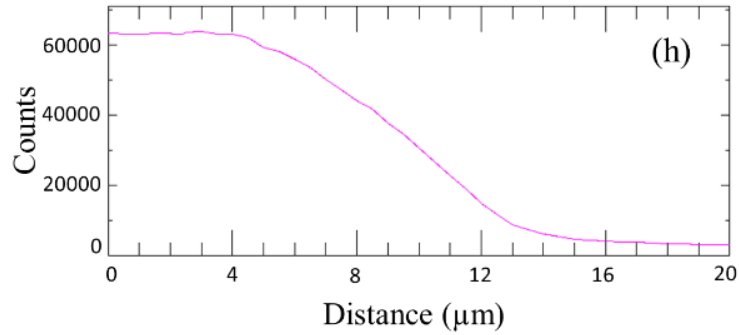


Fig.4- 4 EPMA mappings of carbon element and line scans of carbon intensity of DLC film cross-section deposited at (a) and (b)  $\text{CH}_4/\text{H}_2 = 1:1$ , 6 h; (c) and (d)  $\text{CH}_4/\text{H}_2 = 1:1$ , 12 h; (e) and (f)  $\text{CH}_4/\text{H}_2 = 1:0$ , 6 h; (g) and (h)  $\text{CH}_4/\text{H}_2 = 1:0$ , 12 h.

## 4.2 Chemical composition and microstructure analysis of DLC films deposited on titanium

### 4.2.1 Raman spectroscopy of DLC films on titanium

The Raman spectroscopy is a non-destructive and routine method for characterizing the bonding structure of carbon films. The Raman spectra of DLC films had this feature which has been shown previously [8]. The wide peak of DLC film is created by overlapping two peaks, G (graphite) peak and D (disorder) peak. The G peak is resulted from stretching mode of all pairs of  $\text{sp}^2$  sites (both olefinic and aromatic), while the D peak results from breathing mode of all pairs of  $\text{sp}^2$  sites that are only located in aromatic rings [9]. The bonding state of a-C: H DLC coating was evaluated by three key Raman parameters: the intensity ratio of D-peak and G-peak ( $I_D/I_G$ ), the full width at half maximum of G-peak (FWHM) and the position of G-peak. The Raman spectra of DLC films deposited at different conditions are shown in Fig. 4-5. The D-peak and G-peak were identified at approximately  $1360 \text{ cm}^{-1}$  and  $1560 \text{ cm}^{-1}$  corresponding to disordered

band (arising from bond stretching of  $sp^2$  atoms in rings and chains) and the graphite band (arising from breathing modes of  $sp^2$  atoms in rings), respectively. The  $I_D/I_G$  and G-peak position are considered to have a linear relationship with the graphite crystallite size [10]. FWHM (G) is mainly sensitive to structure disorder which originating from bond angle and bond length. The rise in FWHM (G) demonstrates an increase in the angle and length distortion of the  $sp^2$ -C bond. For a-C:H films with  $sp^3$  content ( $>20\%$ ), a shift of the G-peak position to higher wavenumbers is consistent with an increase  $sp^3$  ratio [11]. A higher FWHM (G) and smaller  $I_D/I_G$  lead to a higher film density [12]. The reason for shifting the G peak position from a low wavenumber to a higher wavenumber is the presence of compressive stress in the DLC-coated titanium. The  $I_D/I_G$  ratio decreased, G-peak position shifted toward higher wavenumber and the FWHM (G) increased with increasing  $CH_4$  ratio and deposition time as shown in Table 4-2, indicating the increasing  $sp^3$  C-C bonds fraction and film density. The detailed Raman features are listed in Table 4-2.

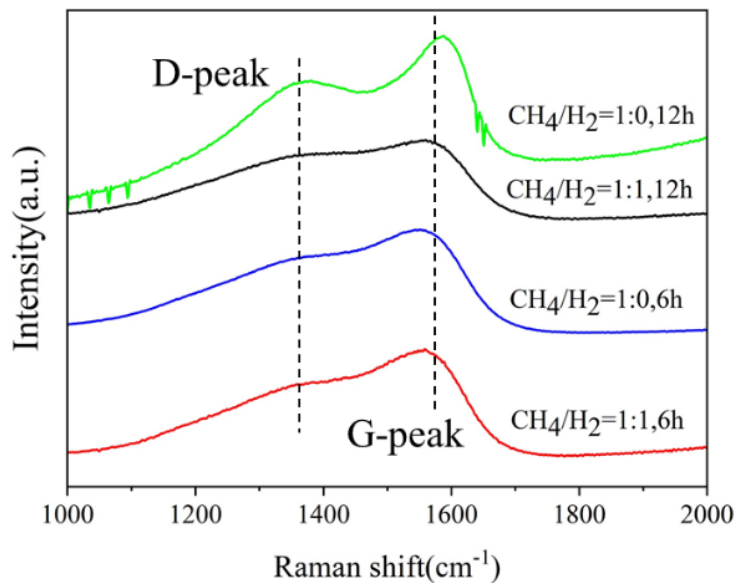


**Fig.4- 5** Typical Raman spectrum of DLC films deposited on titanium at different conditions.

**Table 4- 2** ID/IG ratio, G-peak position and FWHM (G) of DLC films deposited on titanium at different conditions

<i>Ti</i>	<i>CH<sub>4</sub>/H<sub>2</sub> =1:1</i>	<i>CH<sub>4</sub>/H<sub>2</sub> =1:1</i>	<i>CH<sub>4</sub>/H<sub>2</sub> =1:0</i>	<i>CH<sub>4</sub>/H<sub>2</sub> =1:0</i>
	<i>6h</i>	<i>12h</i>	<i>6h</i>	<i>12h</i>
<i>I<sub>D</sub>/I<sub>G</sub></i>	<i>0.877</i>	<i>0.853</i>	<i>0.835</i>	<i>0.827</i>
<i>G-peak(cm<sup>-1</sup>)</i>	<i>1556.59</i>	<i>1557.96</i>	<i>1560.55</i>	<i>1565.77</i>
<i>FWHM(G )(cm<sup>-1</sup>)</i>	<i>133.81</i>	<i>134.23</i>	<i>135.31</i>	<i>138.68</i>

#### 4.2.2 TEM analysis of DLC films on titanium

In order to study the microstructure of the DLC film further, the equipment of Transmission Electron Microscope (TEM) HF-3300 was applied. Before the experiment of TEM, the sample for investigation was prepared. At first, the thickness of the sample was about 0.1 mm, then the sample was processed to about 0.1 $\mu$ m by fine finishing with the application of Focused Ion Beam Scanning Electron Microscopes (FIB-SEM). The SEM image was shown in Fig.4-6. It can be seen that the width of the substrate section decreased gradually with the increasing number of processes. Actually, the width was 20  $\mu$ m in the first process, and 6 $\mu$ m in the last process.

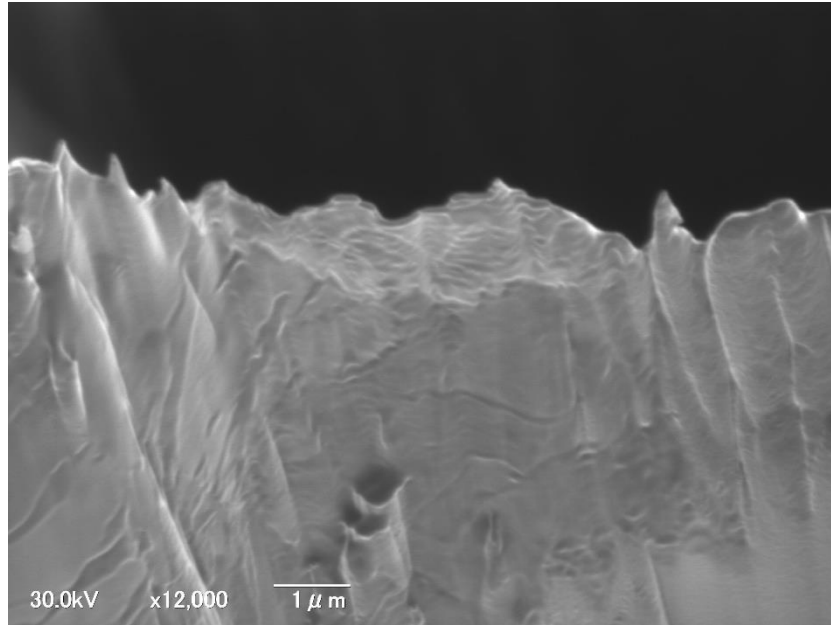


**Fig.4- 6** SEM image of the DLC film deposited on titanium after FIB process.

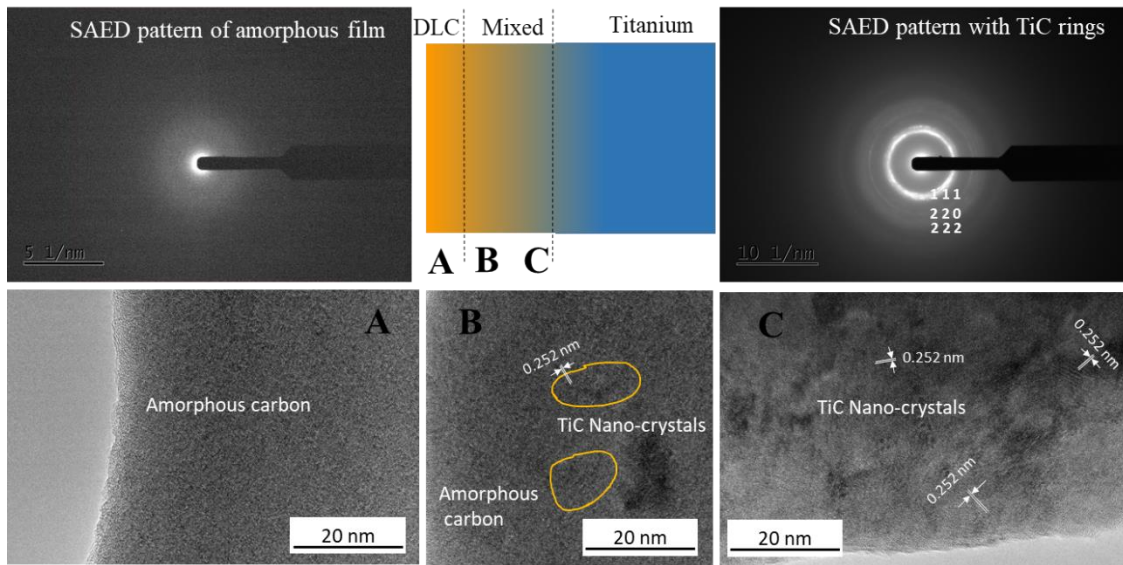


**Fig.4- 7** Schematic diagram TEM images of the DLC film deposited on titanium at  $\text{CH}_4/\text{H}_2$   
=1:0,12h

The schematic diagram and TEM images of DLC film deposited on titanium at  $\text{CH}_4/\text{H}_2$   
=1:0,12h were shown in figure 4-7. The selected area electron diffraction pattern (SAED)  
of amorphous DLC film and nano-crystals were also shown in figure 4-7. TEM  
characterization of pure DLC layer confirmed the amorphous phase microstructure as

shown in figure 4-7 A section, which is in good agreement with previous studies [13-14]. Figure 4-7 B and C sections shown the high-resolution TEM micrographs, taken with the TiC rings. A small amount of TiC nanocrystalline phase was surrounded by an amorphous matrix from Figure 4-7 section B. Then the nano-crystal area became larger from Figure 4-7 section C. It indicates the penetration process of DLC atoms in the titanium substrate. The interplanar spacing can be identified according to the results of calculation based on the diffraction images. The d values calculated from the diffraction pattern using the formula

$$\lambda L = rd \quad (4-1)$$

where r is the radius of the diffraction ring,  $\lambda$  is the wavelength of the electron beam and L is the distance of the photographic plate from the sample, (The product  $\lambda L = A$ , called the camera constant). Polycrystalline rings indexable to the (111), (220) and (222) reflections of cubic TiC are present in the figure. The average cubic TiC lattice constants obtained from electron diffraction pattern is 2.50 Å, which agrees well with the value obtained from TEM images. The absence of other crystalline diffraction signatures in figure 4-7 suggests that only the cubic form of TiC is present in the DLC film and that the hydrocarbon matrix is amorphous [15].

#### 4.2.3 XPS analysis of DLC films on titanium

The bonding structure of DLC films deposited on titanium at different conditions were evaluated by XPS spectroscopy. In order to give a trustful result, the metallic oxide contaminations from the environment was removed by Ar<sup>+</sup> bombardment [16]. After removing the contaminations, C1s and Ti 2p XPS spectrum scan of DLC films deposited on the titanium are shown in the Figure 4-8 and 4-9. It can be seen that the main bond on

the surface of the DLC film are C-C, Ti-C and O-C=O, and their binding energies are about 285.1 eV, 282±0.1 eV and 289.1 eV, respectively [17]. The oxygen percentage of DLC films deposited at CH<sub>4</sub> = 1:1, 6 h; CH<sub>4</sub>/H<sub>2</sub> = 1:1, 12 h; CH<sub>4</sub>/H<sub>2</sub> = 1:0, 6 h and CH<sub>4</sub>/H<sub>2</sub> = 1:0, 12 h is about 35.1%, 31.8%, 31.7% and 23.3% respectively, indicating a gradual decrease with the deposition time. It is known that DLC coatings with less C=O and C-O bonds suggesting a denser coating [18]. The results are in accordance with the EPMA analysis and Raman analysis.

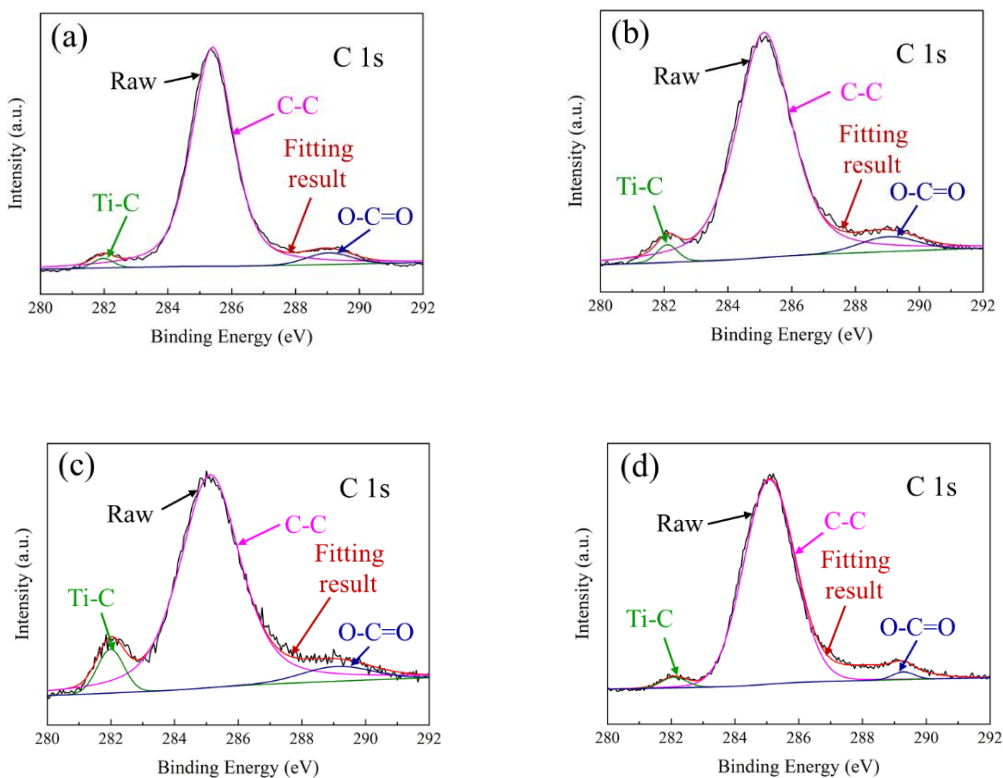


**Fig.4- 8** XPS spectra for Ti 2p of DLC films deposited on titanium at (a) CH<sub>4</sub>/H<sub>2</sub> =1:1, 6hrs; (b) CH<sub>4</sub>/H<sub>2</sub> =1:1, 12hrs; (c) CH<sub>4</sub>/H<sub>2</sub> =1:0, 6hrs; (d) CH<sub>4</sub>/H<sub>2</sub> =1:0, 12hrs.

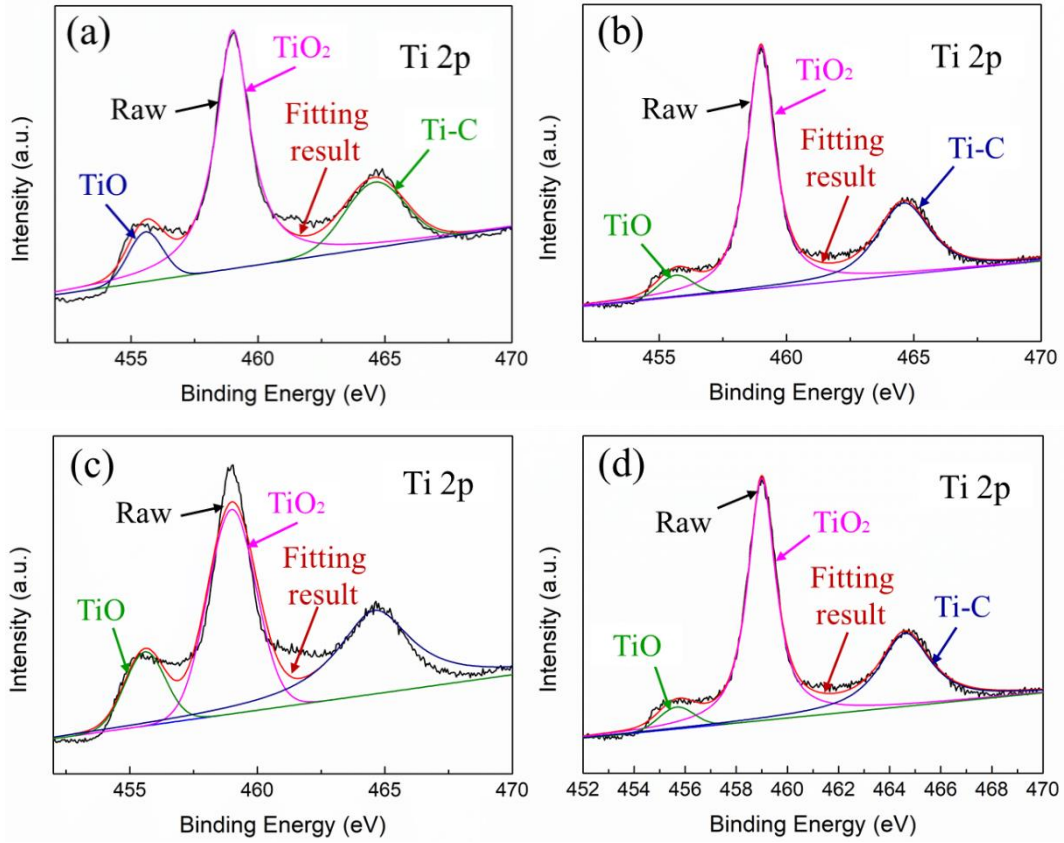


**Fig.4- 9** XPS spectra for Ti 2p of DLC films deposited on titanium at (a)  $\text{CH}_4/\text{H}_2 = 1:1$ , 6hrs; (b)  $\text{CH}_4/\text{H}_2 = 1:1$ , 12hrs; (c)  $\text{CH}_4/\text{H}_2 = 1:0$ , 6hrs; (d)  $\text{CH}_4/\text{H}_2 = 1:0$ , 12hrs.

### 4.3 Interfacial Contact Resistance of DLC films deposited on titanium

The high conductivity of metallic bipolar plates play a vital role in improving the output power efficiency of PEMFC. Therefore the ICR was obtained by subtracting the resistance of the substrate from the resistance of a-C:H film-coated titanium [19]. The ICR of substrate and DLC films at  $150 \text{ N/cm}^2$  are listed in Table 4-3. The DLC film deposited at  $\text{CH}_4/\text{H}_2 = 1:1$ , 6 h showed lowest resistance of  $7 \text{ m}\Omega\cdot\text{cm}^2$  which is lower than the Department of Energy's (DOE) target (2020) of  $10 \text{ m}\Omega\cdot\text{cm}^2$  [20]. The ICR increases as the  $\text{CH}_4$  ratio increases to 100% because the good conductive performance

depends on high content of  $sp^2$ -C bonds. The ICR results are consistent with Raman spectroscopy [21].

**Table 4- 3** ICR of DLC-coated titanium

	<i>Ti</i>	<i>CH<sub>4</sub>/H<sub>2</sub> =1:1</i>	<i>CH<sub>4</sub>/H<sub>2</sub> =1:1</i>	<i>CH<sub>4</sub>/H<sub>2</sub> =1:0</i>	<i>CH<sub>4</sub>/H<sub>2</sub> =1:0</i>
	<i>substrate</i>	<i>6h</i>	<i>12h</i>	<i>6h</i>	<i>12h</i>
<b><i>ICR (mΩ·cm<sup>2</sup>)</i></b>	<i>5</i>	<i>7</i>	<i>17.3</i>	<i>16.5</i>	<i>22.4</i>

## 4.4 Corrosion resistance of DLC films-coated titanium

### 4.4.1 Surface characteristics of DLC films-coated titanium after corrosion

The surface morphology images of titanium (a); and the DLC films deposited at (b)  $CH_4/H_2 = 1:1$ , 6hrs; (c)  $CH_4/H_2 = 1:1$ , 12hrs; (d)  $CH_4/H_2 = 1:0$ , 6hrs; (e)  $CH_4/H_2 = 1:0$ , 12hrs after corrosion test are presented in Fig. 4-10. It can be observed that bare substrate was destroyed and some cracks appear on the surface. The area of localized corrosion becomes larger as  $CH_4/H_2 = 1:0$  decreases to  $CH_4/H_2 = 1:1$ . In the corrosion test of high temperature acidic solution of 168 hours, a small amount of corrosion solution penetrates into the film and contacts with titanium substrate, resulting in pitting corrosion. In addition, the local region is suffered from accelerated corrosion rate due to the pitting.

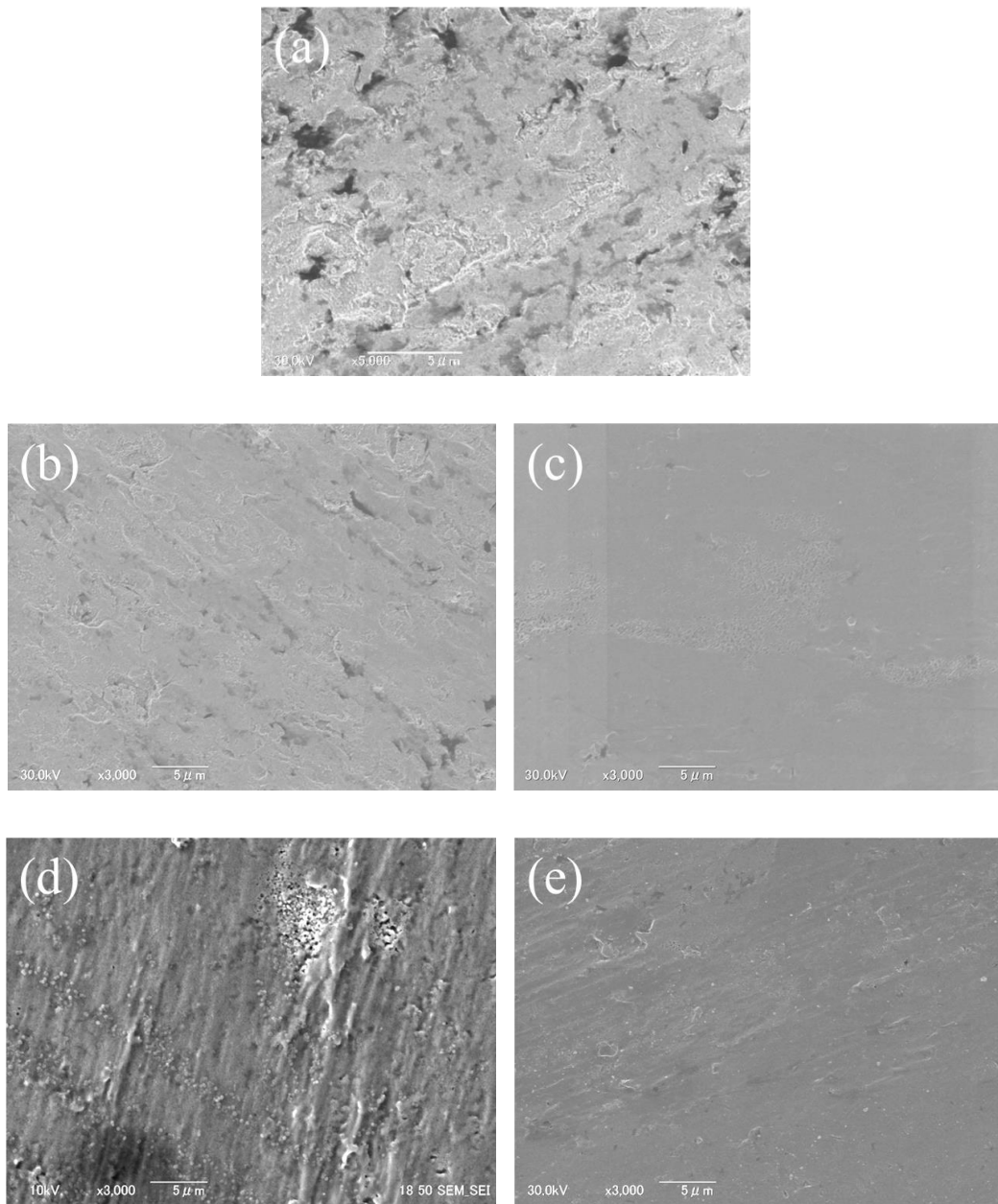


**Fig.4- 10** SEM images of titanium substrate (a); and the DLC film deposited at gas ratios  $\text{CH}_4/\text{H}_2 = 1:1$ , 6hrs (b); gas ratios  $\text{CH}_4/\text{H}_2 = 1:1$ , 12hrs (c); gas ratios  $\text{CH}_4/\text{H}_2 = 1:0$ , 6hrs (d); gas ratios  $\text{CH}_4/\text{H}_2 = 1:0$ , 12hrs (e).

The Raman spectrum of DLC films with different deposition conditions after potentiostatic corrosion test are presented in Figure 4-11. Compared to Raman results

before corrosion, the G-peak position shifted toward higher wavenumber while the  $sp^3$  C-C fraction increased. It is probably due to a small amount of the film peeling off from the sample surface. The Raman spectra results reveal that the anti-corrosion behavior of DLC films deposited at 12 h with smoother curves is better than that of DLC films deposited at 6 h. In addition, the peak intensity of DLC films is stronger at the condition of  $CH_4/H_2=1:0$ .

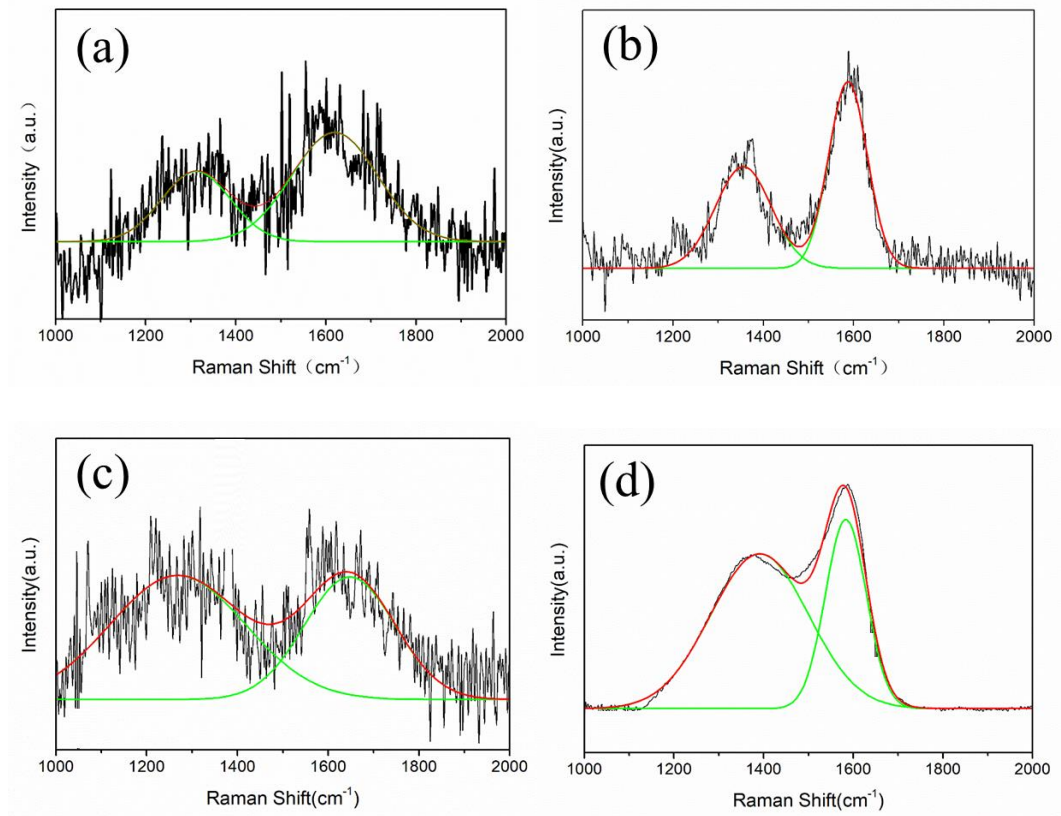


**Fig.4- 11** Typical Raman spectrum of DLC films deposited on titanium at (a)  $CH_4/H_2 = 1:1$ , 6hrs; (b)  $CH_4/H_2 = 1:1$ , 12hrs; (c)  $CH_4/H_2 = 1:0$ , 6hrs; (d)  $CH_4/H_2 = 1:0$ , 12hrs.

#### 4.4.2 Effect of DLC films on metal ions dissolution

Metal ions concentration in corrosion solution are important for evaluating the

corrosive resistance of bipolar plate. Concentrations of the metal ions in the solutions after corrosion test were analyzed by an Inductively Coupled Plasma (ICP) Emission Spectroscopy (ICPS-7000 Sequential Plasma Spectrometer, SHIMADZU Corporation). The results of the bare and DLC films-coated titanium are summarized in Table 4-4. Contrary to the uncoated titanium (about 0.58 ppm), the metal ions dissolved in the liquid has a significant reduction (0.34~0.49 ppm), indicating that the DLC films play an important role on protecting the substrate. There are hydrogen ions in the corrosive solution, forming a strong corrosion layer and accelerating the corrosion rate [22]. Titanium ions concentration of DLC films-coated titanium deposited at CH<sub>4</sub> 100%, 12h (about 0.34 ppm) is obviously lower than that of others. The higher density of DLC films with gas CH<sub>4</sub> 100% prevents the acidic solution from reacting with titanium substrate. The smoother surface of DLC films-coated titanium has the higher anti-corrosion resistance because of the smaller contact area. The higher oxygen content of DLC film deposited at CH<sub>4</sub>/H<sub>2</sub> = 1:1 also accelerates corrosion rate in an acidic solution. The result is consistent with the SEM and AFM analysis.

**Table 4- 4** Metal ions concentration for the bare and DLC films after 168 h corrosion. (ppm)

<i>Ti</i>	<i>CH<sub>4</sub>/H<sub>2</sub> = 1:1,</i>		<i>CH<sub>4</sub>/H<sub>2</sub> = 1:0,</i>		
	<i>6h</i>	<i>12h</i>	<i>6h</i>	<i>12h</i>	
<b><i>Ti (ppm)</i></b>	<i>0.58</i>	<i>0.49</i>	<i>0.43</i>	<i>0.37</i>	<i>0.34</i>

#### 4.4.3 Electrochemical behaviors of DLC films deposited on titanium

The electrochemical behaviors of all samples were analyzed in 0.5 M sulfuric acid

solution at 90 °C by conventional three-electrode system. The DLC-coated titanium sample was acted as working electrode respectively, a platinum sheet as counter electrode, and a saturated calomel electrode (SCE) as the reference electrode [23]. The sample was cut to a size of 20 × 20 mm<sup>2</sup> by a circular saw after the deposition and then sealed with epoxy resin and exposed one end with an area of 10 × 10 mm<sup>2</sup>. The polarization curves of titanium and DLC films-coated titanium in 0.5 mol/L sulfuric acid solution purged with air at 90 °C are shown in Figure 4-12. The high active peak of titanium could be viewed because of the active dissolution and the oxidation. In comparison with the bare, the DLC films-coated titanium exhibit a more noble corrosion potential and more stable passive region in simulated cathode condition. Corrosion potential reaches a maximum of about 0.15 V at the condition of CH<sub>4</sub>/H<sub>2</sub>= 1:0, 12 h, which is significantly greater than the bare of about -0.34 V. The higher corrosion potential usually implies the better corrosion resistance because of the higher electrochemical stability [24]. At the cathode potential of around 0.6 V under the fuel cell operating condition, the corrosion current density of the bare is about 1.8 μA/cm<sup>2</sup>. As for the DLC films-coated titanium, the corrosion current density is reduced to a minimum of 0.23 μA/cm<sup>2</sup> at CH<sub>4</sub>/H<sub>2</sub> = 1:0, 12 h. All the corrosion current density of DLC films meet the DOE's 2020 target of 1 μA/cm<sup>2</sup> (0.5 mol/L H<sub>2</sub>SO<sub>4</sub> solution with 5 ppm HF, 70 °C) [25]. A smaller current density means a lower corrosion rate. All the DLC films-coated titanium exhibit the similar electrochemical behaviors. The DLC films on the surface could protect titanium from contacting sulfuric acid solution, so as to avoid corrosion. The DLC films deposited at CH<sub>4</sub>/H<sub>2</sub> = 1:0 and longer deposition time of 12 h have the better electrochemical behavior and higher corrosion resistance due to the intrinsic microstructure properties from the surface morphology, which are in accordance with the ICP results. The polarization behavior under the anode

condition was not examined because the corrosion behavior of anode condition would be weak [26].

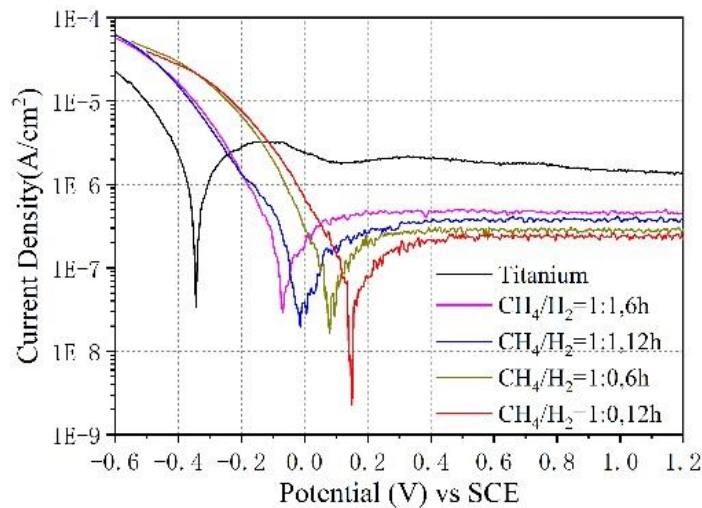


**Fig.4- 12** Potentiodynamic behaviors of uncoated titanium and various DLC films-coated titanium in 0.5 mol/L H<sub>2</sub>SO<sub>4</sub> at 90 °C.

## 4.5 Summary

The dense and uniform DLC films as protective film were successfully deposited on titanium substrates using IBED technique by changing the gas ratio CH<sub>4</sub>/H<sub>2</sub> and deposition time. Compared with the other coating techniques, the IBED method has many advantages such as lower compressive stress due to the production of a graded interfacial, higher film-substrate adhesion and better surface properties of high-precision parts, which enables a series of beneficial surface property modifications without detrimentally affecting the bulk properties. The microstructure properties of the films were evaluated taking into account for different deposition conditions. No voids or pinholes were observed obviously in the SEM analysis of all the DLC films. The pinhole could be

regarded as passageway for the corrosion liquid. Then the corrosion liquid can penetrate through the passageway and corrode the interface which results in the metal ion release even causes coating delamination.

The roughness and  $I_D/I_G$  ratio are lower at  $CH_4/H_2=1:0$ , while the Ra and  $sp^3$  bond fraction decrease with increasing deposition time from 6h to 12h. An increase in the  $H_2$  ratio led to an increase in the surface roughness may be caused by the hydrogen etching effect. The ICR increases as the  $CH_4$  ratio increases because the good conductive performance depends on high content of  $sp^2$ -C bonds. The DLC with low  $sp^3$  fraction ordinarily has low internal stress. Although high values of compressive stress should be avoid in coating preparation, nevertheless, it is also found that a moderate compressive stress could be helpful in the corrosion inhibition process. In particular, propagation of delamination through the coating layer can be suppressed by compressive residual stress, which causes the shrinkage of open corrosion path in the coatings. Meanwhile the nanocrystalline TiC phase is observed from penetration layer of DLC films-coated titanium which has the strong and stable chemical bond energy holding Ti atoms and C atoms together. The DLC film can protect the substrate from corrosion due to its densification and chemical inertness.

The DLC film deposited at  $CH_4/H_2 = 1:0$  is denser than at  $CH_4/H_2 = 1:1$  from the SEM and EPMA images. The metal ions contaminant concentration of a-C:H coating deposited at  $CH_4/H_2 = 1:0$  is also obviously lower than at  $CH_4/H_2 = 1:1$ . And the DLC film has the lowest metal ions concentration of 0.34 ppm at the condition of  $CH_4/H_2 = 1:0$ , 12 h. Corrosion potential reaches a maximum of about 0.15 V at the condition of  $CH_4/H_2 = 1:0$ , 12 h, which is significantly greater than the bare of about  $-0.34$  V. The higher corrosion potential usually implies the better corrosion resistance because of the higher

electrochemical stability. The corrosion current density is reduced to a minimum of 0.23  $\mu\text{A}/\text{cm}^2$  at  $\text{CH}_4/\text{H}_2 = 1:0$ , 12 h compared with the bare of about 1.8  $\mu\text{A}/\text{cm}^2$ . All the corrosion current density of DLC films meet the DOE's 2020 target of 1  $\mu\text{A}/\text{cm}^2$ . A smaller current density means a lower corrosion rate.

## References

- [1] W. Ding, Y. Guo, D. Ju, S. Sato, and T. Tsunoda, "The effect of CH<sub>4</sub>/H<sub>2</sub> ratio on the surface properties of HDPE treated by CH<sub>x</sub> ion beam bombardment," *Modern Physics Letters B*, vol. 30, no. 17, p. 1650214, 2016.
- [2] J. Liang, M. Chen, W. Tsai, S. Lee, and C. Ai, "Characteristics of diamond-like carbon film synthesized on AISI 304 austenite stainless steel using plasma immersion ion implantation and deposition," *Nuclear Instruments and Methods in Physics Research Section B: Beam Interactions with Materials and Atoms*, vol. 257, no. 1-2, pp. 696-701, 2007.
- [3] P. Sioshansi and E. J. Tobin, "Surface treatment of biomaterials by ion beam processes," *Surface and coatings Technology*, vol. 83, no. 1-3, pp. 175-182, 1996.
- [4] J. Ortiz-Medina *et al.*, "Nanostructured carbon-based membranes: Nitrogen doping effects on reverse osmosis performance," *NPG Asia Materials*, vol. 8, no. 4, pp. e258-e258, 2016.
- [5] X. Gao *et al.*, "Changes in the composition, structure and friction property of sputtered MoS<sub>2</sub> films by LEO environment exposure," *Applied surface science*, vol. 330, pp. 30-38, 2015.
- [6] N. Sharma *et al.*, "Effect of CH<sub>4</sub>/H<sub>2</sub> plasma ratio on ultra-low friction of nano-crystalline diamond coating deposited by MPECVD technique," *Tribology international*, vol. 44, no. 9, pp. 980-986, 2011.
- [7] J. Martí-González and E. Bertran, "Mechanical and surface characterization of diamond-like carbon coatings onto polymeric substrate," *arXiv preprint arXiv:1509.08512*, 2015.
- [8] J. Xu *et al.*, "Corrosion behavior of a ZrCN coated Ti alloy with potential application as a bipolar plate for proton exchange membrane fuel cell," *Journal of Alloys and Compounds*, vol. 663, pp. 718-730, 2016.
- [9] T. Santra, T. Bhattacharyya, P. Patel, F. Tseng, and T. Barik, "Diamond, diamond-like carbon (DLC) and diamond-like nanocomposite (DLN) thin films for MEMS applications," in *Microelectromechanical Systems and Devices: InTech*, 2012.
- [10] A. C. Ferrari *et al.*, "Raman spectrum of graphene and graphene layers," *Physical review letters*, vol. 97, no. 18, p. 187401, 2006.
- [11] N. Dwivedi *et al.*, "Probing the role of an atomically thin SiN<sub>x</sub> interlayer on the structure of ultrathin carbon films," *Scientific reports*, vol. 4, no. 1, pp. 1-10, 2014.
- [12] C. Casiraghi, A. Ferrari, and J. Robertson, "Raman spectroscopy of hydrogenated amorphous carbons," *Physical Review B*, vol. 72, no. 8, p. 085401, 2005.

- [13] B. Ghosh, F. Guzmán-Olivos, and R. Espinoza-González, "Plasmon-enhanced optical absorption with graded bandgap in diamond-like carbon (DLC) films," *Journal of materials science*, vol. 52, no. 1, pp. 218-228, 2017.
- [14] Y. J. Jo, T. F. Zhang, M. J. Son, and K. H. Kim, "Synthesis and electrochemical properties of Ti-doped DLC films by a hybrid PVD/PECVD process," *Applied Surface Science*, vol. 433, pp. 1184-1191, 2018.
- [15] W. Meng and B. Gillispie, "Mechanical properties of Ti-containing and W-containing diamond-like carbon coatings," *Journal of applied physics*, vol. 84, no. 8, pp. 4314-4321, 1998.
- [16] T. Guo, C. Kong, X. Li, P. Guo, Z. Wang, and A. Wang, "Microstructure and mechanical properties of Ti/Al co-doped DLC films: Dependence on sputtering current, source gas, and substrate bias," *Applied Surface Science*, vol. 410, pp. 51-59, 2017.
- [17] M. Magnuson, E. Lewin, L. Hultman, and U. Jansson, "Electronic structure and chemical bonding of nanocrystalline-TiC/amorphous-C nanocomposites," *Physical Review B*, vol. 80, no. 23, p. 235108, 2009.
- [18] M. Yoshida, T. Tanaka, S. Watanabe, M. Shinohara, J.-W. Lee, and T. Takagi, "Improvement of oxygen barrier of PET film with diamond-like carbon film by plasma-source ion implantation," *Surface and Coatings Technology*, vol. 174, pp. 1033-1037, 2003.
- [19] N. Huang, H. Yu, L. Xu, S. Zhan, M. Sun, and D. W. Kirk, "Corrosion kinetics of 316L stainless steel bipolar plate with chromiumcarbide coating in simulated PEMFC cathodic environment," *Results in physics*, vol. 6, pp. 730-736, 2016.
- [20] K. Furlan, A. Klein, and D. Hotza, "Diamond-like carbon films deposited by hydrocarbon plasma sources," *Rev. Adv. Mater. Sci*, vol. 34, pp. 165-172, 2013.
- [21] M. Hiratsuka and A. Tanaka, "Coating Technology of High-Performance DLC Films and Industrial Application (Japanese Title: 高機能 DLC 膜コーティング技術と応用展開)," *Journal of the Vacuum Society of Japan*, vol. 58, pp. 215-220, 2015.
- [22] M. Yoshida, T. Tanaka, S. Watanabe, M. Shinohara, J.-W. Lee, and T. Takagi, "Improvement of oxygen barrier of PET film with diamond-like carbon film by plasma-source ion implantation," *Surface and Coatings Technology*, vol. 174, pp. 1033-1037, 2003.
- [23] H. Zhang *et al.*, "Performance of Ti–Ag-deposited titanium bipolar plates in simulated unitized regenerative fuel cell (URFC) environment," *international journal of hydrogen energy*, vol. 36, no. 9, pp. 5695-5701, 2011.

- [24] M. Kumagai, S.-T. Myung, S. Kuwata, R. Asaishi, Y. Katada, and H. Yashiro, "Application of Ni-free high nitrogen stainless steel for bipolar plates of proton exchange membrane fuel cells," *Electrochimica Acta*, vol. 54, no. 3, pp. 1127-1133, 2009.
- [25] T. Fukutsuka, T. Yamaguchi, S.-I. Miyano, Y. Matsuo, Y. Sugie, and Z. Ogumi, "Carbon-coated stainless steel as PEFC bipolar plate material," *Journal of Power Sources*, vol. 174, no. 1, pp. 199-205, 2007.
- [26] N. Huang, H. Yu, L. Xu, S. Zhan, M. Sun, and D. W. Kirk, "Corrosion kinetics of 316L stainless steel bipolar plate with chromiumcarbide coating in simulated PEMFC cathodic environment," *Results in physics*, vol. 6, pp. 730-736, 2016.



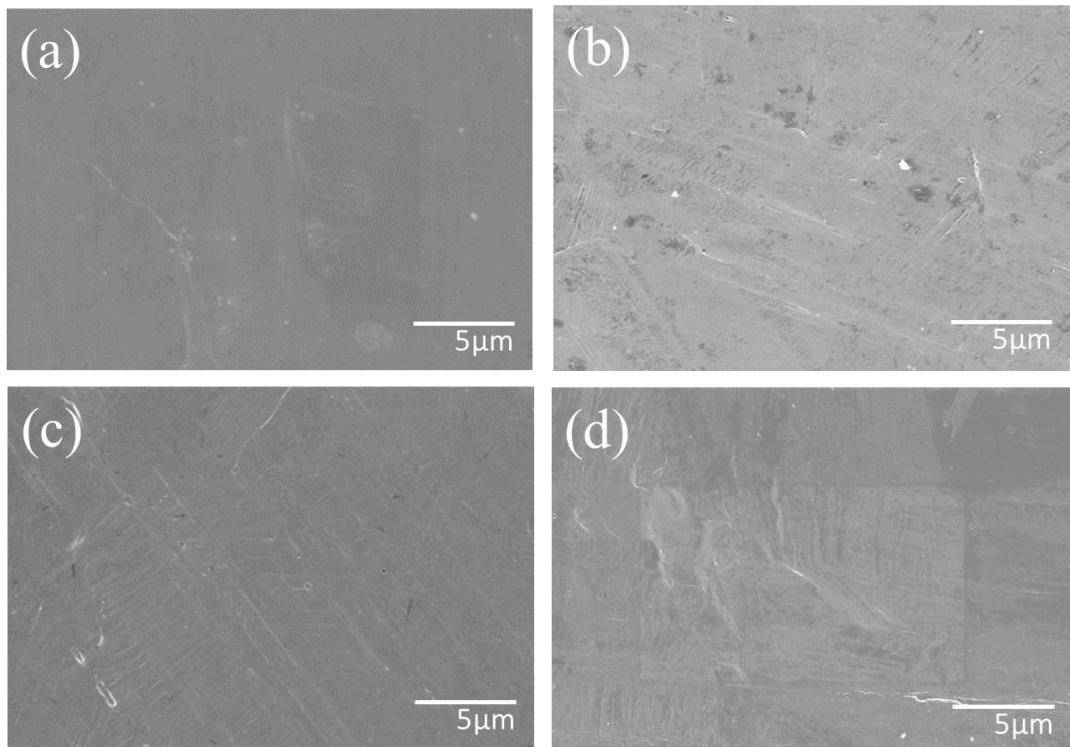
# Chapter 5 Chemical composition and corrosion behavior of DLC films-coated stainless steel

## 5.1 Surface and cross-section morphology of DLC films

### deposited on SUS316L

#### 5.1.1 Surface morphology and roughness

The surface morphology of the DLC films were observed using a scanning electron microscope. The surface morphology images of SUS316L (a); and the DLC films deposited at (b) gas ratios  $\text{CH}_4/\text{H}_2 = 1:1$ , 6hrs; (c) gas ratios  $\text{CH}_4/\text{H}_2 = 1:1$ , 12hrs; (d) gas ratios  $\text{CH}_4/\text{H}_2 = 1:0$ , 6hrs; (e) gas ratios  $\text{CH}_4/\text{H}_2 = 1:0$ , 12hrs are presented in Fig. 5-1.



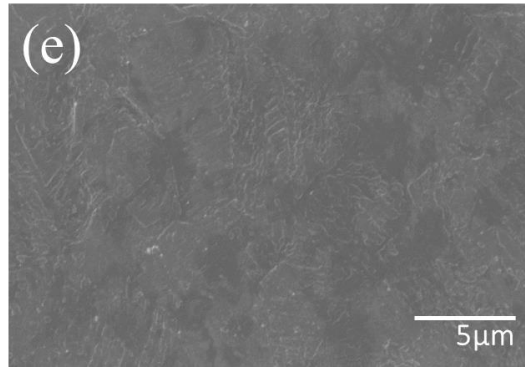
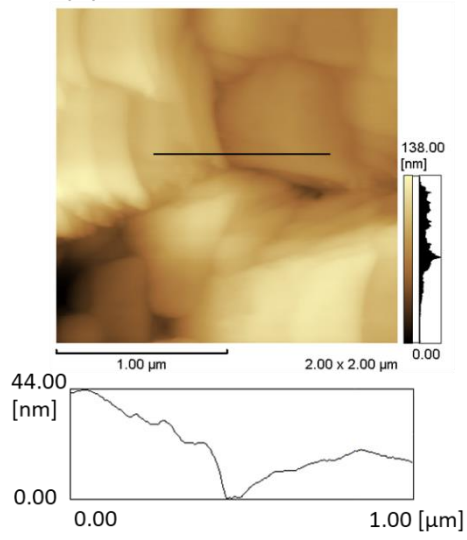


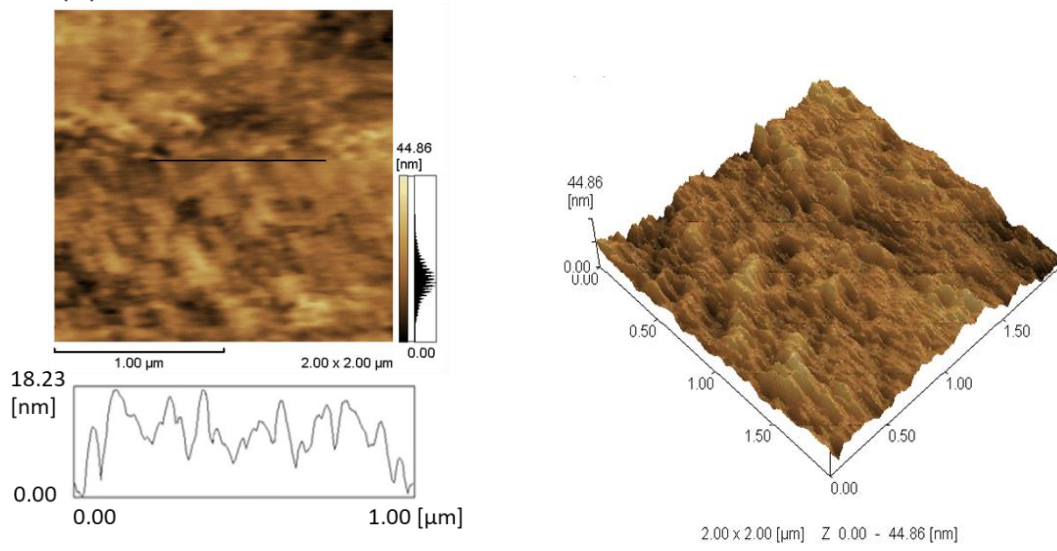
**Fig.5- 8** SEM image of SUS316L substrate (a); and the DLC film deposited at gas ratios  $\text{CH}_4/\text{H}_2 = 1:1$ , 6hrs (b); gas ratios  $\text{CH}_4/\text{H}_2 = 1:1$ , 12hrs (c); gas ratios  $\text{CH}_4/\text{H}_2 = 1:0$ , 6hrs (d); gas ratios  $\text{CH}_4/\text{H}_2 = 1:0$ , 12hrs (e).

The AFM measurements are carried out for uncoated SUS316L (a) and DLC films deposited at (b)  $\text{CH}_4/\text{H}_2 = 1:1$ , 12 h; (c)  $\text{CH}_4/\text{H}_2 = 1:1$ , 6 h; (d)  $\text{CH}_4/\text{H}_2 = 1:0$ , 12 h; (e)  $\text{CH}_4/\text{H}_2 = 1:0$ , 6 h as shown in Figure 5-2. From these figures, it can be seen that the undulating hills with a height of about 138.00 nm, 44.86 nm, 67.95 nm, 39.97 nm and 65.51 nm appear on the surface of bare and DLC films respectively. The Ra roughness of uncoated SUS316L and the DLC films-coated SUS316L is 21.80 nm, 3.77 nm, 5.63 nm, 3.93 nm and 7.56 nm respectively. The surface of DLC film deposited at 12 h becomes more flattened than that of DLC film deposited at 6 h. This can be explained by considering that the deposition process prevails on the etching phenomena: the high-energy ion beams continuously bombard the surface with the increase of time, etching away the interfacial and unstable carbon atoms belonging to the still un-relaxed domains [1, 2].

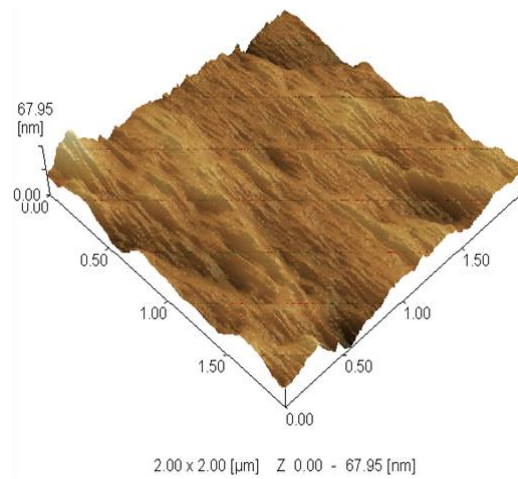
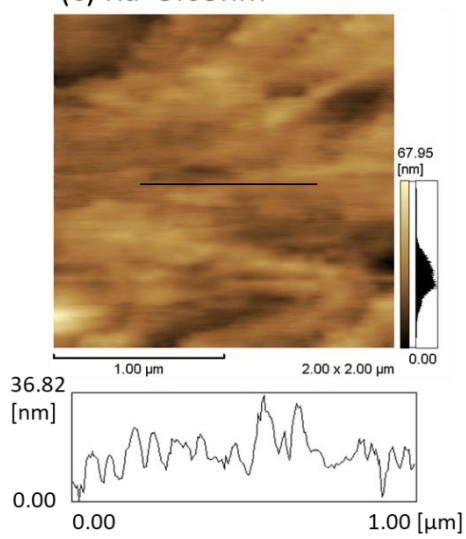
(a) Ra=21.80nm



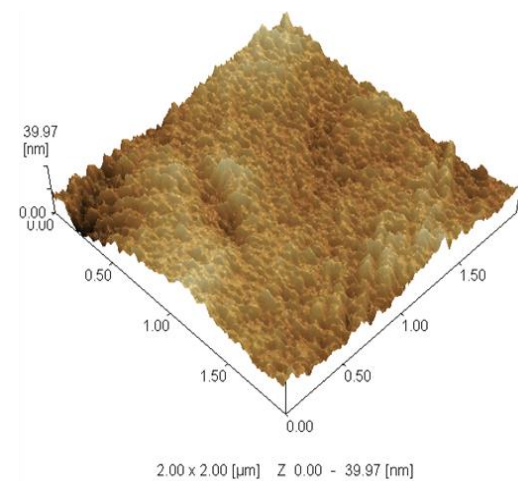
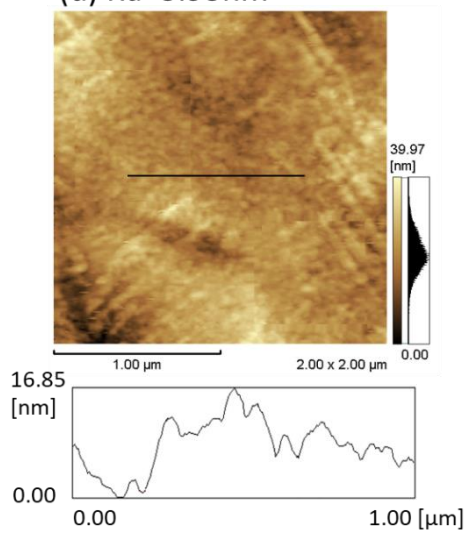
(b) Ra=3.77nm



(c) Ra=5.63nm



(d) Ra=3.93nm



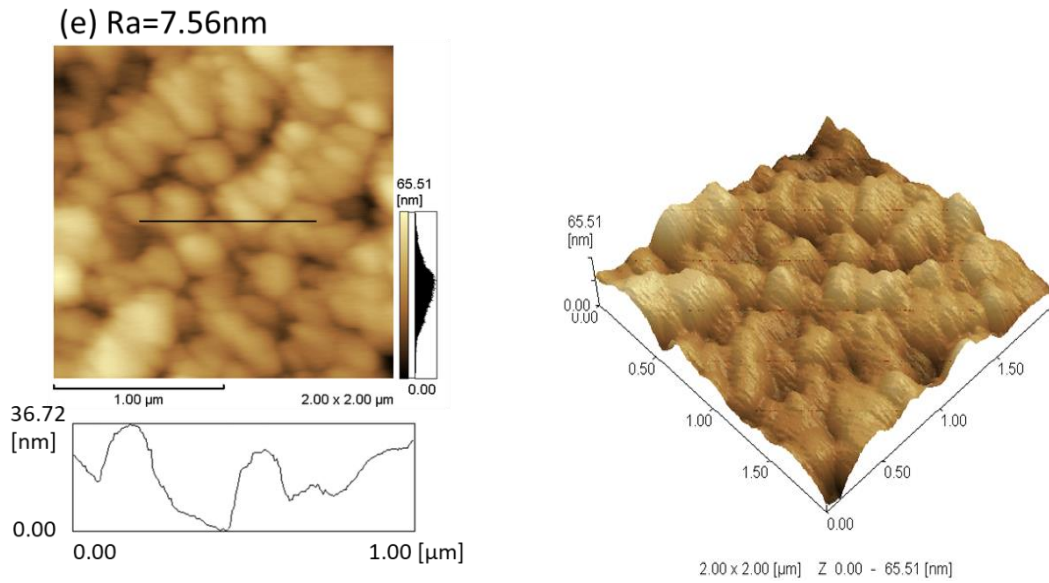


**Fig.5- 9** AFM images and linear Z-axis scale bars of uncoated SUS316L (a) and DLC coatings deposited at (b)  $\text{CH}_4/\text{H}_2 = 1:1$ , 12 h; (c)  $\text{CH}_4/\text{H}_2 = 1:1$ , 6 h; (d)  $\text{CH}_4/\text{H}_2 = 1:0$ , 12 h; (e)  $\text{CH}_4/\text{H}_2 = 1:0$ , 6 h.

### 5.1.2 Cross-sectional morphology and thickness

The cross-section morphology of the DLC films were observed using a scanning electron microscope. The cross-section morphology images of SUS316L (a) and the DLC films deposited at (b)  $\text{CH}_4/\text{H}_2 = 1:1$ , 6hrs; (c)  $\text{CH}_4/\text{H}_2 = 1:1$ , 12hrs; (d)  $\text{CH}_4/\text{H}_2 = 1:0$ , 6hrs; (e)  $\text{CH}_4/\text{H}_2 = 1:0$ , 12hrs are presented in Fig. 5-3. The DLC films on the surface are very dense. The thickness of the fully dense coating cannot be clearly defined because of the permeation layer. The DLC layer has a maximum thickness of the fully dense coating of about 569.8 nm from the Figure 5-3c. The average thickness of the fully dense coating is about 543.4 nm, 407.6 nm and 543.3 nm respectively from the Figure 5-3b, d, e. The thickness of the DLC film deposited on stainless steel substrate at the condition of gas ratios  $\text{CH}_4/\text{H}_2 = 1:0$  is thinner than at the condition of gas ratios  $\text{CH}_4/\text{H}_2 = 1:1$ . With the increase of time, the high-energy ion beams continuously bombard the growing film, the

surface desorption process plays a dominant role. So the coating atoms are penetrated into the substrate with more energy, which reduces the thickness of the fully dense coating and increases the thickness of the permeation layer [1, 3, 4].

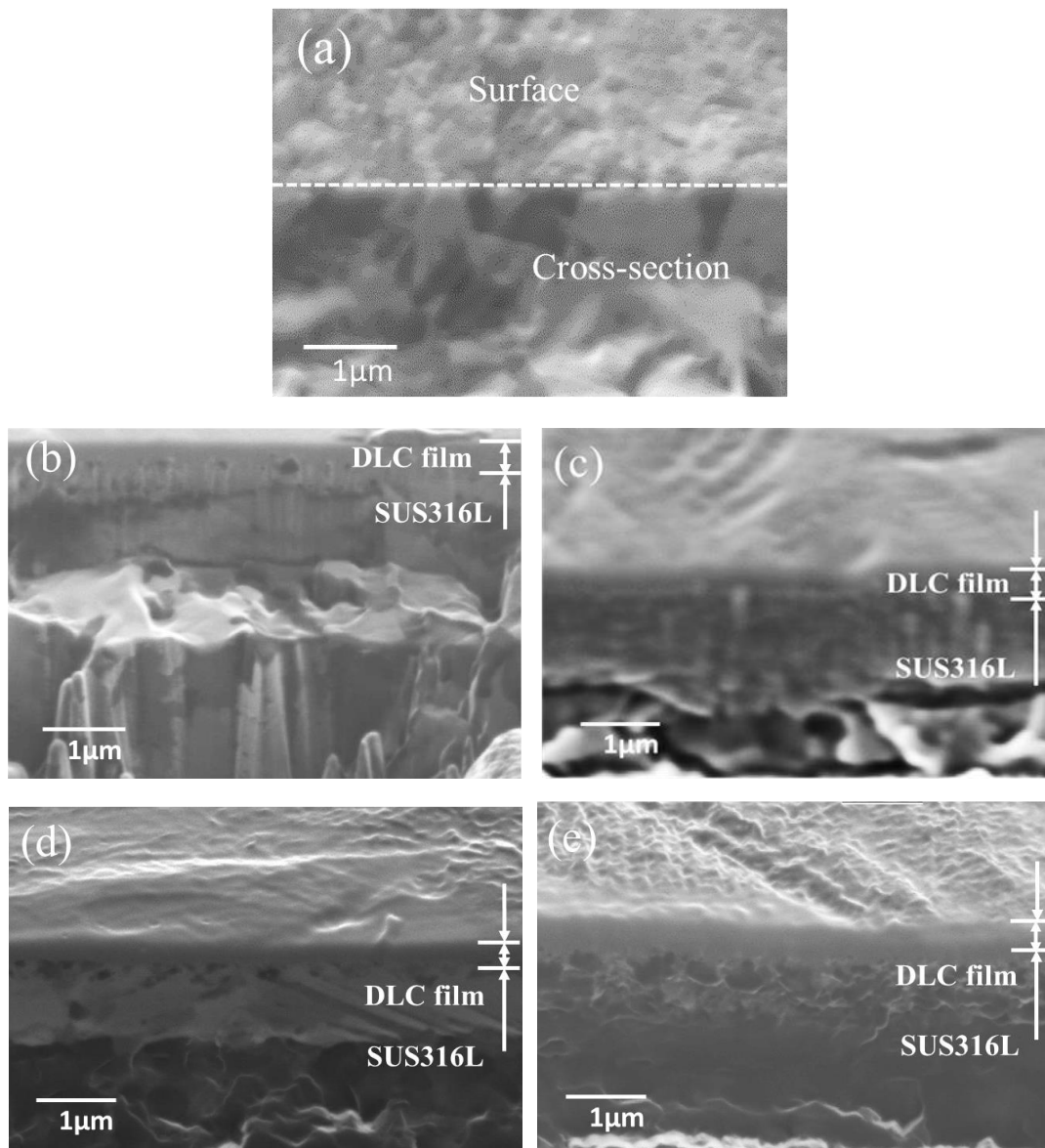
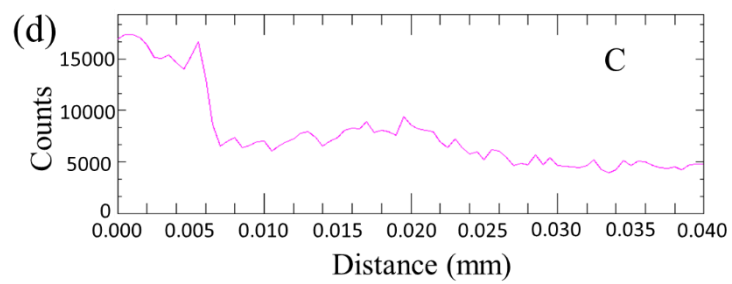
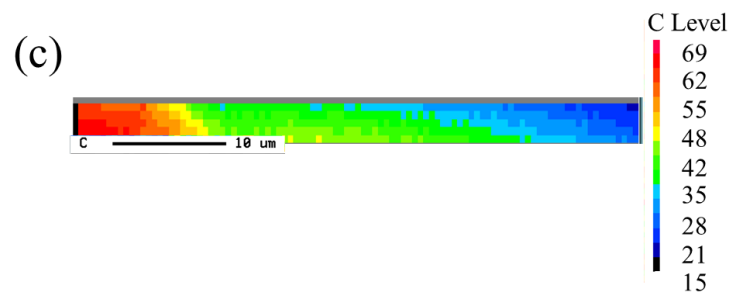
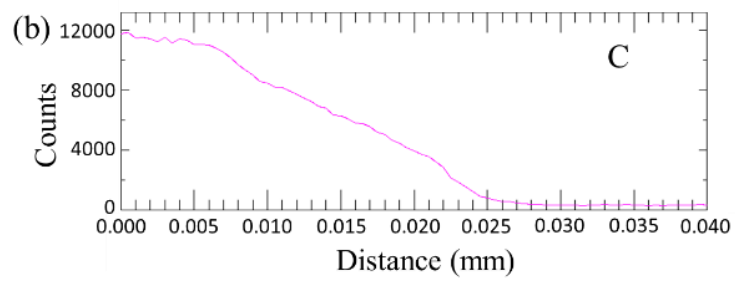
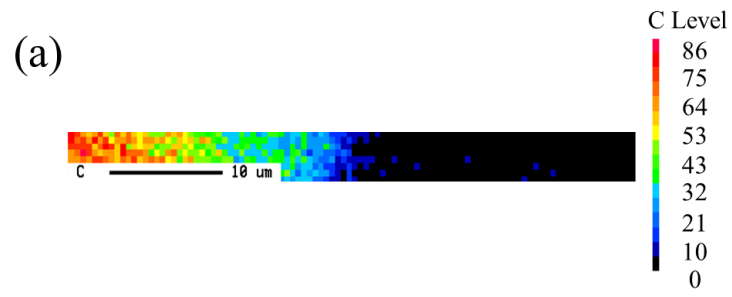


**Fig.5- 3** Cross-section SEM image of SUS316L (a) and the DLC films deposited at (b)  $\text{CH}_4/\text{H}_2 = 1:1$ , 6hrs; (c)  $\text{CH}_4/\text{H}_2 = 1:1$ , 12hrs; (d)  $\text{CH}_4/\text{H}_2 = 1:0$ , 6hrs; (e)  $\text{CH}_4/\text{H}_2 = 1:0$ , 12hrs.

**Table 5- 1** Thickness of DLC films-coated stainless steel deposited at different conditions

	$CH_4/H_2 = 1:1$	$CH_4/H_2 = 1:1$	$CH_4/H_2 = 1:0$	$CH_4/H_2 = 1:0$
	6h	12h	6h	12h
<b>Thickness(mm)</b>	543.4	569.8	407.6	543.3

The carbon element concentration distribution of DLC film-coated SUS316L were determined by EPMA. The sample to be analyzed was bombarded by an electron beam which would emit x-rays with wavelengths characteristic to specific elements. Then the concentration distribution and diffusivities of elements could be obtained accurately by EPMA mapping [5-6]. The average thickness of the carbon permeation layer is about 10  $\mu\text{m}$ , 15 $\mu\text{m}$ , 8 $\mu\text{m}$  and 9  $\mu\text{m}$  respectively from Figure 5-4 b, d, f, h. The liner scan of carbon is not significantly reduced in Figure 5-4 d, so the thickness is estimated to be 35  $\mu\text{m}$  combined with the carbon concentration distribution (Figure 5-4 c). The limited lateral resolution may also reduce the accuracy of the results. The liner scans indicate that the carbon concentration decreases with the distance. The thickness of the DLC film deposited on SUS316L substrate at the condition of gas ratio  $CH_4/H_2 = 1:1$  is thicker than that of  $CH_4/H_2 = 1:0$ . As the increase of deposition time, the penetration depth of DLC increases because of the increase in high-energy ion beam, but the intensity of carbon weakens. The coating atoms are penetrated into the substrate with more energy to reduce the thickness of the fully dense coating and increase the thickness of the permeation layer at the deposition time of 12 h.



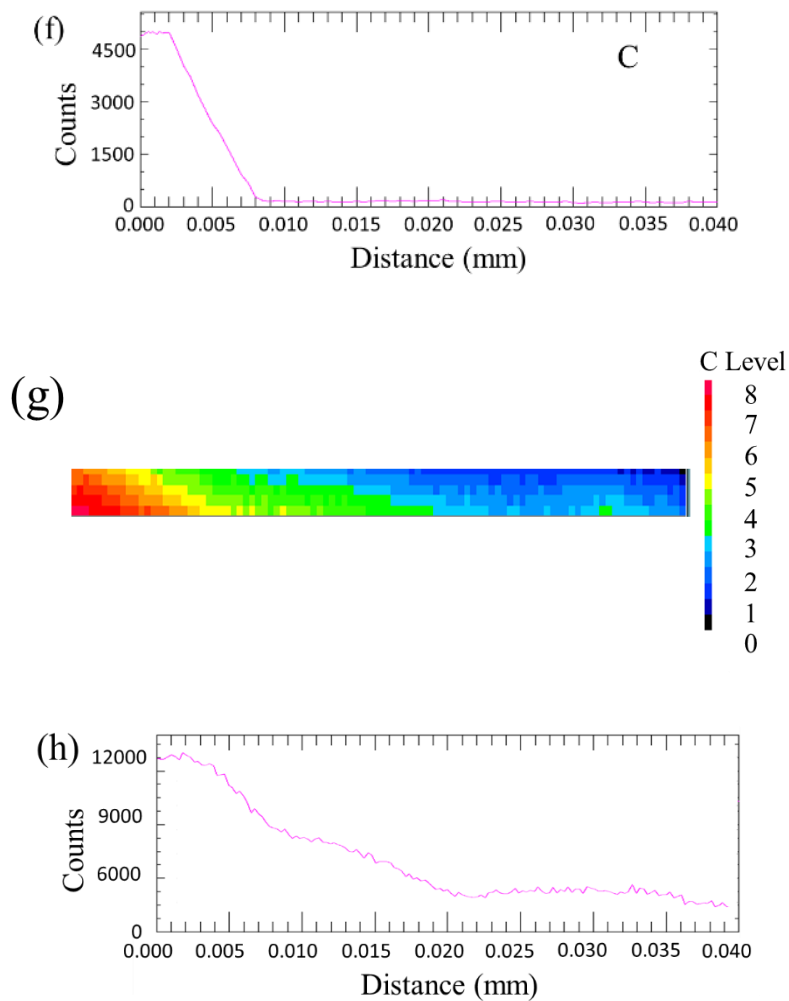


Fig.5- 4 EPMA mappings of carbon element and EPMA line scans of carbon intensity of DLC film cross-section deposited at (a) and (b)  $\text{CH}_4/\text{H}_2 = 1:1$ , 6 h; (c) and (d)  $\text{CH}_4/\text{H}_2 = 1:1$ , 12 h; (e) and (f)  $\text{CH}_4/\text{H}_2 = 1:0$ , 6 h; (g) and (h)  $\text{CH}_4/\text{H}_2 = 1:0$ , 12 h.

## 5.2 Chemical composition and microstructure analysis of DLC films deposited on SUS316L

### 5.2.1 Raman spectroscopy of DLC films on SUS316L

The position of G peak and ratio of D peak intensity to G peak intensity ( $I_D/I_G$ ) are

the important factors which fully depended on the DLC film structure [7]. In order to extract these factors, the Raman spectrum of DLC coating was decomposed to two Gaussian peaks (D-peak to G-peak). The Fig.5-5 displays the typical Raman spectrum of DLC films deposited on SUS316L. The spectra exhibited a broad asymmetric Raman scattering band in the range of 1000-2000 $\text{cm}^{-1}$ , representing typical characteristics of DLC films from the figure.

Raman features such as ID/IG ratio, D-peak and G-peak position are specifically shown in Table 5-2. The Raman shift error exists due to factors such as the pixel of detector, laser wavelength accuracy and the fitting by a Gaussian method [8]. The variation of G-peak position toward higher Raman shift shows that the chemical bonding is changed from olefinic to aromatic. The G-peak position is changed from 1558 to 1570  $\text{cm}^{-1}$  by decreasing the  $\text{CH}_4$  ratio and the deposited time for SUS316L substrate. Moreover, the decreased ID/IG shows an increase in size and number of clusters, a decrease in chain-like structures [3, 9]. ID/IG ratio of DLC film deposited on SUS316L at gas ratios  $\text{CH}_4/\text{H}_2 = 1:1$ , 6 h is 1.03, meanwhile ID/IG of DLC coating deposited at gas ratios  $\text{CH}_4/\text{H}_2 = 1:0$ , 6 h is 1.21. Meanwhile, the G-peak position is shifted from 1558.45 to 1568.85  $\text{cm}^{-1}$  indicating the increase in  $\text{sp}^2$ -C content. In a-C:H coating, a decrease in ID/IG corresponds to a decrease in  $\text{sp}^2/\text{sp}^3$ . Therefore, DLC film deposited at  $\text{CH}_4/\text{H}_2 = 1:1$ , 6 h has a higher  $\text{sp}^3$  content with a diamond-like tetrahedral structure which leads to a better anti-corrosion resistance [10].

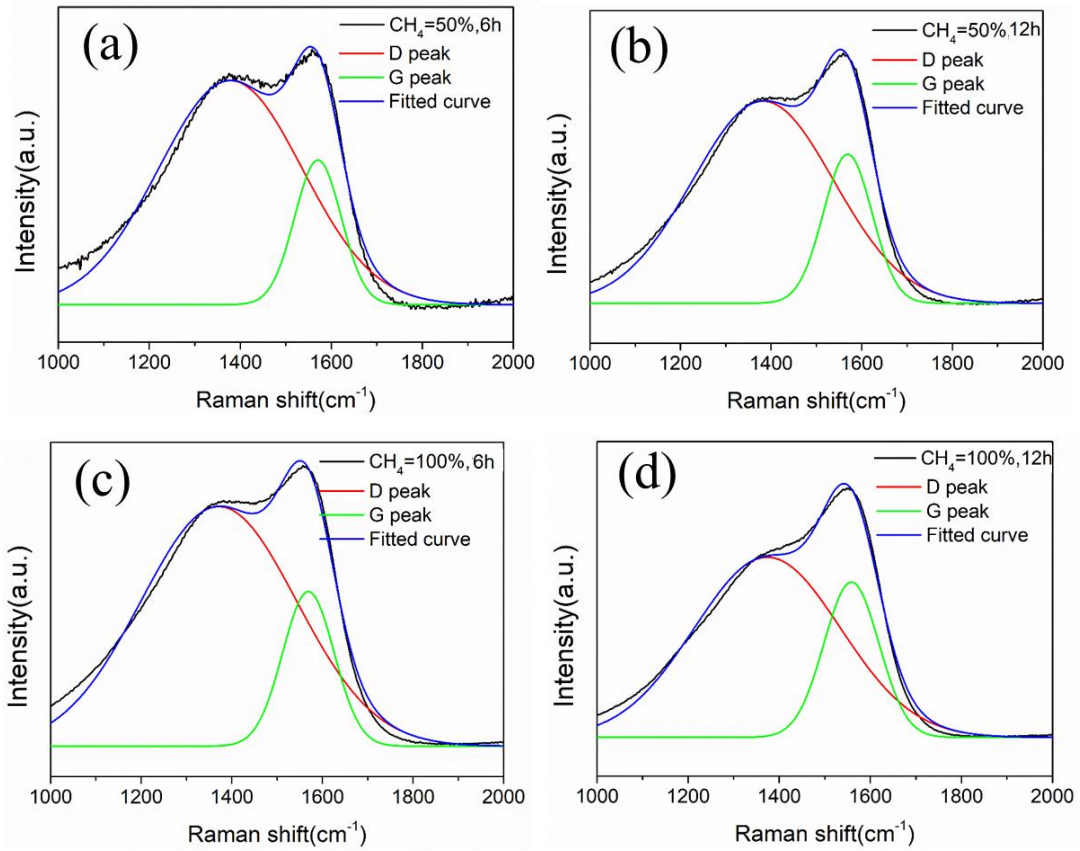


**Fig.5- 5** Typical Raman spectrum of DLC films deposited on SUS316L at (a)  $CH_4/H_2 = 1:1$ , 6hrs; (b)  $CH_4/H_2 = 1:1$ , 12hrs; (c)  $CH_4/H_2 = 1:0$ , 6hrs; (d)  $CH_4/H_2 = 1:0$ , 12hrs.

**Table 5- 2**  $I_D/I_G$  ratio, D peak and G peak position of DLC films deposited on SUS316L at different conditions

<i>SUS316L</i>	$CH_4/H_2 = 1:1, 12h$	$CH_4/H_2 = 1:1, 6h$	$CH_4/H_2 = 1:0, 12h$	$CH_4/H_2 = 1:0, 6h$
$I_D/I_G$	1.03	1.30	1.21	1.31
<i>G-peak</i> ( $cm^{-1}$ )	1558.45	1568.91	1568.85	1570.53
<i>D-peak</i> ( $cm^{-1}$ )	1373.99	1382.35	1371.20	1378.31

### 5.2.2 TEM analysis of DLC films on SUS316L

The microstructure of the DLC film-coated SUS316L was analyzed by TEM. Before the experiment of TEM, the sample with the thickness of about 0.1 $\mu\text{m}$  for investigation was prepared by FIB-SEM as before. The SEM image was shown in Fig.5-6.

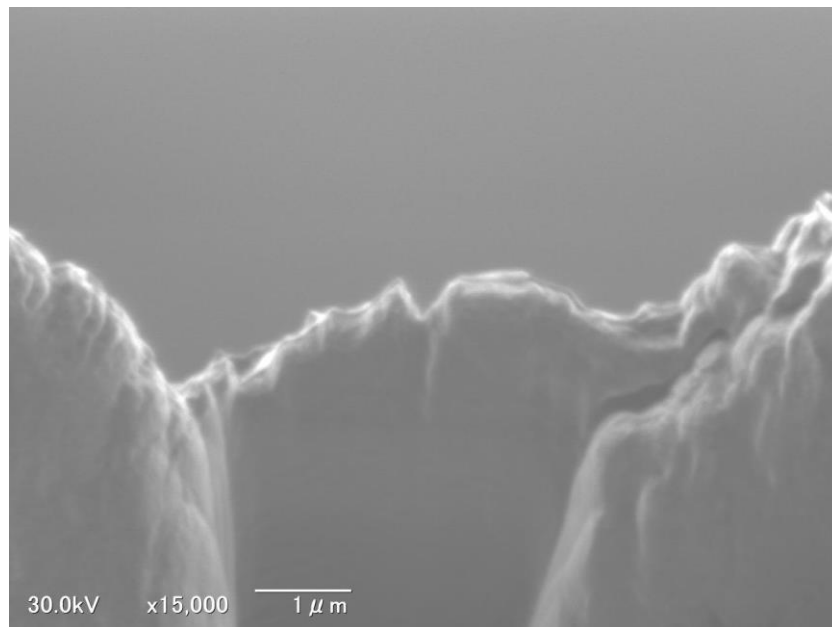


**Fig.5-6** SEM image of the DLC film deposited on SUS316L after FIB process.

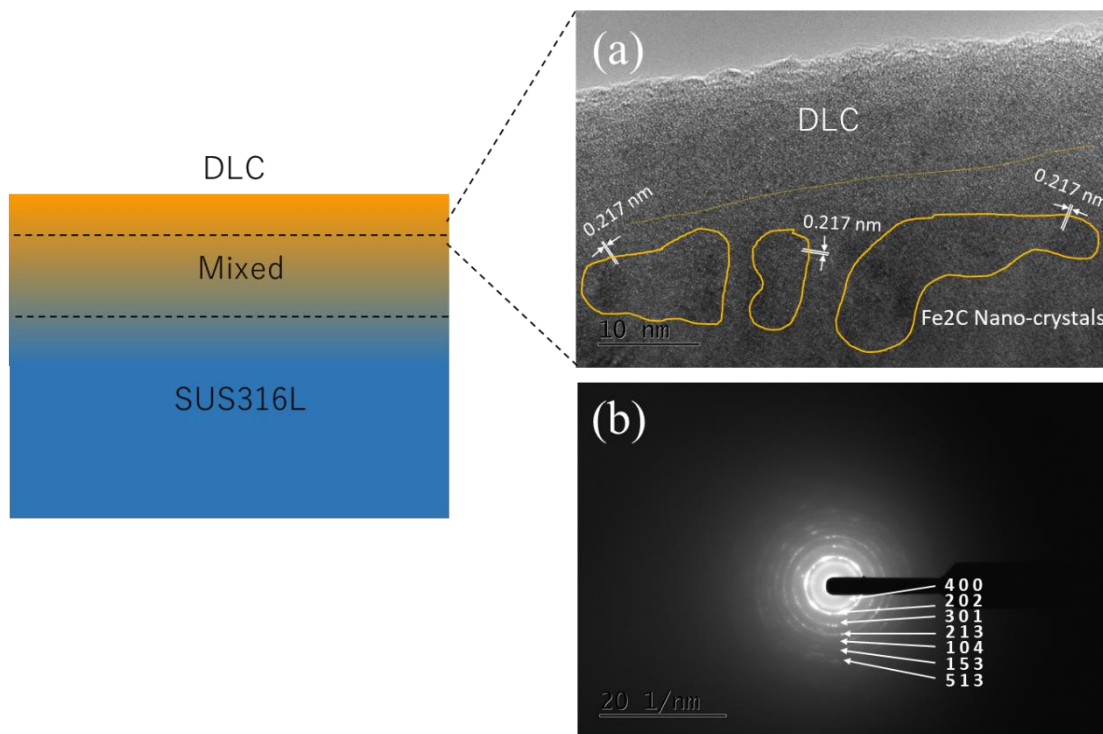


**Fig.5- 7** Schematic diagram TEM images of the DLC film deposited on SUS316L at  $\text{CH}_4/\text{H}_2 = 1:1$

The schematic diagram and TEM images of DLC film deposited on SUS316L at  $\text{CH}_4/\text{H}_2 = 1:1$  were shown in figure 5-7. The penetration section from pure DLC film to SUS316L substrate could be easily seen from figure 5-7(a). The selected area electron diffraction pattern (SAED) of nanocrystalline phase was shown in figure 5-7(b). A small amount of nanocrystalline phase marked with yellow circle was surrounded by an amorphous matrix. The interplanar spacing was calculated according to the results of calculation based on the diffraction images. The  $d$  values is 0.217 nm which agrees well with the  $\text{Fe}_2\text{C}$  lattice constant. Polycrystalline rings indexable to the (400), (202), (301), (213), (104), (153) and (513) reflections of  $\text{Fe}_2\text{C}$  were present.

### 5.2.3 XPS analysis of DLC films on SUS316L

The bonding structure of DLC films deposited at different conditions were evaluated by XPS spectroscopy. In order to give a trustful result, the metallic oxide contaminations from the environment was removed by Ar<sup>+</sup> bombardment [11]. After removing the contaminations, C1s XPS spectrum scan of DLC films deposited on the SUS 316L are shown in the Figure 5-8. It can be seen that the main bond on the surface of the DLC film are sp<sup>2</sup>-C, sp<sup>3</sup>-C, c=O and c-c, and their binding energies are about 284.58 eV, 286 eV, 288.4~288.5 eV and 293.5 eV, respectively [12, 13]. The surface oxide film on SUS316L having a thickness of 2-4 nm means a very small oxygen content. The DLC film may contain oxygen content and not just from oxidation in the air. The oxygen atomic concentration of DLC films deposited at CH<sub>4</sub> = 1:1, 12 h; CH<sub>4</sub>/H<sub>2</sub> = 1:1, 6 h; CH<sub>4</sub>/H<sub>2</sub> = 1:0, 12 h and CH<sub>4</sub>/H<sub>2</sub> = 1:0, 6 h is about 21.59%, 17.92%, 27.77% and 21.84% respectively. No obvious peaks of Fe, Cr and Ni elements were observed in the spectra, which means no matrix elements exist in the surface composition of the DLC film, indicating that during the film deposition process, the density and energy of bombardment ions are high, and the substrate can be fully impacted. With the increase of time, the high-energy ion beams continuously bombard the growing film, causing the sp<sup>3</sup>-C to break down into the stable two-dimensional sp<sup>2</sup>-C structure. The binding energy of 293.5 eV indicates the peak of the transition to the sigma- orbitals [14].

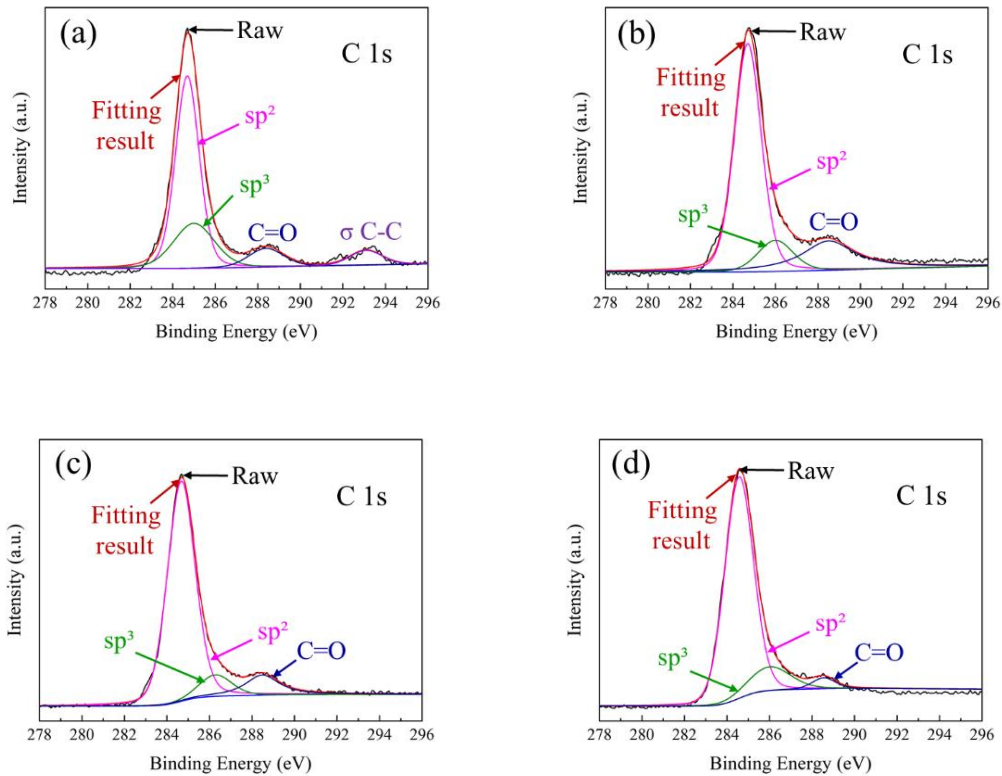


**Fig.5-8** XPS spectra for C 1s of DLC films deposited on SUS316L at (a)  $\text{CH}_4/\text{H}_2 = 1:1$ , 12hrs; (b)  $\text{CH}_4/\text{H}_2 = 1:1$ , 6hrs; (c)  $\text{CH}_4/\text{H}_2 = 1:0$ , 12hrs; (d)  $\text{CH}_4/\text{H}_2 = 1:0$ , 6hrs.

### 5.3 Interfacial Contact Resistance of DLC films deposited on SUS316L

The low ICR is the key factor to obtain high performance for metallic bipolar plates of PEMFCs. The ICR of SUS316L substrate and DLC films at  $150 \text{ N/cm}^2$  are shown in Table 5-3. The ICR is obtained by subtracting the resistance of the substrate from the resistance of DLC Films-Coated SUS316L [15-16]. The good conductive performance depends on high content of  $\text{sp}^2$ -C bonds. Since the DLC film penetrates into the substrate from EPMA results, the increase of ICR under the condition of  $\text{CH}_4/\text{H}_2 = 1:0$  may be due to an increase of  $\text{sp}^3$ -C content in the permeation layer. It results that ICR is not in good agreement with

the  $sp^2/sp^3$  ration mentioned above. Therefore, the DLC film-coated SUS316L at  $CH_4/H_2 = 1:1$  is available for fuel cells. Nevertheless, the DLC films deposited at  $CH_4/H_2 = 1:1$ , 12 h showed lowest resistance of  $12.9 \text{ m}\Omega\cdot\text{cm}^2$  which is still slightly higher than the Department of Energy's (DOE) target (2020) of  $10 \text{ m}\Omega\cdot\text{cm}^2$  [17].

**Table 5- 3** ICR of DLC-coated SUS316L

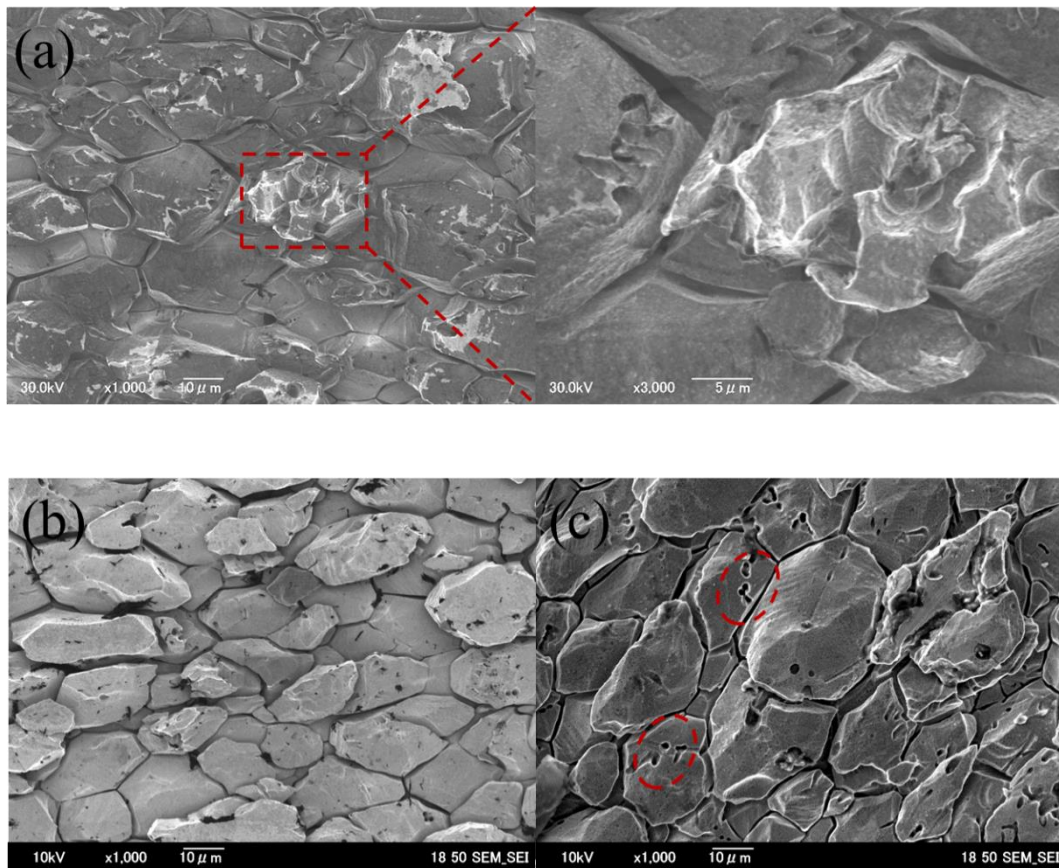
	<i>SUS316L</i>	<i>CH<sub>4</sub>/H<sub>2</sub> =1:1</i>	<i>CH<sub>4</sub>/H<sub>2</sub> =1:1</i>	<i>CH<sub>4</sub>/H<sub>2</sub> =1:1</i>	<i>CH<sub>4</sub>/H<sub>2</sub> =1:0</i>
	<i>substrate</i>	<i>6h</i>	<i>12h</i>	<i>6h</i>	<i>12h</i>
<b><i>ICR (mΩ·cm<sup>2</sup>)</i></b>	35	23.7	12.9	105.6	79.9

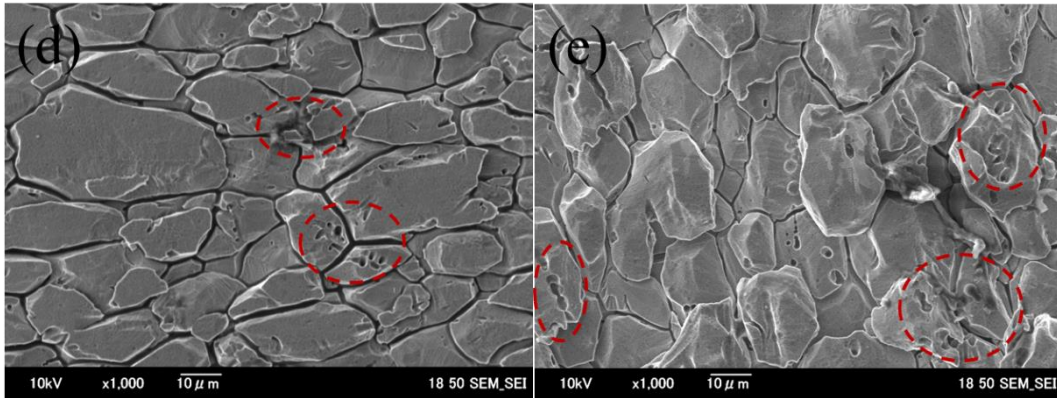
## 5.4 Corrosion behavior of DLC films-coated SUS316L

### 5.4.1 Surface characteristics of DLC films-coated SUS316L after corrosion

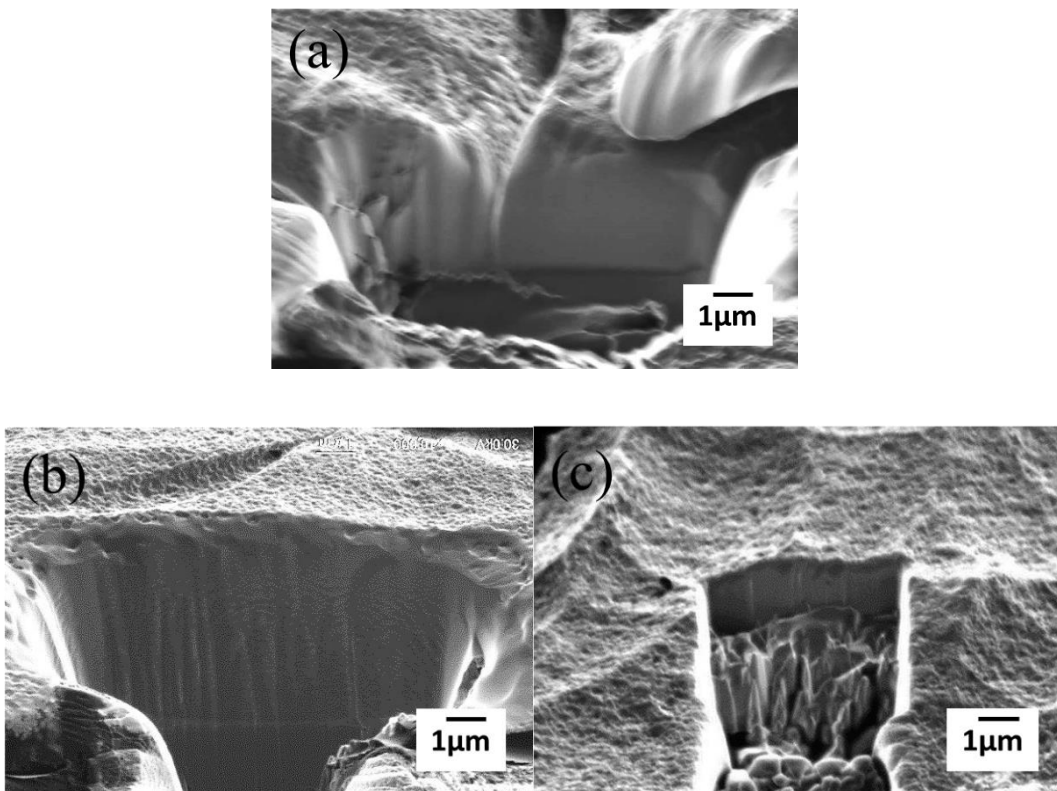
The surface morphology images of SUS316L (a); and the DLC films deposited at (b) gas ratios  $CH_4/H_2 = 1:1$ , 12hrs; (c) gas ratios  $CH_4/H_2 = 1:1$ , 6hrs; (d) gas ratios  $CH_4/H_2 = 1:0$ , 12hrs; (e) gas ratios  $CH_4/H_2 = 1:0$ , 6hrs after corrosion test are presented in Fig. 5-9. The cross-section morphology SEM images of SUS316L and different DLC coatings are presented in Figure 5-3. DLC films are still found on the surface of the substrates and the thickness of the DLC film is thinner than before from these pictures. It is observed that the DLC films are destroyed in corrosion test, and some cracks appear on the surface. The surface morphology is changed and some larger corrosion pits are observed on the surface at condition of  $CH_4/H_2 = 1:0$ , 12 h than that of  $CH_4/H_2 = 1:1$ , 12 h. The pitting corrosion regions are marked with red circles as shown in Figure 5-9. SUS316L

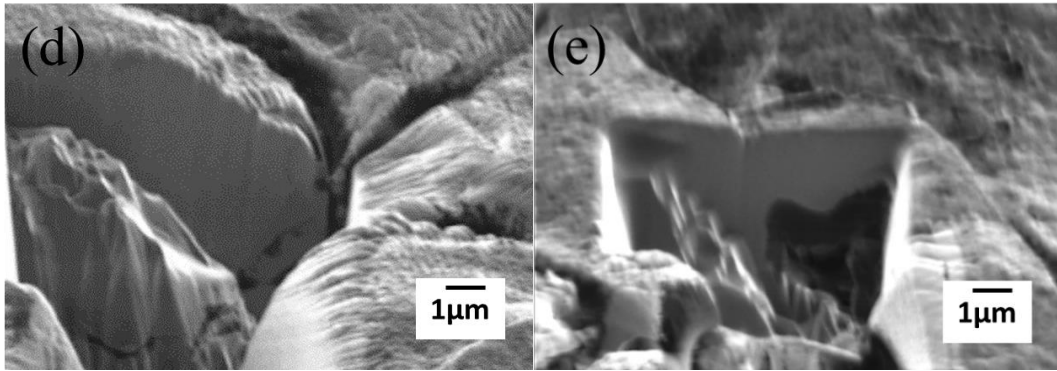
constituents like Fe, Cr and Ni are stable in elemental form below  $-0.7$  V vs. SCE. In the fuel cell operating conditions, SUS316L constituents are stable in the form of  $\text{Fe}^{2+}$ ,  $\text{Fe}^{3+}$ ,  $\text{Ni}^{2+}$  and  $\text{Cr}^{3+}$  oxidized states [18]. In the corrosion test of high temperature acidic solution of 168 hours, a small amount of acidic solution penetrates into the film and contacts with SUS316L. Then the oxide is generated between the substrate and the film, causing the DLC film to rupture and forming pitting corrosion. For the DLC films coated on the SUS316L substrate, a local region is suffered from accelerated corrosion due to the pits.





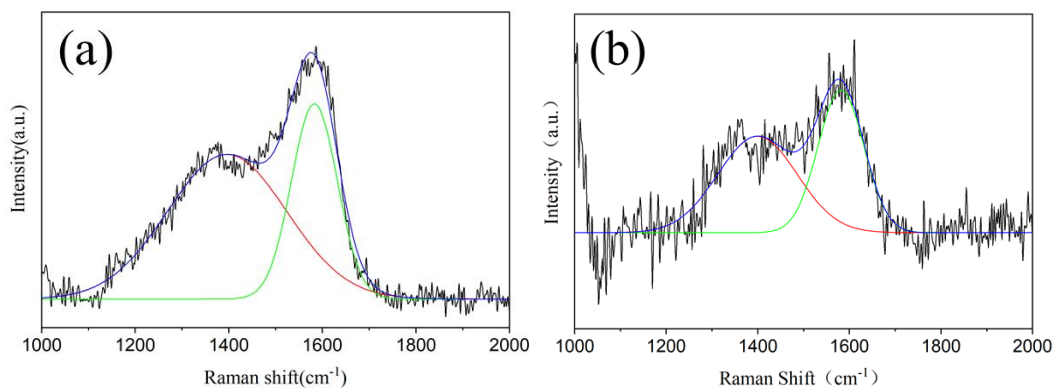
**Fig.5- 9** SEM images of SUS316L substrate (a); and the DLC film deposited at gas ratios  $\text{CH}_4/\text{H}_2 = 1:1$ , 6hrs (b); gas ratios  $\text{CH}_4/\text{H}_2 = 1:1$ , 12hrs (c); gas ratios  $\text{CH}_4/\text{H}_2 = 1:0$ , 6hrs (d); gas ratios  $\text{CH}_4/\text{H}_2 = 1:0$ , 12hrs (e) after corrosion test.





**Fig.5- 10** Cross-section SEM images of SUS316L (a); and the DLC films deposited at (b)  $\text{CH}_4/\text{H}_2 = 1:1$ , 12hrs; (c)  $\text{CH}_4/\text{H}_2 = 1:1$ , 6hrs; (d)  $\text{CH}_4/\text{H}_2 = 1:0$ , 12hrs; (e)  $\text{CH}_4/\text{H}_2 = 1:0$ , 6hrs after corrosion test.

The Chemical bonding structure of DLC films-coated SUS316L after corrosion test are analyzed. Figure 5-11 displays the typical Raman spectrum of DLC films deposited on SUS316L after corrosion test. The Raman spectra can be fitted by the two Gaussian peaks. The G-peak intensity of the DLC film at the condition of  $\text{CH}_4/\text{H}_2 = 1:0$ , 12 h is weaker than that of  $\text{CH}_4/\text{H}_2 = 1:1$ , 12 h, indicating a reduction of  $\text{sp}^3\text{-C}$  ratio. Therefore, DLC film deposited at  $\text{CH}_4/\text{H}_2 = 1:1$ , 12 h has the better corrosion resistance.



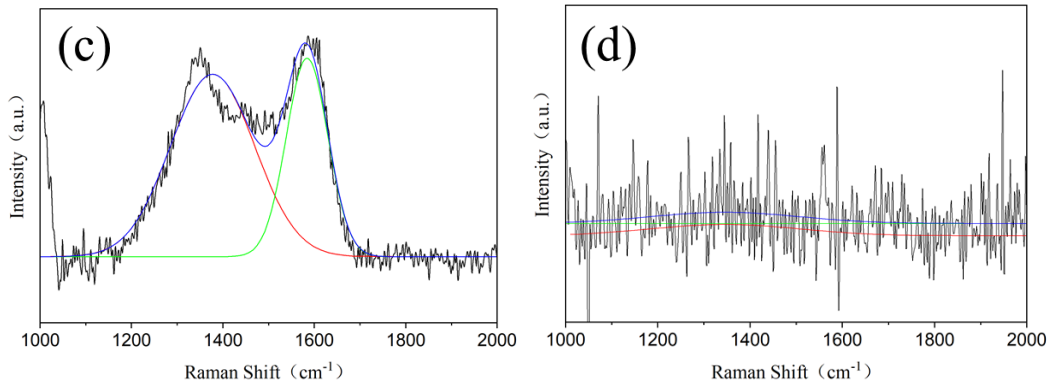


**Fig.5- 11** Typical Raman spectrum of DLC films deposited on SUS316L at (a)  $\text{CH}_4/\text{H}_2 = 1:1$ , 12hrs; (b)  $\text{CH}_4/\text{H}_2 = 1:1$ , 6hrs; (c)  $\text{CH}_4/\text{H}_2 = 1:0$ , 12hrs; (d)  $\text{CH}_4/\text{H}_2 = 1:0$ , 6hrs.

#### 5.4.2 Effect of DLC films on metal ions dissolution

Metal ions concentration in corrosion solution are important for evaluating the corrosive resistance of bipolar plate. Hence metal ions concentration for the bare and DLC films-coated SUS316L after 168 h corrosion test are summarized in Table 5-4. Compared to the metal ions concentration of uncoated substrate, the metal ions of DLC films has a significant reduction, indicating that the DLC films play an important role on protecting the substrate.

For the SUS316L stainless steel, the metal ions leached from DLC films-coated SUS316L has a significant reduction with a minimum of 16.60 ppm, indicating that the DLC films play an important role on protecting the substrate. The main reason is that there is an easily corroded place on the surface of DLC film coated on SUS316L. The pitting reaction takes place in passivation film formed on SUS316L due to the self-excited reaction and some pores are formed on the substrate [19]. In addition, there are hydrogen ions in the corrosive solution, forming a strong corrosion layer and accelerating the corrosion rate [20]. Meanwhile, intergranular corrosion cracking inside the SUS316L. All

of these have a destructive effect on the DLC film coated on the SUS316L. From Table 5-4, the DLC film deposited at the condition of  $CH_4/H_2 = 1:1$ , 12 h has a lower concentration than that of  $CH_4/H_2 = 1:0$ , 12 h. Because the DLC film deposited at  $CH_4/H_2 = 1:0$ , 12 h is relatively thin and not dense enough which can be observed from SEM and EPMA results. The higher oxygen content of DLC film deposited at  $CH_4/H_2 = 1:0$  also accelerates corrosion rate in an acidic solution. After 168 h corrosion test, part of the substrate is exposed to acid corrosion solution, which is more susceptible to corrosion. Meanwhile the corrosion behavior is consistent with the cross-section SEM images of the DLC coatings.

**Table 5- 4** Metal ions concentration for the bare and DLC films after 168 h corrosion. (ppm)

	SUS316L	$CH_4/H_2=1:1$ , 12h	$CH_4/H_2=1:1$ , 6h	$CH_4/H_2=1:0$ , 12h	$CH_4/H_2=1:0$ , 6h
316L-Fe	38.84	11.89	18.99	14.98	26.45
316L-Cr	9.28	2.86	4.51	3.22	4.55
316L-Ni	3.60	1.85	1.72	1.36	2.90
Total	51.72	16.60	25.22	19.56	33.90

#### 5.4.3 Electrochemical behaviors of DLC films deposited on SUS316L

The electrochemical behaviors of all samples were analyzed in 0.5 M sulfuric acid solution at 90 °C by conventional three-electrode system. The DLC-coated SUS316L sample was acted as working electrode respectively, a platinum sheet as counter electrode,

and a SCE as the reference electrode [21]. The polarization curves of SUS316L and DLC films-coated SUS316L in 0.5 M sulfuric acid solution purged with air at 90 °C are shown in Figure 5-12. In comparison with the bare, the DLC films-coated SUS316L exhibit a more noble corrosion potential and more stable passive region in simulated cathode condition. Corrosion potential reaches a maximum of about 0.1 V at the condition of CH<sub>4</sub>/H<sub>2</sub>= 1:1, 12 h, which is significantly greater than the bare of about -0.2 V. The higher corrosion potential usually implies the better corrosion resistance because of the higher electrochemical stability [22]. At the cathode potential of around 0.6 V under the fuel cell operating condition, the corrosion current density of the bare is about 19 μA/cm<sup>2</sup>. As for the DLC films-coated SUS316L, the corrosion current density is reduced to a minimum of 0.5 μA/cm<sup>2</sup> at CH<sub>4</sub>/H<sub>2</sub> = 1:1, 6 h and 12 h. The corrosion current density of DLC films deposited at CH<sub>4</sub>/H<sub>2</sub> = 1:1 meet the DOE's 2020 target of 1 μA/cm<sup>2</sup> (0.5 M H<sub>2</sub>SO<sub>4</sub> solution with 5 ppm HF, 70 °C) [23]. A smaller current density means a lower corrosion rate. All the DLC films-coated SUS316L exhibit the similar passivation behavior. The high active peak could be viewed because of the active dissolution and the oxidation. The passivation film formed on the surface could protect SUS316L from contacting sulfuric acid solution, so as to avoid corrosion. The DLC films deposited at CH<sub>4</sub>/H<sub>2</sub> = 1:1 have the better electrochemical behavior and higher corrosion resistance due to the intrinsic microstructure properties from the surface morphology, which are in accordance with the ICP results.

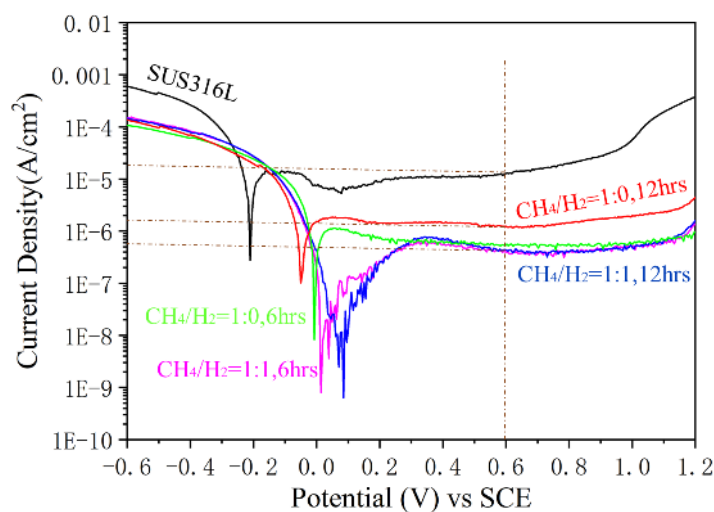


**Fig.5- 12** Potentiodynamic behaviors of uncoated SUS316L and various DLC films-coated SUS316L in 0.5 M H<sub>2</sub>SO<sub>4</sub> at 90 °C.

## 5.5 Summary

In this part, the dense and uniform DLC films as protective film were successfully deposited on SUS316L steel using IBED technique by changing the gas ratio CH<sub>4</sub>/H<sub>2</sub> and deposition time. The microstructure and corrosion properties of the films were evaluated taking into account for different deposition conditions. After depositing the DLC film, the localized corrosion of a point or small area has been significantly improved. We observed that the gas ratio CH<sub>4</sub>/H<sub>2</sub> of 1:1 contributed to the increase in film thickness and sp<sup>3</sup> bond fraction, resulting in a decrease in corrosion current density and metal ions concentration. Because the hydrogen restores the high potential of the oxidic species in SUS316L surface such as Fe, Cr to the low potential, which results in easier formation of Fe-C, Cr-C bonds on the substrate, improving the adhesion and density between the film and substrate. The metal ions concentration and surface roughness of DLC coating

deposited at 12 h are obviously lower than that of DLC deposited at 6 h. The pitting corrosion takes place in the passivation film due to the self-excited reaction and some pores are formed on the surface to accelerate the corrosion rate. As a result, The DLC film-coated SUS316L steel deposited at  $\text{CH}_4/\text{H}_2$  of 1:1, deposition time of 12 h has the best corrosion resistance with a dense film thickness of about 569.8 nm and a carbon permeation layer thickness of about 15  $\mu\text{m}$ , indicating the low corrosion current density of 0.5  $\mu\text{A}/\text{cm}^2$  and low metal ions concentration of 16.60 ppm because of the higher chemical inertness and the less pinholes. The corrosion current density of DLC films-coated SUS316L deposited at  $\text{CH}_4/\text{H}_2 = 1:1$  meets the DOE's 2020 target of 1  $\mu\text{A}/\text{cm}^2$ . Nevertheless, the DLC films deposited at  $\text{CH}_4/\text{H}_2 = 1:1$ , 12 h with the lowest resistance of 12.9  $\text{m}\Omega\cdot\text{cm}^2$  is still higher than the DOE's target (2020) of 10  $\text{m}\Omega\cdot\text{cm}^2$ . Based on these discussions, the DLC films are useful to restrain the corrosion process. However, the DLC films-coated SUS316L steel still cannot meet the resistance of the bipolar plate.

## References

- [1] A. H. Deutchman and R. J. Partyka, "Ion beam enhanced deposition," *Advanced materials & processes*, vol. 161, no. 7, pp. 33-35, 2003.
- [2] R. Toro *et al.*, "Argon and hydrogen plasma influence on the protective properties of diamond-like carbon films as barrier coating," *Surfaces and Interfaces*, vol. 6, pp. 60-71, 2017.
- [3] J. Robertson, "Diamond-like amorphous carbon," *Materials science and engineering: R: Reports*, vol. 37, no. 4-6, pp. 129-281, 2002.
- [4] B. B. Han, D. Y. Ju, M. R. Chai, H. J. Zhao, and S. Sato, "Corrosion Resistance of DLC Film-Coated SUS316L Steel Prepared by Ion Beam Enhanced Deposition," *Advances in Materials Science and Engineering*, vol. 2019, 2019.
- [5] J. H. Kim, J. T. Yeom, J. K. Hong, S. Y. Shim, S. G. Lim, and N. K. Park, "Effect of scandium on the hot extrudability of 7075 aluminum alloy," *Metals and Materials International*, vol. 16, no. 4, pp. 669-677, 2010.
- [6] W. Lengauer and M. Bohn, "Thermochemical basis of the preparation of well-defined transition metal carbide, nitride and carbonitride reference materials for electron-probe microanalysis (epma)," in *Solid State Phenomena*, 2018, vol. 274, pp. 20-42: Trans Tech Publ.
- [7] M. Yoshida, T. Tanaka, S. Watanabe, M. Shinohara, J.-W. Lee, and T. Takagi, "Improvement of oxygen barrier of PET film with diamond-like carbon film by plasma-source ion implantation," *Surface and Coatings Technology*, vol. 174, pp. 1033-1037, 2003.
- [8] C. Casiraghi, A. Ferrari, and J. Robertson, "Raman spectroscopy of hydrogenated amorphous carbons," *Physical Review B*, vol. 72, no. 8, p. 085401, 2005.
- [9] W. Dai, X. Gao, J. Liu, S.-H. Kwon, and Q. Wang, "Compositionally modulated multilayer diamond-like carbon coatings with AlTiSi multi-doping by reactive high power impulse magnetron sputtering," *Applied surface science*, vol. 425, pp. 855-861, 2017.
- [10] N. Huang, H. Yu, L. Xu, S. Zhan, M. Sun, and D. W. Kirk, "Corrosion kinetics of 316L stainless steel bipolar plate with chromiumcarbide coating in simulated PEMFC cathodic environment," *Results in physics*, vol. 6, pp. 730-736, 2016.
- [11] T. Guo, C. Kong, X. Li, P. Guo, Z. Wang, and A. Wang, "Microstructure and mechanical properties of Ti/Al co-doped DLC films: Dependence on sputtering current, source gas, and substrate bias," *Applied Surface Science*, vol. 410, pp. 51-59, 2017.

- [12] D. Xie *et al.*, "Carbon-doped titanium oxide films by dc reactive magnetron sputtering using CO<sub>2</sub> and O<sub>2</sub> as reactive gas," *Acta Metallurgica Sinica (English Letters)*, vol. 27, no. 2, pp. 239-244, 2014.
- [13] L. Wang, R. Zhang, U. Jansson, and N. Nedfors, "A near-wearless and extremely long lifetime amorphous carbon film under high vacuum," *Scientific reports*, vol. 5, p. 11119, 2015.
- [14] J. Sedlmair, *Soft x-ray spectromicroscopy of environmental and biological samples*. Universitätsverlag Göttingen, 2011.
- [15] T. Fukutsuka, T. Yamaguchi, S.-I. Miyano, Y. Matsuo, Y. Sugie, and Z. Ogumi, "Carbon-coated stainless steel as PEFC bipolar plate material," *Journal of Power Sources*, vol. 174, no. 1, pp. 199-205, 2007.
- [16] W. Mingge *et al.*, "Chromium interlayer amorphous carbon film for 304 stainless steel bipolar plate of proton exchange membrane fuel cell," *Surface and Coatings Technology*, vol. 307, pp. 374-381, 2016.
- [17] R. A. Antunes, M. C. L. Oliveira, G. Ett, and V. Ett, "Corrosion of metal bipolar plates for PEM fuel cells: A review," *International journal of hydrogen energy*, vol. 35, no. 8, pp. 3632-3647, 2010.
- [18] R. A. Antunes, M. C. L. Oliveira, G. Ett, and V. Ett, "Corrosion of metal bipolar plates for PEM fuel cells: A review," *International journal of hydrogen energy*, vol. 35, no. 8, pp. 3632-3647, 2010.
- [19] A. Kumar, M. Ricketts, and S. Hirano, "Ex situ evaluation of nanometer range gold coating on stainless steel substrate for automotive polymer electrolyte membrane fuel cell bipolar plate," *Journal of Power Sources*, vol. 195, no. 5, pp. 1401-1407, 2010.
- [20] H. Pan, Q.-j. XU, H. YUN, and X.-q. Deng, "Review on corrosion and surface modification of stainless steel bipolar plates for proton exchange membrane fuel cells," *Corrosion & Protection*, vol. 8, 2011.
- [21] H. Zhang *et al.*, "Performance of Ti-Ag-deposited titanium bipolar plates in simulated unitized regenerative fuel cell (URFC) environment," *international journal of hydrogen energy*, vol. 36, no. 9, pp. 5695-5701, 2011.
- [22] K. Feng, X. Cai, H. Sun, Z. Li, and P. K. Chu, "Carbon coated stainless steel bipolar plates in polymer electrolyte membrane fuel cells," *Diamond and Related Materials*, vol. 19, no. 11, pp. 1354-1361, 2010.
- [23] M. M. Whiston, I. L. Azevedo, S. Litster, K. S. Whitefoot, C. Samaras, and J. F. Whitacre, "Expert assessments of the cost and expected future performance of proton exchange membrane fuel cells for vehicles," *Proceedings of the National*

*Academy of Sciences*, vol. 116, no. 11, pp. 4899-4904, 2019.



# Chapter 6 Conclusion

## 6.1 Discussion and summary

The different DLC coatings were successfully deposited on AZ31 magnesium alloy as hard protective coatings using the IBED method by changing the gas flow rate and accelerating voltage. The composition and friction characteristics of the DLC coatings were analyzed to improve the surface performance of magnesium alloy AZ31, and the following observations were made:

(1) No voids or pinholes were observed and the adhesion strength quality were acceptable in the SEM analysis of the DLC films. The  $I_D/I_G$  decreased to a minimum of 0.62, the hardness increased to a maximum of 4056 HV and the track wear area decreased to  $332 \mu\text{m}^2$  at a lower accelerating voltage of 6 kV and at a higher  $\text{H}_2$  ratio. The friction force decreased to 0.12 N for the DLC coating deposited at 6 sccm/6 kV.

(2) Orbital hybridization between carbon atoms and  $sp^3$  C–C bonds was formed on the surface of the magnesium alloy. The ions with higher energy caused the  $sp^3$  bond to break down into the stable  $sp^2$  bond as the accelerating voltage decreased, and unsaturated C- bonds were saturated by the site-selective adsorption of incident  $\text{CH}_x$ , resulting in a low  $I_D/I_G$ , high fraction of  $sp^3$  carbon, and high hardness in the DLC films.

(3) An increase of the gas flow rate led to reduction of friction force because the increasing number of  $\text{CH}_x$  group ions generated with  $\text{CH}_4$ , which formed  $sp^3$  and  $sp^2$  hybridizations, reduced the number of C-dangling bonds on the surface. A low gas flow rate enhances dissociation of  $\text{CH}_4$  due to the resident time at the plasma and leads to graphitization of the film structure because of H ion/atom/molecule enrichment.

(4) The surface performance of AZ31 magnesium alloy was significantly improved

with the deposition of the DLC films at different flow rates and accelerating voltages by enhancing the hardness and friction properties.

The dense and uniform DLC films as protective film were successfully deposited on SUS316L stainless steel and titanium substrates using IBED technique by changing the gas ratio  $\text{CH}_4/\text{H}_2$  and deposition time. Compared with the other coating techniques, the IBED method has many advantages such as lower compressive stress due to the production of a graded interfacial, higher film-substrate adhesion and better surface properties of high-precision parts, which enables a series of beneficial surface property modifications without detrimentally affecting the bulk properties. The microstructure and corrosion properties of the films were evaluated taking into account for different deposition conditions. The DLC films exhibited improved the corrosion resistance and conductivity. The fully dense DLC film with a thickness of about 1281 nm exhibited the best anti-corrosion behavior because the film is dense. The ICR increases as the  $\text{H}_2$  ratio increases because the good conductive performance depends on high content of  $\text{sp}^2\text{-C}$  bonds. The DLC film deposited at gas ratios  $\text{CH}_4/\text{H}_2 = 1:0$  is denser than at  $\text{CH}_4/\text{H}_2 = 1:1$  from the SEM images. Meanwhile the nanocrystalline TiC phase is observed from penetration layer of DLC films-coated titanium which has the strong and stable chemical bond energy. The DLC film can protect the substrate from corrosion due to its densification and chemical inertness. The metal ions contaminant concentration of a-C:H coating deposited at  $\text{CH}_4/\text{H}_2 = 1:0$  is obviously lower than at  $\text{CH}_4/\text{H}_2 = 1:1$ . Even the a-C:H film-coated titanium deposited at  $\text{CH}_4/\text{H}_2 = 1:0$ , 6h is lower than at  $\text{CH}_4/\text{H}_2 = 1:1$ , 12h. And the DLC film has the lowest metal ions concentration of 0.34 ppm at the condition of  $\text{CH}_4/\text{H}_2 = 1:0$ , 12 h. As a result, the DLC film deposited on the titanium at  $\text{CH}_4/\text{H}_2 = 1:0$  has the better anti-corrosion resistance. Therefore the a-C:H films-coated titanium

substrate are useful to restrain the corrosion process and could be considered as a candidate bipolar plates for PEMFC.

We observed that the gas ratio  $\text{CH}_4/\text{H}_2$  of 1:1 contributed to the increase in film thickness and  $\text{sp}^3$  bond fraction, resulting in a decrease in corrosion current density and metal ions concentration for the SUS316L substrate. The hydrogen restores the high potential of the oxidic species in SUS316L surface such as Fe, Cr to the low potential, which results in easier formation of Fe-C, Cr-C bonds on the substrate, improving the adhesion and density between the film and substrate. The metal ions concentration and surface roughness of DLC coating deposited at 12 h are obviously lower than that of DLC deposited at 6 h. The pitting corrosion takes place in the passivation film due to the self-excited reaction and some pores are formed on the surface to accelerate the corrosion rate. As a result, The DLC film-coated SUS316L steel deposited at  $\text{CH}_4/\text{H}_2$  of 1:1, deposition time of 12 h has the best corrosion resistance with a dense film thickness of about 569.8 nm and a carbon permeation layer thickness of about 15  $\mu\text{m}$ , indicating the low corrosion current density of 0.5  $\mu\text{A}/\text{cm}^2$  and low metal ions concentration of 16.60 ppm because of the higher chemical inertness and the less pinholes. The corrosion current density of DLC films-coated SUS316L deposited at  $\text{CH}_4/\text{H}_2 = 1:1$  meets the DOE's 2020 target of 1  $\mu\text{A}/\text{cm}^2$ .

The density and chemical bonding structure of DLC films are key factors influencing the corrosion behavior.

## 6.2 Future work

For Mg alloy AZ31, future work will involve improving the precipitation hardening of magnesium alloy to improve the supporting effect of the substrate and coating durability.

Based on these discussions, the DLC films are useful to restrain the corrosion process. For DLC films-coated SUS316L, a denser interlayer between the substrate and DLC film is considered. The DLC films deposited at  $\text{CH}_4/\text{H}_2 = 1:1$ , 12 h with the lowest resistance of  $12.9 \text{ m}\Omega\cdot\text{cm}^2$  is still higher than the DOE's target (2020) of  $10 \text{ m}\Omega\cdot\text{cm}^2$ . The DLC films-coated SUS316L steel still cannot meet the resistance of the bipolar plate. Hence, future work would be needed to improve the DLC film-coated SUS316L resistance by adding a conductive path to the DLC film while reducing the cost of the manufacturing. The processing condition,  $\text{CH}_4$  ratio of 25% and 75% will also be considered perfect conclusions.

## Related Publications

- [1] **Beibei Han**, Dongying Ju, Susumu Sato, Huijun Zhao. Effect of CH<sub>4</sub>/H<sub>2</sub> gas flow rate on hardness and tribological properties of magnesium alloy AZ31 coated with DLC film. Taiwan Association for Coatings and Thin films Technology (TACT) 2017 International Thin Films Conference. D-O-495.
- [2] **Beibei Han**, Huijun Zhao, Dongying Ju, Maorong Chai, Susumu Sato. Corrosion Resistance of DLC Films-Coated Stainless Steel Prepared by Ion Beam Enhanced Deposition. 25th Congress of International Federation for Heat Treatment and Surface Engineering (IFHTSE) 2018. Chinese Heat Treatment Society. NO. 527
- [3] **HAN BeiBei**, JU DongYing, SATO Susumu, ZHAO HuiJun. Plasma preparation method and tribological properties of diamond-like carbon coating on magnesium alloy AZ31 substrate. SCIENCE CHINA Technological Sciences, Vol. 62, pp. 1939-1947, 2019.
- [4] **Beibei Han**, Dongying Ju, Susumu Sato and Huijun Zhao. Preparation, Characterization and Tribological Properties of Diamond-Like Carbon Film on AZ31 Magnesium Alloy. Key Engineering Materials, Vol. 804, pp. 69-74, 2019
- [5] **Beibei Han**, Dongying Ju, Susumu Sato, Maorong Chai. Microstructure and corrosion behavior of DLC films deposited on SUS316L and titanium substrate for bipolar plates. 26th IFHTSE CONGRESS 2019 International Congress on Metal Science and Heat Treatment. September 17-19, 2019. Moscow, Russia. pp 253-258.
- [6] **BeiB. Han**, DongY. Ju, MaoR. Chai, HuiJ. Zhao, and Susumu Sato. Corrosion Resistance of DLC Film-Coated SUS316L Steel Prepared by Ion Beam Enhanced Deposition. Advances in Materials Science and Engineering. Vol. 2019, Article ID 7480618, 13 pages (In press).

- [7] Kun WANG, Dongying JU, Guiying XU, **Beibei HAN**, Yongfei WANG, Jian ZHANG, Maorong CHAI, Shaobei CHEN, Weimin ZHOU. Enhanced Li Ion Storage Performances of Carbon Black by Introducing Organosulfur Groups on Surface. *Electrochemistry*. Vol. 88, pp 8-13, 2020.

## Acknowledgements

During the preparation of the doctor's thesis, I have received a lot of invaluable helps from many people. Their comments and advices contribute to the accomplishment of the thesis.

First of all I would like to extend my sincere gratitude to my supervisor, Prof. Dongying Ju, for his instructive advice and useful suggestions in the academic studies. I am deeply grateful for giving me the opportunity to pursue the Ph.D degree at Saitama Institute of Technology. I would also thank all the Ju Laboratory members for their enjoyable help and collaboration.

I would like to express my gratitude to Dr. Y. Watanabe, Prof. S. Sato, Prof. M. Uchida and Prof. R. Negishi for spending much time reading the thesis and provided me with inspiring advice. Without their patient instruction, insightful criticism and expert guidance, the completion of this thesis would not have been possible.

I also owe a special debt of gratitude to Prof. M. R. Chai, Prof. W. M. Zhou, Prof. M. Uchida and Prof. S. Sato, from whose patient instruction and suggestion I have completed the experiment and academically prepared for the thesis.

I should finally like to express my gratitude to my beloved parents, H. X. Han & M. L. Liu, who have always been helping me out of difficulties and supporting without a word of complaint.